Distribution Categories:
Coal Conversion and Utilization:
Coal Gasification (UC-90c)
Direct Combustion of Coal (UC-90e)
Materials and Components (UC-90h)

ANL-79-56

ARGONNE NATIONAL LABORATORY
9700 South Cass Avenue
Argonne, Illinois 60439

# MATERIALS TECHNOLOGY FOR COAL-CONVERSION PROCESSES

Seventeenth Quarterly Report
January—March 1979

W. A. Ellingson
Program Manager

Materials Science Division

Previous reports in this series

| | |
|---|---|
| ANL-78-54 | January—March 1978 |
| ANL-78-79 | April—June 1978 |
| ANL-79-2 | July—September 1978 |
| ANL-79-23 | October—December 1978 |

TABLE OF CONTENTS

TABLE OF CONTENTS (continued)

LIST OF FIGURES

LIST OF FIGURES (contd.)

LIST OF FIGURES (contd.)

LIST OF FIGURES (contd.)

LIST OF TABLES

MATERIALS TECHNOLOGY FOR COAL-CONVERSION PROCESSES:
SEVENTEENTH QUARTERLY REPORT
January-March 1979

## HIGHLIGHTS

Task A -- Evaluation of Ceramic Refractories for Slagging Gasifiers *(C. R. Kennedy, R. N. Singh, R. J. Fousek, S. W. Kreis, and R. E. Mailhiot)*

In test run 10, the corrosion of a wide variety of commercial refractories in a mixture of coal-ash slag and potassium seed at ∿ 1500°C under reducing conditions has been investigated. These conditions simulate the operating environment of the water walls of a radiant boiler in a coal-fired open-cycle MHD plant. Several refractories appear promising for this application. As compared with earlier results obtained with slag only at ∿ 1500°C, the presence of ∿ 10 wt % $K_2O$ seed in the Montana Rosebud slag did not result in increased corrosion, and may have actually improved the corrosion resistance of many of the refractories that were tested. The fused-cast chrome-spinel refractory exhibited the highest corrosion resistance of any refractory tested. The magnesia-chrome refractories showed more resistance to corrosion than the other sintered materials that were tested. A phosphate-bonded chrome-ore ramming mix performed better than the other ramming mixes tested, but not as well as any of the sintered or fused-cast bricks.

Test run 11, which evaluated the compatibility of a variety of refractories with a basic slag (B/A = 1.5), has been completed. Again, the fused-cast chrome-spinel refractory was the most resistant to attack.

Task C -- Development and Application of Nondestructive Evaluation Methods for Coal-conversion Processes *(W.A. Ellingson, K.J. Reimann, C.A. Youngdahl and R.R. Roberts)*

The high-temperature ultrasonic erosion monitoring system installation was 75% completed on the gas-stream cleanup section of the Morgantown Energy Technology Center (METC) gas producer. The data-acquisition system will be controlled by the METC digital computer. Acoustic-emission data from the 95% $Al_2O_3$ refractory firing are consistent with the theory that a uniform shift in amplitude does not affect characteristic slope. Modification of an existing coal-slurry loop is in progress to establish the sensitivity limits for leak detection in slurry valves. Present results on scattering of ultrasonic waves from roughened surfaces suggest that time-domain deconvolution methods and acoustic spectroscopy yield similar resolution of thickness values.

Task D.1 -- Corrosion in Gasification Environments *(K. Natesan)*

Corrosion and uniaxial tensile specimens of Incoloy 800, Type 310 stainless steel, Inconel 671, and U. S. Steel Alloy 18-18-2 were exposed for 3.6 Ms to multicomponent gas mixtures at temperatures of 750, 871, and 982°C. Information is presented on the type and thickness of corrosion-product layers and on depths of intergranular penetration of the base metal for the specimens exposed to these simulated coal-gasification environments.

Task D.2 -- Effect of Sulfation Accelerators and Corrosion Inhibitors on Materials in Fluidized-bed Combustion Systems *(O. K. Chopra)*

The corrosion behavior of several iron- and nickel-base alloys has been evaluated after 360-ks (100-h) exposures in the bed and freeboard regions of an atmospheric-pressure fluidized-bed combustor. The influence of small additions of NaCl, $CaCl_2$, and $Na_2CO_3$ (i.e., sulfation-enhancement agents) to the limestone on the average thickness of the surface scale and internal corrosive penetration at temperatures between $\sim$ 700 and 1120 K was determined from metallographic evaluation of the specimens. The results indicated that the addition of 0.3 mol % $CaCl_2$ to the fluidized bed had no significant effect on the corrosion behavior of the various materials; however, 0.5 mol % NaCl or 1.9 mol % $Na_2CO_3$ increased the corrosion rates of most of the materials. In general, the austenitic stainless steels and Haynes Alloy 188 exhibit better resistance against accelerated corrosion in the presence of salts than the high-nickel alloys. The various materials located in the freeboard section of the combustor at temperatures between $\sim$ 800 and 975 K showed no detectable corrosion.

Task E -- Erosion Behavior of Materials in Coal-conversion Processes *(J.Y. Park, S. Danyluk, and W.J. Shack)*

Repair of the corrosion/erosion test apparatus has continued. The cause of the cooling-water leak is being sought, and a new heating element is being installed.

Task F -- Component Performance and Failure Analysis *(S. Danyluk, G.M. Dragel, and L.E. Pahis)*

A number of failed components from the Grand Forks Energy Technology Center were examined. These included three tuyere tips and a perforated vapor-barrier liner from the slagging gasifier, and three flow-control valves from the liquefaction unit. A 6-inch ball valve from the Morgantown Energy Technology Center Valve Dynamic Test Unit was examined after excessive leakage developed during simulated lockhopper service.

MATERIALS TECHNOLOGY FOR COAL-CONVERSION PROCESSES:
SEVENTEENTH QUARTERLY REPORT,
January-March 1979

## FOREWORD

This broad-base materials engineering program, begun in 1974, includes studies on ceramic (refractory) and metallic materials presently being used or intended for use in coal-conversion processes. The program entails nondestructive testing, failure analysis, and studies of erosive wear, corrosion and refractory degradation. Appropriate laboratory and field experiments are integrated such that the results have impact on present pilot- and demonstration-plant and proposed full-scale designs. This quarterly report, for the period January-March 1979, presents the technical accomplishments of the program.

## ABSTRACT

Studies of slag attack on refractories were continued, utilizing conditions relevant to MHD applications. Addition of 10 wt % $K_2O$ seed to the slag did not increase its corrosive effect on the refractories tested.

A hot gas-stream cleanup erosion-monitoring system using an ANL-developed nondestructive ultrasonic system was installed at the Morgantown Energy Technology Center (METC) during this period and was 75% completed. Characteristic-slope values obtained from broadband and resonant-band acoustic-emission transducers during rapid heating of a 95% $Al_2O_3$ refractory panel are consistent with theory.

Corrosion information on type and thickness of corrosion-product layers was obtained on Incoloy 800, 310 stainless steel, Inconel 671 and U.S. Steel Alloy 18-18-2 after exposure to corrosive environments at 750, 871 and 982°C. Fluid-bed corrosion studies involving sulfation accelerators have shown that addition of 0.3 mol % $CaCl_2$ has no significant effect on corrosion behavior of the alloys studied. However, 0.5 mol % NaCl or 1.9 mol % $Na_2CO_3$ increases the corrosion rates of most materials.

Failure analyses were performed on components from the slagging gasifier and liquefaction unit at the Grand Forks Energy Technology Center, and a ball valve from the METC Valve Dynamic Test Unit.

# INTRODUCTION

The economical conversion of coal into clean and readily usable fuels will be advanced through the use of durable materials. The technical information base applicable to materials selection in plant design for the operating environments of various coal-conversion processes is extremely limited. Hence, reliable selection and lifetime-prediction methods for materials under these conditions are not available. This project is designed to provide part of the materials information necessary for successful operation of coal-conversion systems. The present report is the seventeenth quarterly progress report submitted by ANL to the Division of Systems Engineering, Office of Fossil Energy under Project Number 7106, "Materials Technology for Coal-conversion Processes".

The project includes six tasks: (A) evaluation of commercial refractories exposed to coal slag under conditions typical of those encountered in slagging gasification processes; (B) evaluation of erosion/corrosion-resistant coatings when exposed to prototype operating environments (suspended in FY 78); (C) development, evaluation, and application of non-destructive evaluation methods applicable to coal-conversion systems; (D) evaluation of the corrosion behavior of commercial alloys; (E) development of analytical models to predict the erosive-wear behavior of materials used in coal-conversion plants; and (F) analysis of failed coal-conversion plant components.

Task A -- Evaluation of Ceramic Refractories for Slagging Gasifiers

*(C. R. Kennedy, R. N. Singh, E. J. Fousek, C. W. Kreis, and R. E. Mailhiot)*

In addition to applications in slagging gasifiers, refractories are also being considered for use in a variety of components of a coal-fired open-cycle magnetohydrodynamic (MHD) power-generator system. In particular, refractories may be required in the construction of a combustor, high-temperature air heater, radiant boiler, and high-temperature gas ducting. In all these applications, the refractories must be able to withstand high operating temperatures and the corrosive-erosive conditions associated with liquid coal slag. Furthermore, the situation may be exacerbated by the high levels of alkalies (particularly potassium compounds) which are injected as a seed material to increase the electrical conductivity of the plasma in the MHD generator. Although a considerable amount of information is available on refractory-materials behavior in coal-fired systems in general,[1-3] little is known about the corrosion behavior of refractories in the slagging environment of a coal-fired MHD system, which has significantly higher potassium levels than other systems. Therefore, test run 10 was performed to evaluate the corrosion behavior of a number of candidate ceramic refractory materials in contact with a high-temperature ($\sim$ 1500°C) mixture of coal slag and seed to simulate the conditions within the radiant boiler of an MHD power generator.

A wide variety of commercially available materials in the form of bricks and easily repairable ramming materials were exposed for $\sim$ 500 h at 1500°C to an artificial Montana Rosebud coal slag, with $\sim$ 10 wt % $K_2O$ to simulate the effect of the seed. The chemical compositions of the refractories that were tested are listed in Table I. The partial pressure of oxygen was maintained at $\sim 10^{-5}$ Pa by adjusting the relative flow of natural gas, air, and oxygen. Chemical analysis of gas samples taken from the furnace at various times during the tests were used to calculate the partial pressure of oxygen at the furnace temperature. The temperature was measured with a Pt vs Pt-10% Rh thermocouple. During the test, seed material ($K_2SO_4$) was frequently added to maintain the desired $K_2O$ content in the slag.

After termination of the test, the bricks were removed from the furnace and sectioned lengthwise in the vertical plane so that the slag attack (depth of material removed and depth of slag penetration) could be viewed in cross section.

The composition of the slag during test run 10 is given in Table II. The concentrations of $SiO_2$, iron oxides, CaO, MgO, and $Na_2O$ in the slag remained fairly constant throughout the test. However, the concentration of $K_2O$ in the slag decreased during the test as a result of preferential vaporization, and the $Al_2O_3$ concentration increased slightly. Additional potassium salt ($K_2SO_4$) was frequently added during the test to maintain the potassium oxide levels in the slag between $\sim$ 6 and 10 wt %. The potassium oxide concentration in the slag as a function of time during the test is given in Fig. 1. An average $K_2O$ concentration of $\sim$ 8 wt % was maintained during the entire test run. The base-to-acid ratio (B/A) was fairly constant (0.4 to 0.6) over the entire test period. The ferritic content in the slag

was low (0.25 to 0.4), indicating that the test was performed under predominantly reducing conditions.

The thermal history of each sample during the entire 475-h test duration is summarized in Figs. 2-4. During the test, the furnace temperature was raised to ∿ 1500°C, and when a steady-state temperature profile was achieved, slag was added. When the initial charge of slag (70-80 kg) was completely melted, the furnace temperature was increased to ∿ 1600°C and kept there for an ∿ 24-h period. Another 70-80 kg of slag was then added, and the temperature was lowered to ∿ 1500°C. The test was continued at this lower temperature for an additional ∿ 450 h before termination. Since the slag pool is heated only from the top, a strong vertical gradient (∿ 7°C/mm) exists within the slag. Thus, most of the attack on the refractories occurs at the slag line. Two such slag-attack lines were visible on some refractories. The top attack line corresponds to an exposure at ∿ 1500°C for 450 h, whereas the bottom attack line, which was "frozen in" by the second slag addition, corresponds to an exposure at ∿ 1600°C for 24 h.

Full- and 1/2-size refractory samples were tested in the same test run. The temperatures at two locations (25.4 and 76.2 mm from the hot face) were recorded for each sample, as shown in Figs. 2-4. Generally, full-size bricks were 50-100°C hotter than 1/2-size bricks. After the test, the samples were sectioned lengthwise to determine the extent of corrosion. The sectioned samples are shown in Figs. 5-7. Two slag-seed attack lines are visible on the fused-cast alumina sample (number 2) in Fig. 5a.

The relative resistance of the three fused-cast refractory compositions to seed-slag attack is summarized in Table III. It is apparent from the data on maximum depth of material removal and slag-seed penetration that among the fused-cast bricks tested, the chrome-spinel (number 22) exhibited the best performance. The fused-cast alumina-chrome bricks (number 38) had good corrosion resistance, but suffered from extensive cracking (Fig. 5a) owing to either thermal shock or the steep temperature gradient during the testing. The fused-cast alumina material (number 2) showed fair performance; however, extensive slag-seed penetration was observed in the central porous region (Fig. 5b) which was formed during casting of the brick.

The relative resistance of the four sintered refractory compositions to slag-seed attack is summarized in Table IV. The sintered magnesia-spinel brick (number 98) had only average corrosion resistance, and also suffered from extensive cracking (Fig. 6b). This material also showed attack by the potassium-rich vapors produced during the test. A significant amount of seed-slag penetration was also observed for this material. The alumina-chromia material (number 23) showed intermediate corrosion resistance, but the full-length brick suffered from swelling (Fig. 6c) as a result of gas-phase attack. The two sintered magnesia-chrome refractories (numbers 20 and 29) showed the best corrosion resistance (minimum depth of removal) among the sintered materials; however, the 1/2-length bricks suffered from cracking (Figs. 6f and h), probably owing to the steep thermal gradient.

The relative resistance of the four types of ramming mixes to slag-seed attack is summarized in Table V. Of the four ramming mixes, the phosphate-bonded chrome-ore (number 18) performed the best whereas the

silicate-bonded chrome-ore (number 99) performed the worst. The alumina-chrome mix (number 96) showed intermediate performance, but the full-length brick exhibited substantial swelling (see Fig. 7e). The magnesia mix (number 97) suffered extensive cracking (see Figs. 7g and h), swelling, and more gas-phase than liquid-phase attack.

Samples have been obtained from areas close to the slag-refractory interfaces for microstructural examinations via optical microscopy and SEM. The results from these examinations will be utilized in determining the nature and mechanism of the corrosion.

In general, the corrosion resulting from exposure to Rosebud-type slag-seed mixtures was less than or equal to that resulting from exposures to similar (but not identical) Rosebud-type slags without seed. These results are in qualitative agreement with the limited results of other experiments.[4-6] Two potential explanations for improved corrosion resistance in the presence of seed exist. First, it has been reported[7] that the viscosity of the slag increases with increasing $K_2O$ content (up to 20 wt %). Second, the addition of $K_2O$ to coal slag has been found to decrease wetting of many refractories by the slag.[8]

Test run 11, which exposed a variety of refractories to a basic slag (B/A = 1.5, Table VI), at 1500°C for ~ 500 h, has now been completed. The results are currently being compiled and analyzed, and will be presented in detail in the next quarterly report. A preliminary evaluation of the relative corrosion resistance of the tested refractories is presented in Table VII. As in tests with acidic slags, the fused-cast chrome-spinel refractory was the most resistant to corrosion.

TABLE I. Refractories Tested in Run 10

| Number | Type | Composition |
|---|---|---|
| 2 | Fused-cast alumina | $Al_2O_3$(99)-$Na_2O$(0.4) |
| 22 | Fused-cast chrome-spinel | $Cr_2O_3$(80)-MgO(8)-$Fe_2O_3$(6) |
| 38 | Fused-cast alumina-chromia | $Al_2O_3$(60.4)-$Cr_2O_3$(27.3)-MgO(6.0)-$Fe_2O_3$(4.2)-$SiO_2$(1.8) |
| 20 | Sintered magnesia-chrome | MgO(59)-$Cr_2O_3$(19)-$Al_2O_3$(13)-$Fe_2O_3$(7)-$SiO_2$(1.5)-CaO(0.5) |
| 23 | Sintered alumina-chromia | $Al_2O_3$(89.7)-$Cr_2O_3$(10) |
| 29 | Sintered magnesia-chrome | MgO(63)-$Cr_2O_3$(19)-$Al_2O_3$(5)-$Fe_2O_3$(12)-$SiO_2$(1)-CaO(1) |
| 98 | Sintered magnesia-spinel | $Al_2O_3$(70)-MgO(28) |
| 18 | Phosphate-bonded chrome-ore ramming mix | $Cr_2O_3$(39.6)-$Al_2O_3$(21.4)-$Fe_2O_3$(22.6)-MgO(9.6)-$SiO_2$(2.5)-$TiO_2$(0.6)-$P_2O_5$(3.7) |
| 96 | Alumina-chromia ramming mix | $Al_2O_3$(85)-$Cr_2O_3$(10)-$SiO_2$(2)-$P_2O_5$(3) |
| 97 | Magnesia ramming mix | MgO(95)-$SiO_2$(3)-CaO(1) |
| 99 | Silicate-bonded chrome-ore ramming mix | $Cr_2O_3$(33)-$Al_2O_3$(28)-MgO(19)-FeO(13)-$SiO_2$(5) |

TABLE II. Composition of Slag (wt %)[a] During Corrosion Test Run 10

| Component | Exposure Time, h | | | | | | | | |
|---|---|---|---|---|---|---|---|---|---|
| | 0 | 23 | 111 | 183 | 255 | 303 | 374 | 405 | 473 |
| $SiO_2$ (S) | 38.0 | 36.0 | 38.2 | 37.4 | 38.[illegible] | 38.8 | 38.6 | 38.8 | 37.8 |
| $Al_2O_3$ (A) | 24.8 | 24.6 | 28.7 | 30.8 | 29.4 | 31.3 | 30.8 | 29.1 | 30.9 |
| $Fe_2O_3$ ($F_1$) | 1.8 | 1.3 | 1.0 | 1.2 | 1.7 | 0.9 | 1.1 | 1.1 | 1.3 |
| FeO ($F_2$) | 1.5 | 1.9 | 1.4 | 1.3 | 1.2 | 1.8 | 1.9 | 1.7 | 1.8 |
| Fe ($F_3$) | 0.6 | 0.7 | 1.0 | 1.0 | 0.7 | 0.8 | 0.6 | 0.4 | 0.5 |
| CaO (C) | 17.1 | 20.0 | 16.0 | 16.1 | 17.6 | 17.9 | 18.7 | 13.3 | 19.9 |
| MgO (M) | 5.3 | 5.7 | 4.9 | 3.8 | 3.7 | 4.0 | 3.8 | 3.0 | 3.4 |
| $Na_2O$ (N) | 0.2 | 0.2 | 0.2 | 0.15 | 0.15 | 0.1 | 0.1 | 0.1 | 0.05 |
| $K_2O$ (K) | 10.21 (11.1)[b] | 9.0 (9.5) | 8.1 (9.1) | 7.8 | 6.3 (7.8) | 6.4 (6.1) | 7.2 (7.0) | 11.9 (11.3) | 7.1 |
| $TiO_2$ (T) | <0.1 | 0.2 | 0.2 | 0.2 | 0.3 | 0.3 | 0.35 | 0.3 | 0.3 |
| $Cr_2O_3$ | <0.1 | 0.1 | <0.1 | <0.1 | <0.1 | <0.1 | <0.1 | <0.1 | <0.1 |
| B/A Ratio[c] | 0.55 | 0.63 | 0.50 | 0.44 | 0.45 | 0.40 | 0.42 | 0.46 | 0.44 |
| Ferritic content, %[d] | 40 | 30 | 25 | 29 | 40 | 22 | 27 | 30 | 30 |

[a] Measured after the 1500°C operating temperature was reached.

[b] Numbers in parentheses give $K_2O$ concentrations determined from an independent analysis.

[c] Base-to-acid ratio $B/A = (F_1 + F_2 + F_3 + C + M + N + K)/(S + A + T)$.

[d] Ferritic content $= \dfrac{\text{wt \% } (Fe_2O_3)}{\text{wt \% } (Fe_2O_3) + 1.11 \text{ wt \% } (FeO) + 1.43 \text{ wt \% } (Fe)}$.

TABLE III. Relative Corrosion Resistance of Fused-cast Refractories Exposed to Slag-Seed Attack in Test Run 10

| Number | Type | Attack Line | Maximum Depth of Removal[a], mm | | Maximum Depth of Penetration[a], mm | | Remarks |
|---|---|---|---|---|---|---|---|
| | | | Full-length | 1/2-length | Full-length | 1/2-length | |
| 2 | Alumina | Top[b] | 1 | 1 | 45 | 60 | Some cracking. Penetration into central porous region resulting from casting. |
| | | Bottom[c] | 1 | 0 | 45 | 60 | |
| 22 | Chrome-spinel | Top | 0 | 0 | 0 | 0 | Full length - some cracks |
| | | Bottom | 0 | 0 | 0 | 0 | Half length - no cracks. |
| 38 | Alumina-chromia | Top | 1 | 1 | 0 | 0 | Substantial cracking. |
| | | Bottom | 0 | 0 | 0 | 0 | |

[a] Measured from the original hot face.

[b] 455 h at ∿ 1500°C

[c] 24 h at 1600°C

TABLE IV. Relative Corrosion Resistance of Sintered Refractories Exposed to Slag-Seed Attack in Test Run 10

| Number | Type | Attack Line | Maximum Depth of Removal[a], mm | | Maximum Depth of Penetration[a], mm | | Remarks |
|---|---|---|---|---|---|---|---|
| | | | Full-length | 1/2-length | Full-length | 1/2-length | |
| 20 | Magnesia-chrome | Top[b] | 1 | <1 | 40?[c] | 10? | Pitted by gas phase. No cracking. |
| | | Bottom[d] | 1 | <1 | 40? | 10? | |
| 23 | Alumina-chromia | Top | 2 | 1 | 23 | 15 | Some swelling of full-length brick due to gas-phase attack. |
| | | Bottom | 2 | 1 | 18 | 10 | |
| 29 | Magnesia-chrome | Top | 1 | <1 | ? | ? | Pitted by gas phase. Some cracking. |
| | | Bottom | 1 | <1 | ? | ? | |
| 98 | Magnesia-spinel | Top | 1 | 1 | 40 | 35 | Extensive cracking and attack by gas phase. |
| | | Bottom | 4 | 2 | 50 | 35 | |

[a] Measured from the original hot face.

[b] 455 h at ∿ 1500°C.

[c] ? = measurement in doubt or impossible.

[d] 24 h at 1600°C.

TABLE V. Relative Corrosion Resistance of Ramming-mix Refractories Exposed to Slag-Seed Attack in Test Run 10

| Number | Type | Attack Line | Maximum Depth of Removal[a], mm | | Maximum Depth of Penetration[a], mm | | Remarks |
|---|---|---|---|---|---|---|---|
| | | | Full-length | 1/2-length | Full-length | 1/2-length | |
| 18 | Phosphate-bonded chrome ore | Top[b] | 2 | 2 | 60 | 49 | Some cracking. |
| | | Bottom[c] | ?[d] | 2 | 60 | 45 | |
| 96 | Alumina-chromia | Top | 3-5 | 1 | 50 | 15 | Full length - substantial swelling. Some cracking. |
| | | Bottom | 3-5 | 1 | 40 | 15 | |
| 97 | Magnesia | Top | 5 | 4 | 6 | 5 | Extensive cracking and swelling. More attack by gas than liquid phase. |
| | | Bottom | 6 | 4 | 7 | 5 | |
| 99 | Silicate-bonded chrome ore | Top | 20 | 4 | 70 | 52 | |
| | | Bottom | ? | ? | 70 | 52 | |

[a] Measured from the original hot face.

[b] 455 h at ∿ 1500°C.

[c] 24 h at 1600°C.

[d] ? = Measurement impossible because the refractory fractured upon removal from the furnace.

TABLE VI. Composition of Slag (wt %)[a] During Corrosion Test Run 11

| Component | Exposure Time, h | | |
|---|---|---|---|
| | 1 | 303 | 398 |
| $SiO_2$ (S) | 25.1 | 23.0 | 25.1 |
| $Al_2O_3$ (A) | 15.3 | 16.1 | 15.0 |
| $Fe_2O_3$ ($F_1$) | 4.3 | 4.2 | 4.2 |
| FeO ($F_2$) | 8.3 | 9.4 | 9.2 |
| Fe ($F_3$) | 1.0 | 0.9 | 1.0 |
| CaO (C) | 39.2 | 39.4 | 38.2 |
| MgO (M) | 5.5 | 5.8 | 5.8 |
| $Na_2O$ (N) | 0.1 | 0.1 | 0.1 |
| $K_2O$ (K) | 0.1 | 0.1 | 0.1 |
| $TiO_2$ (T) | 1.0 | 1.0 | 1.1 |
| B/A Ratio[b] | 1.4 | 1.5 | 1.4 |
| Ferritic Content[c], % | 29 | 26 | 26 |

[a]Measured after the 1500°C operating temperature was reached.

[b]As in Table II.

[c]As in Table II.

TABLE VII. Relative Corrosion Resistance of Refractories Exposed to a Basic Slag in Test Run 11

| Number | Type | Maximum Depth of Removal[a], mm | Composition |
|---|---|---|---|
| 2 | Fused-cast alumina | 11 | $Al_2O_3$(99)-$Na_2O$(6.5) |
| 22 | Fused-cast chrome-spinel | 0-1 | $Cr_2O_3$(30)-MgO(8)-$Fe_2O_3$(6)-$Al_2O_3$(5)-$SiO_2$(1) |
| 280 | Fused-cast aluminia-chromia | 0-1 | $Al_2O_3$(65)-$Cr_2O_3$(32)-FeO(1) |
| 317 | Fused-cast magnesia-spinel | 15 | MgO(65)-$Al_2O_3$(35) |
| 16 | Sintered alumina-chromia | 10 | $Al_2O_3$(90)-$Cr_2O_3$(10) |
| 852 | Sintered alumina-chromia | 3 | $Al_2O_3$(81)-$Cr_2O_3$(16.6)-$P_2O_5$(1.0) |
| 29 | Sintered magnesia-chrome | 4 | MgO(63)-$Cr_2O_3$(18)-$Fe_2O_3$(12)-$Al_2O_3$(5)-$SiO_2$(1)-CaO(1) |
| 35 | Sintered magnesia-chrome | 4 | MgO(60)-$Cr_2O_3$(15.5)-$Al_2O_3$(15)-$Fe_2O_3$(7)-$SiO_2$(1.5)-CaO(1) |
| 41 | Sintered magnesia-chrome | | MgO(55)-$Cr_2O_3$(20)-$Al_2O_3$(8)-FeO(11)-$SiO_2$(2.5)-$TiO_2$(1.5) |
| 190 | Chemically bonded alumina-chrome | 9 | $Al_2O_3$(91)-$Cr_2O_3$(7.5) |
| 86 | Sintered alumina-chromia | 21 | $Al_2O_3$(84.5)-$Cr_2O_3$(10.5)-$P_2O_5$(4.5) |

[a]Measured from the original hot face.

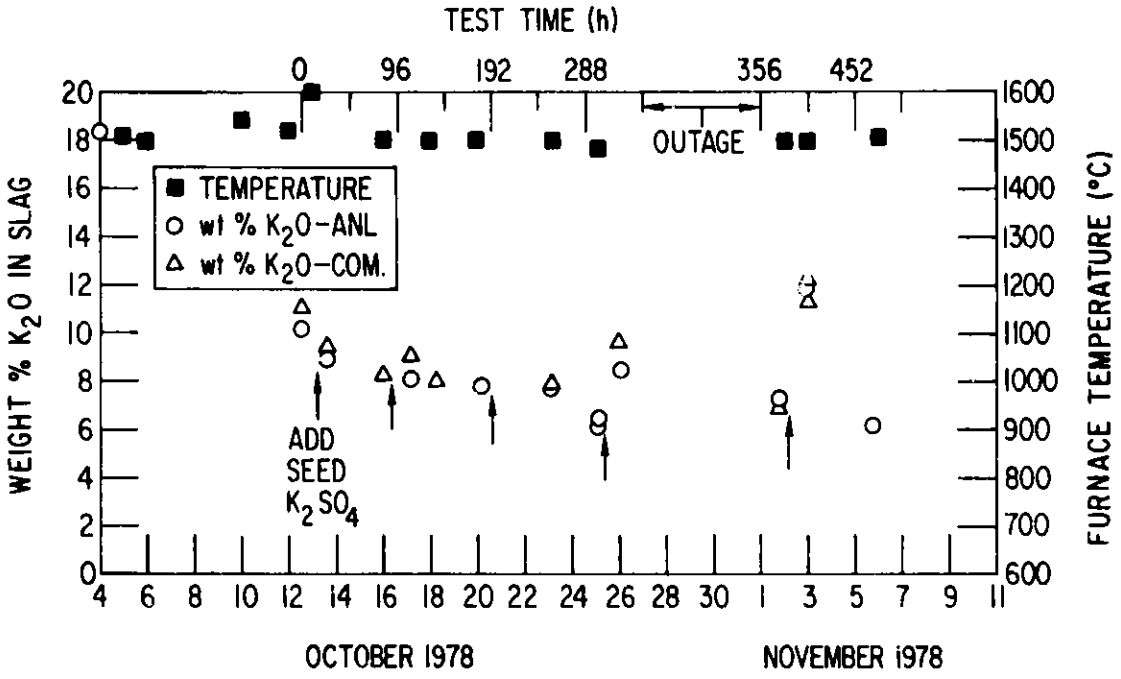


Fig. 1. Weight Percent $K_2O$ and Furnace Plenum Temperature as a Function of Time During Test Run 10. ANL Neg. No. 306-79-297.

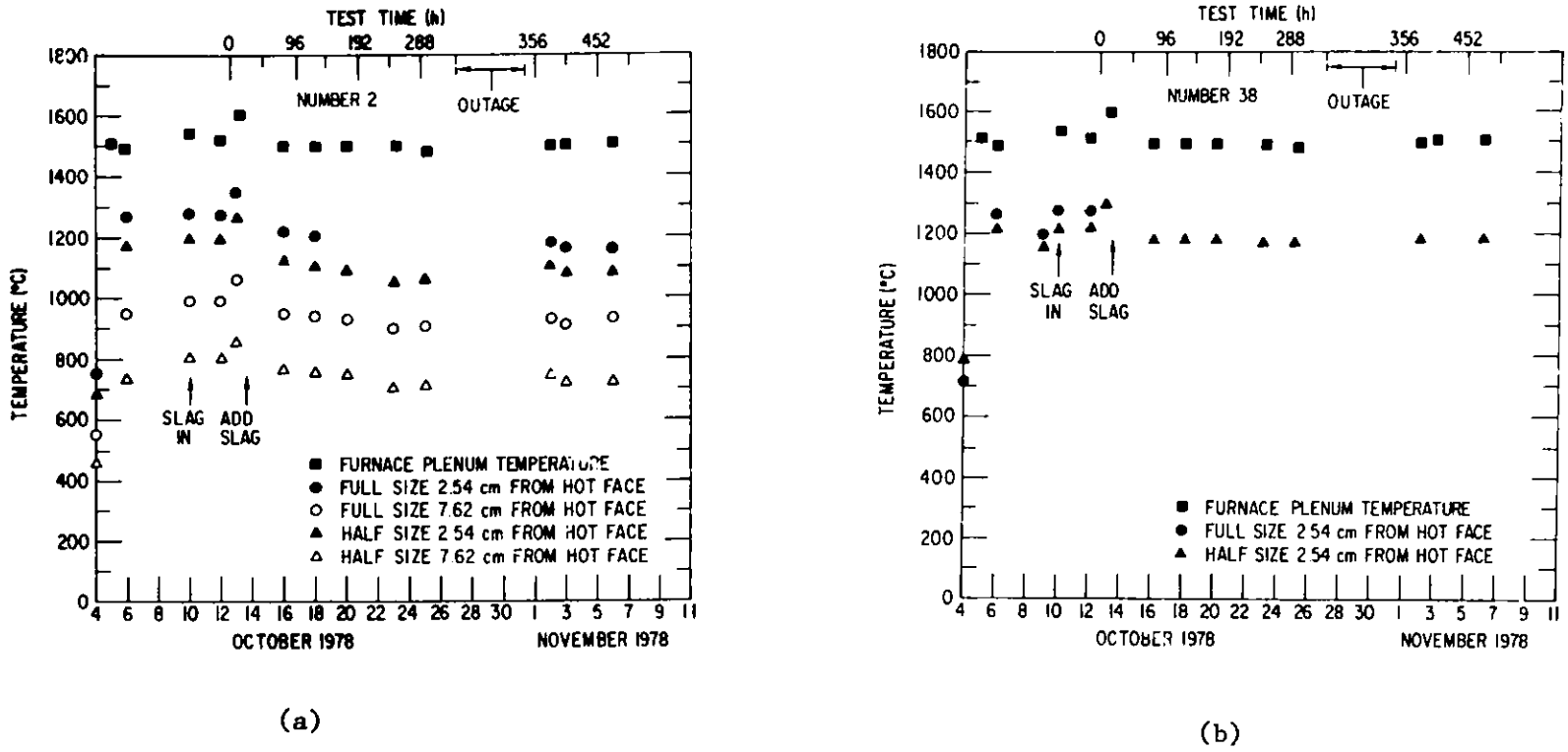


Fig. 2. Furnace Plenum and Midheight Brick Temperatures of the Fused-cast Refractories as a Function of Time During Test Run 10. (a) Alumina (number 2), (b) alumina-chromia (number 38), and (c) chrome-spinel (number 22). ANL Neg. Nos. 306-79-286, 292, 289.

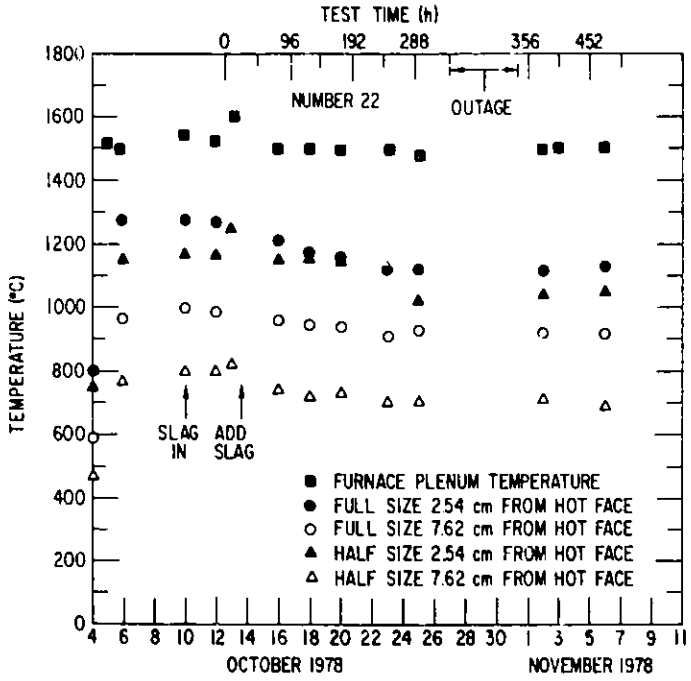
TEST TIME (h)
0
96
192
288
356
452
NUMBER 22
OUTAGE
TEMPERATURE (°C)
1800
1600
1400
1200
1000
800
600
400
200
0
SLAG IN
ADD SLAG
FURNACE PLENUM TEMPERATURE
FULL SIZE 2.54 cm FROM HOT FACE
FULL SIZE 7.62 cm FROM HOT FACE
HALF SIZE 2.54 cm FROM HOT FACE
HALF SIZE 7.62 cm FROM HOT FACE
4 6 8 10 12 14 16 18 20 22 24 26 28 30 1 3 5 7 9 11
OCTOBER 1978
NOVEMBER 1978

(c)

Fig. 2
(contd.)

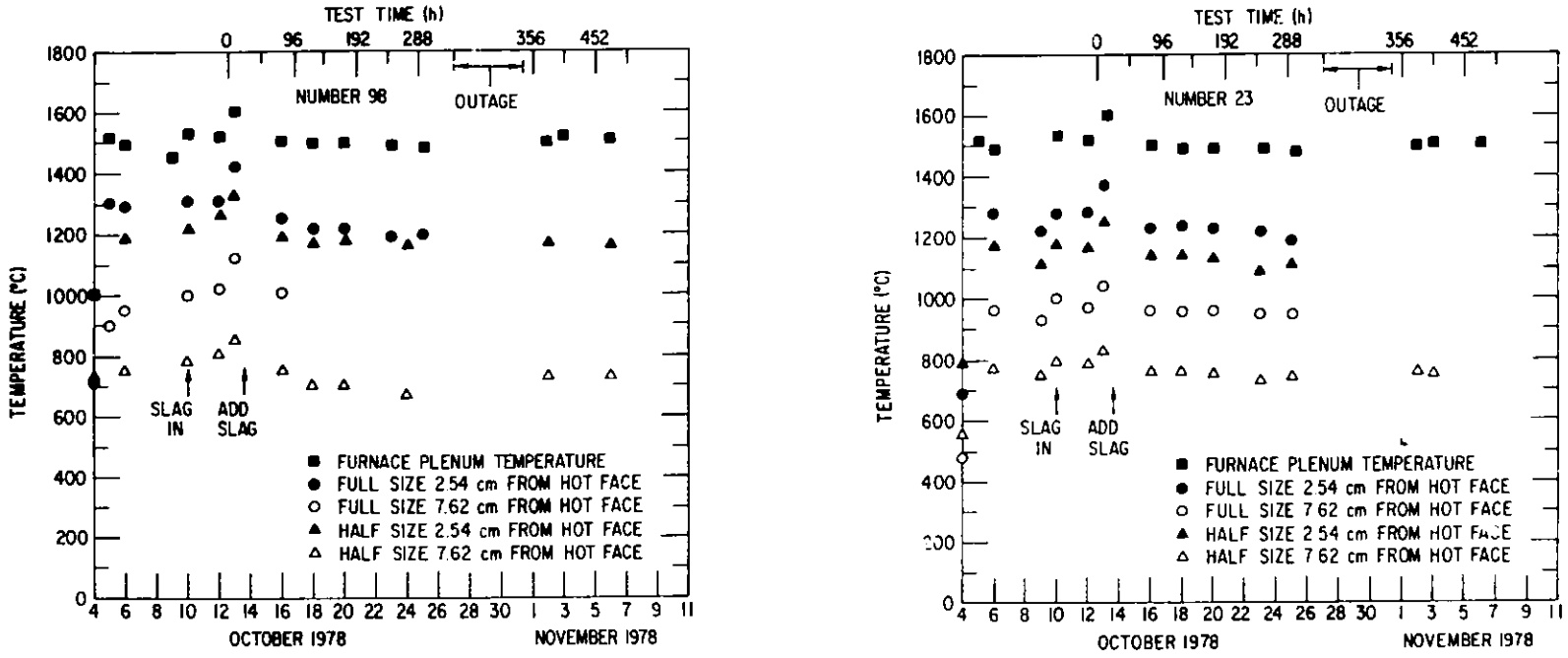


(a) (b)

Fig. 3. Furnace Plenum and Midheight Brick Temperatures of the Sintered Refractories as a Function of Time During Test Run 10. (a) Magnesia-spinel (number 98), (b) alumina-chromia (number 23), (c) magnesia-chrome (number 20), and (d) magnesia-chrome (number 29). ANL Neg. Nos. 306-79-295, 290, 288, 291.

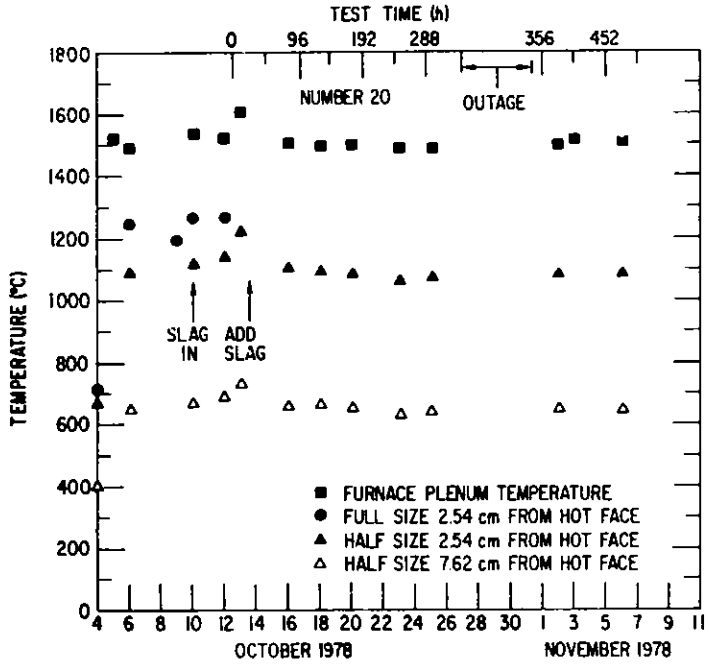


(c)

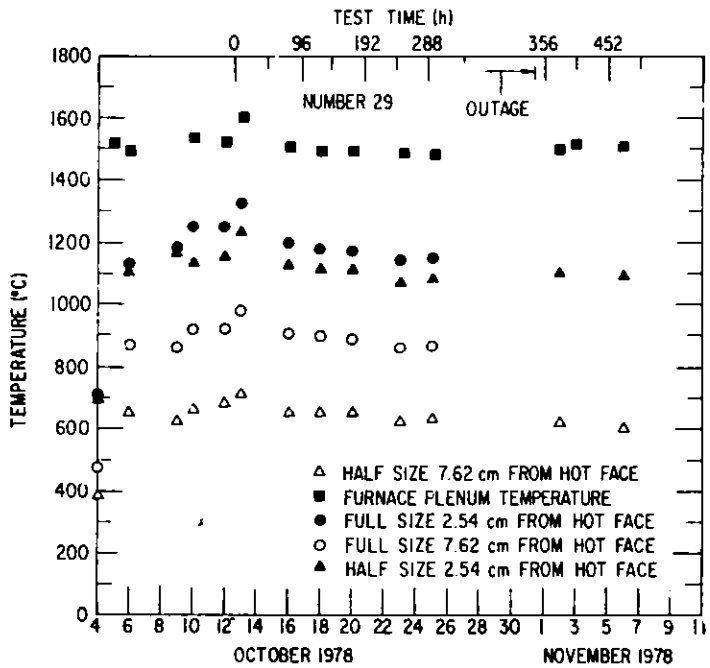


(d)

Fig. 3.

(contd.)

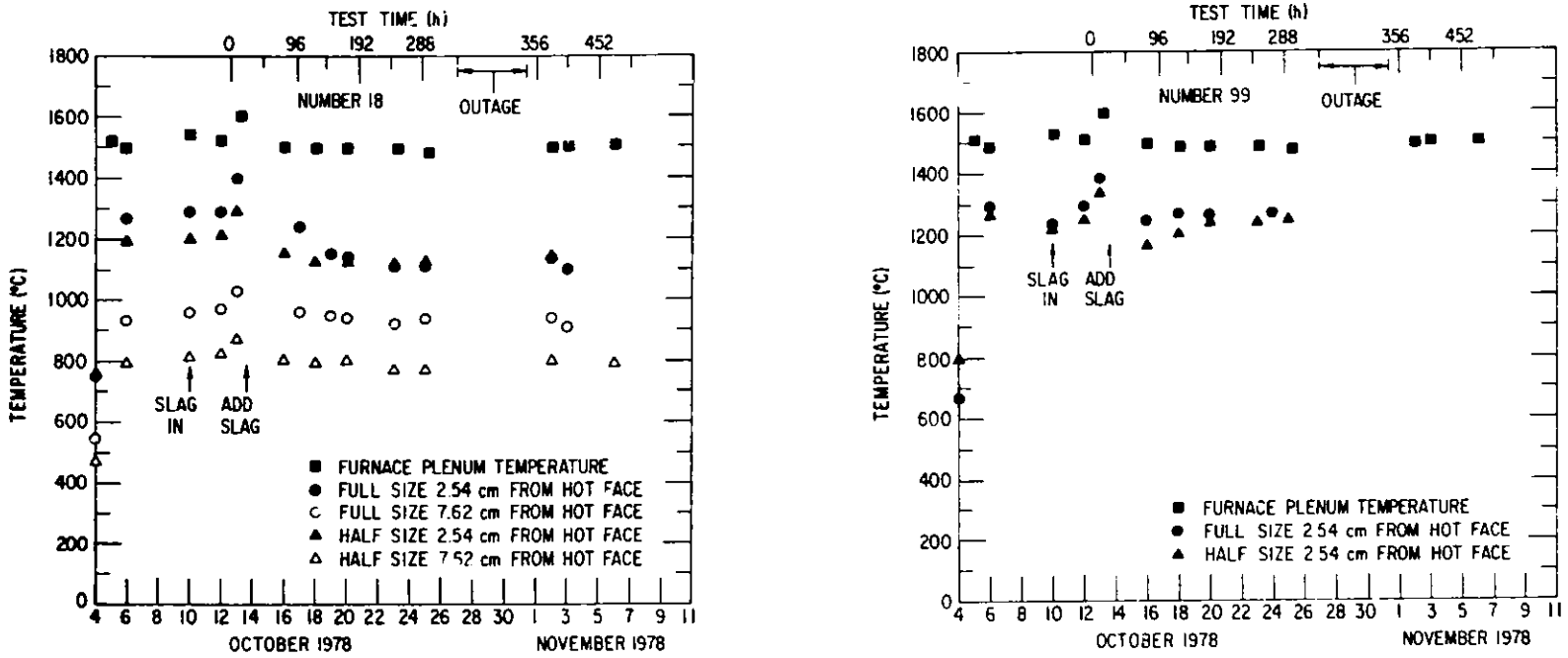


(a) (b)

Fig. 4. Furnace Plenum and Midheight Brick Temperatures of the Ramming Mixes as a Function of Time During the Test. (a) Phosphate-bonded chrome-ore (number 18), (b) silicate-bonded chrome-ore (number 99), (c) alumina-chromia (number 96), and (d) magnesia (number 97). ANL Neg. Nos. 306-79-287, 296, 293, 294.

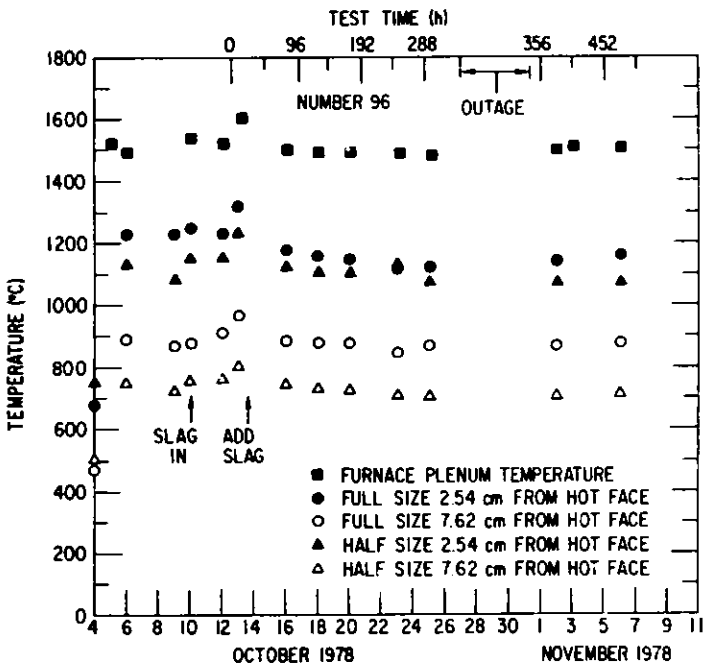


(c)

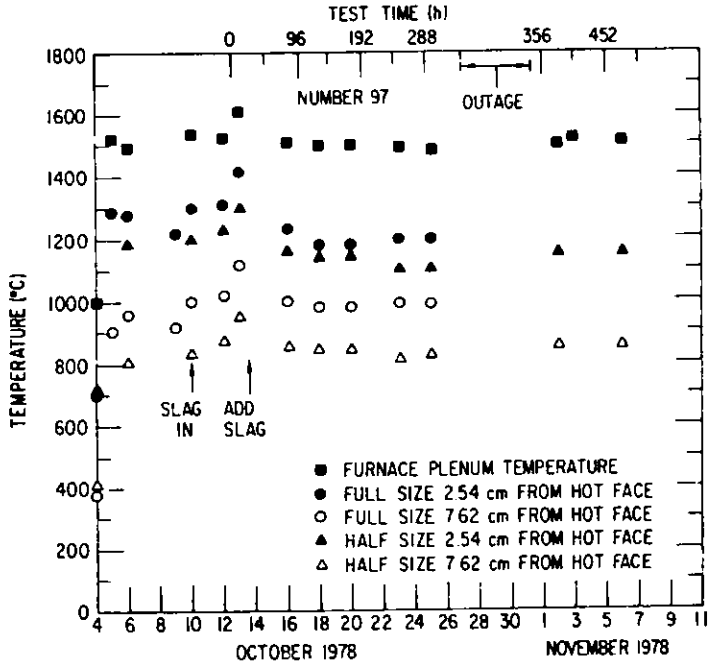


(d)

Fig. 4.
(contd.)

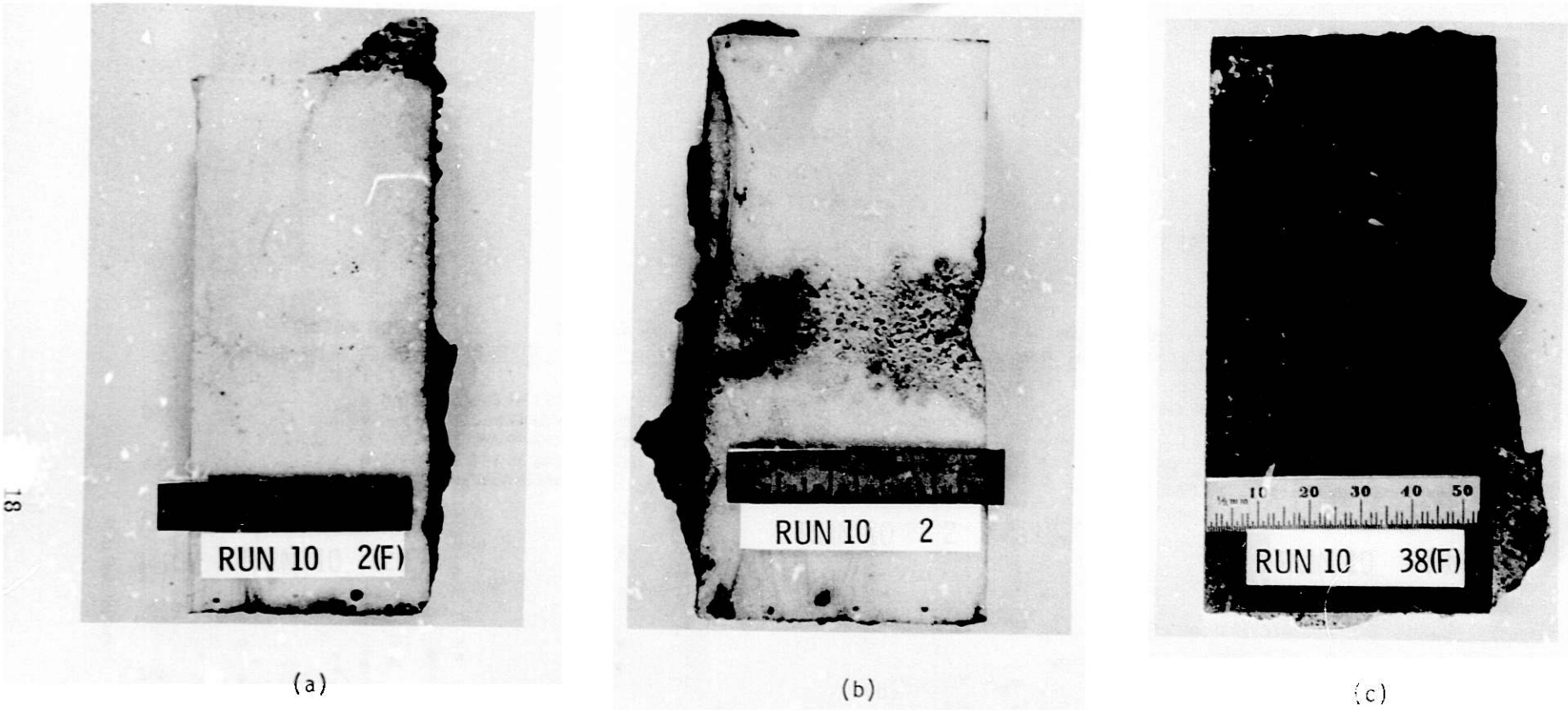


Fig. 5. Cut Sections (Entire Length of Brick is not Shown) from Fused-cast Refractories. (a) and (b), Full- and 1/2-length alumina (number 2), (c) and (d) full- and 1/2-length alumina-chromia (number 38), (e) and (f) full- and 1/2-length chrome-spinel (number 22). The right face of the bricks in (a) and (c)-(f) and the left face of the brick in (b) were exposed to the slag, which can be seen adhering to all the bricks. A chunk of material has spalled out of the sample pictured in (d) at the upper slag line. ANL Neg. Nos. 306-79-278, 279.

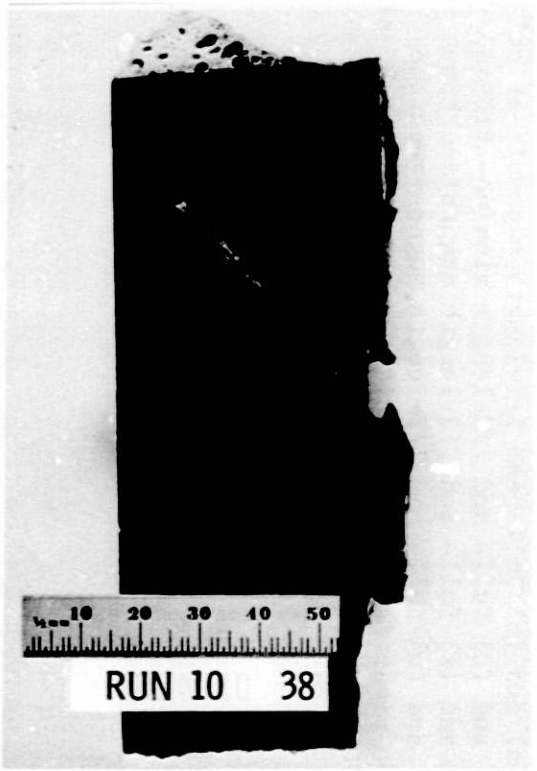


(d)

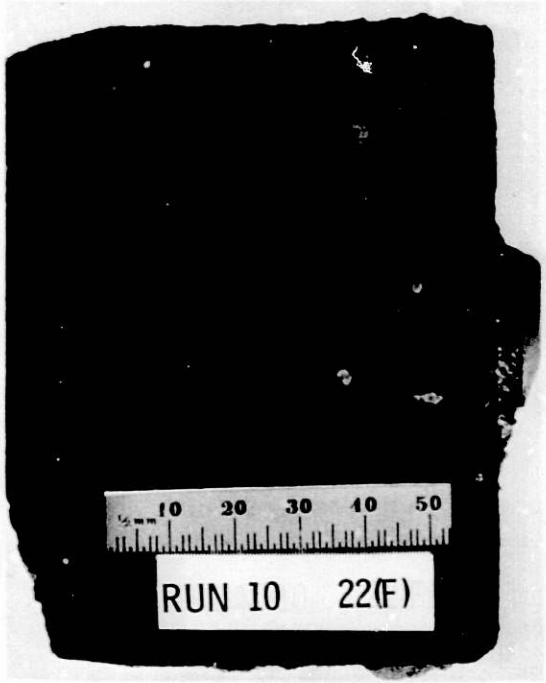


(e)

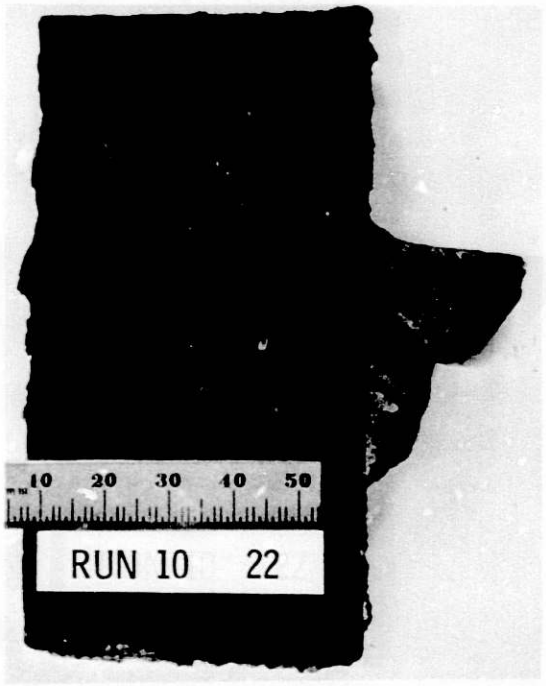


(f)

Fig. 5.
(contd.)

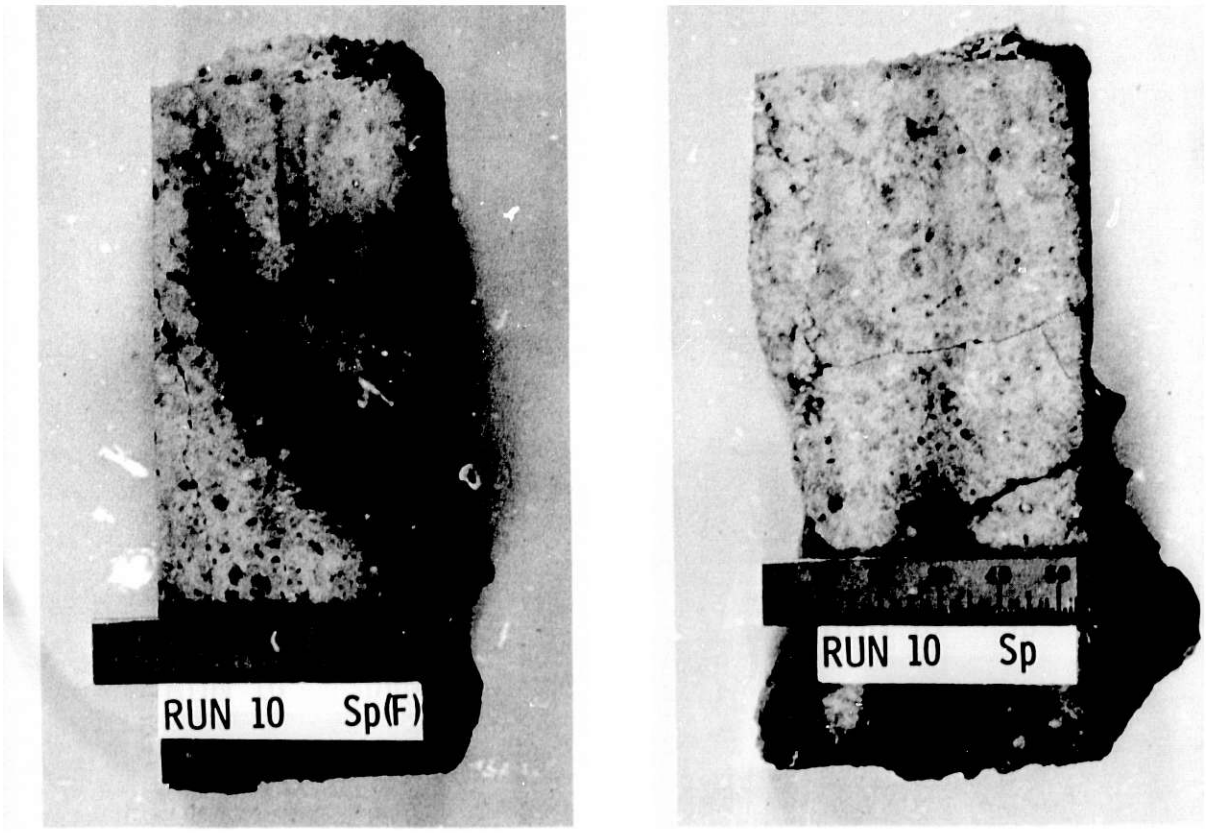


(a) (b)

Fig. 6. Cut Sections (Entire Length of Brick is not Shown) from Sintered Refractories. (a) and (b) Full- and 1/2-length magnesia-spinel (number 98), (c) and (d) full- and 1/2-length alumina-chromia (number 23), (e) and (f) full- and 1/2-length magnesia-chrome (number 20), (g) and (h) full- and 1/2-length magnesia-chrome (number 29). The right face of each brick was exposed to the slag. ANL Neg. Nos. 306-79-280, 281, 282.

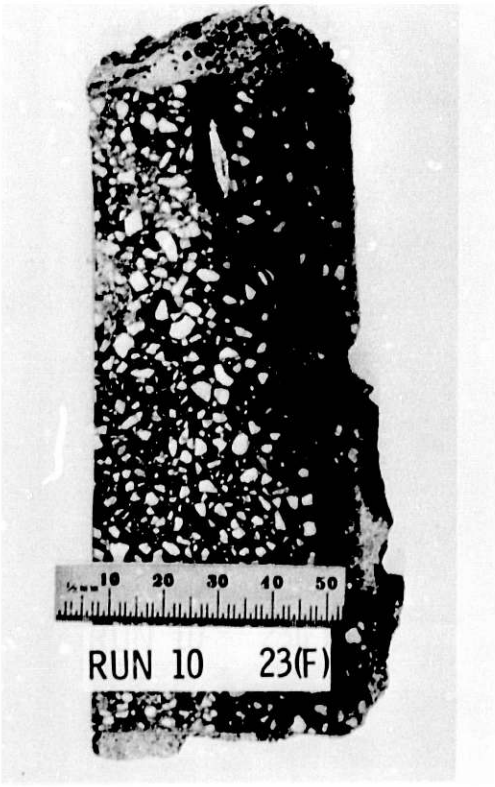


(c)

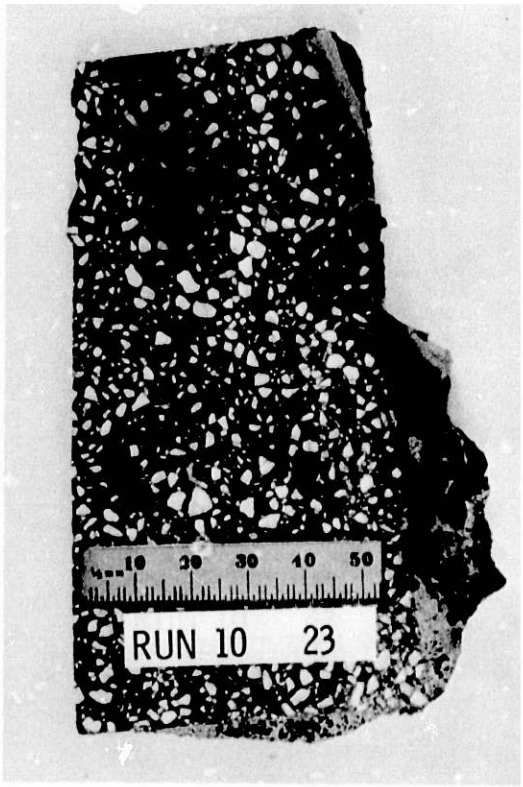


(d)

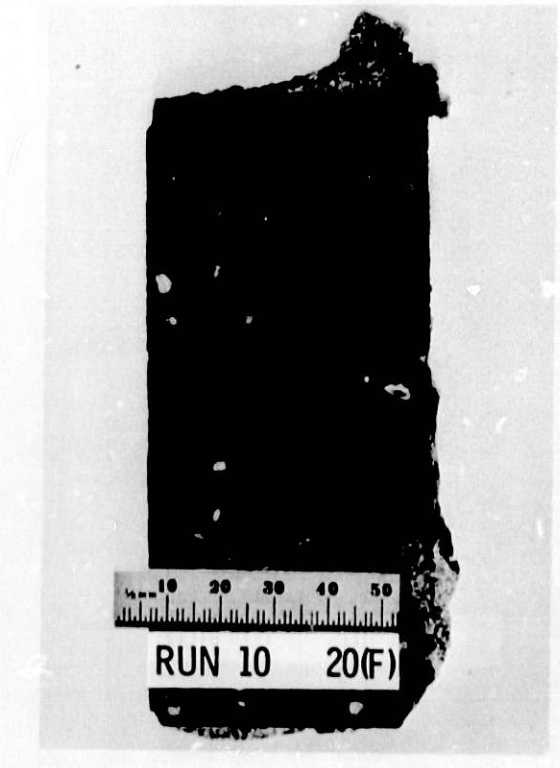


(e)

Fig. 6 (contd.)

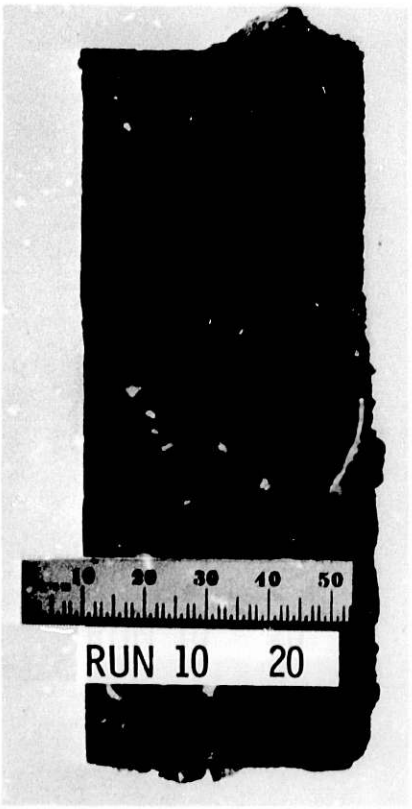


(f)

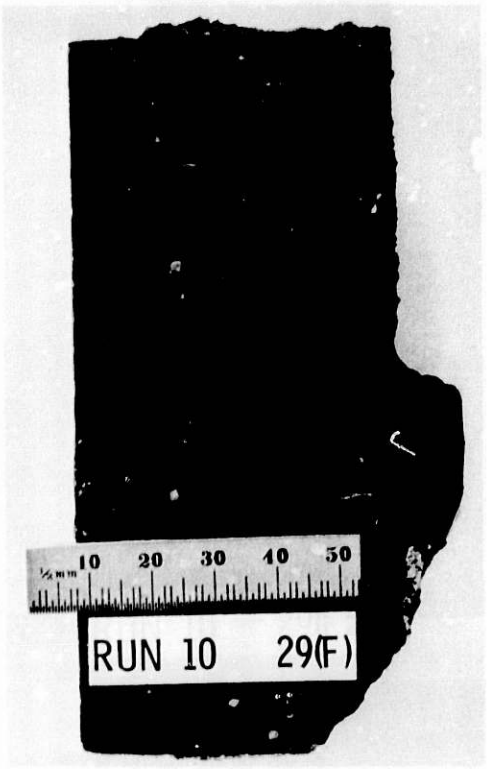


(g)

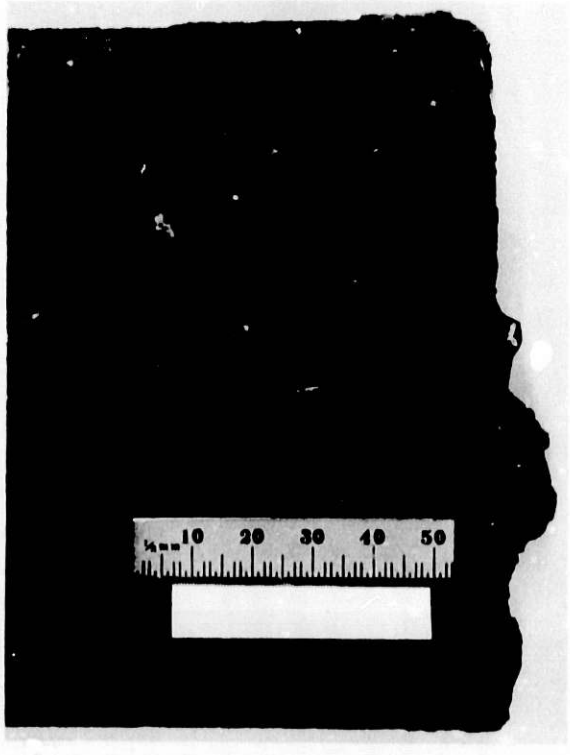


(h)

Fig. 6 (contd.)

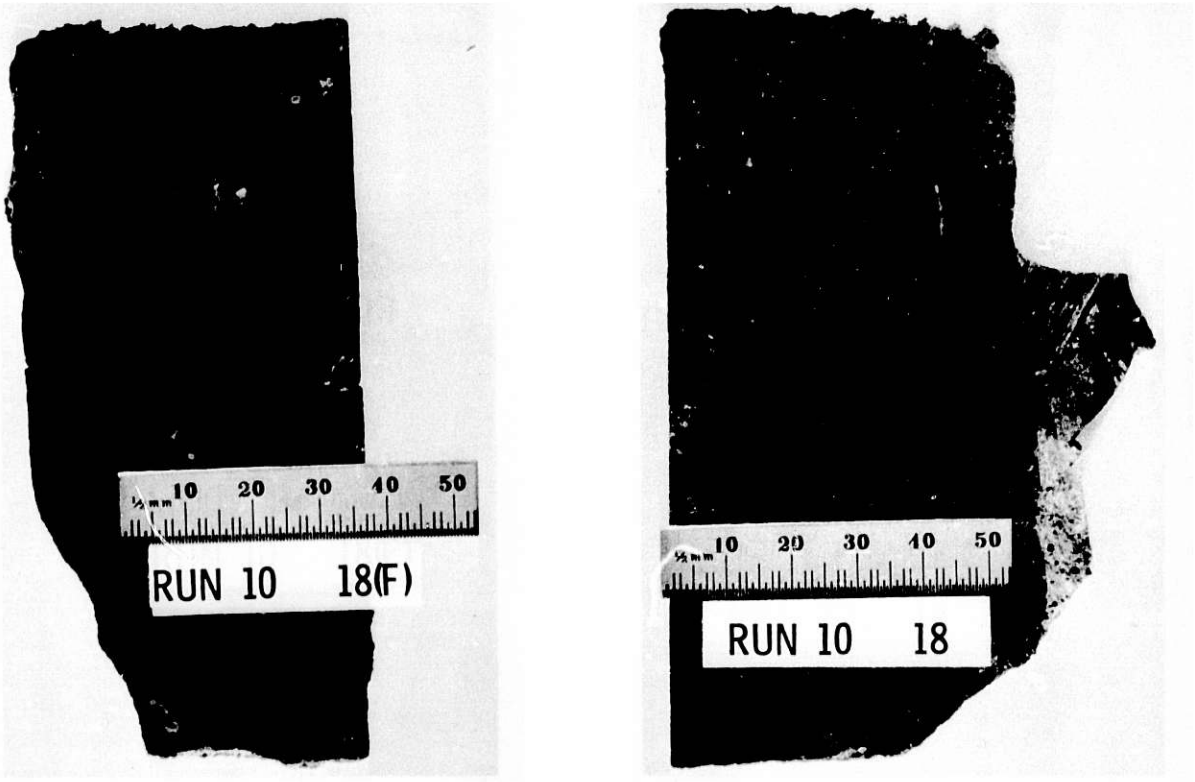


Fig. 7. Cut Sections (Entire Length of Brick is not Shown) from Ramming Mixes. (a) and (b) Full- and 1/2-length phosphate-bonded chrome-ore (number 18), (c) and (d) full- and 1/2-length silicate-bonded chrome-ore (number 99), (e) and (f) full- and 1/2-length alumina-chromia (number 96), (g) and (h) full- and 1/2-length magnesia (number 97). The right face of the bricks in (b) and (d)-(h) and the left face of the bricks in (a) and (c) were exposed to the slag.
ANL Neg. Nos. 306-79-283, 285, 284.


(c)


(d)


(e)

Fig. 7 (contd.)

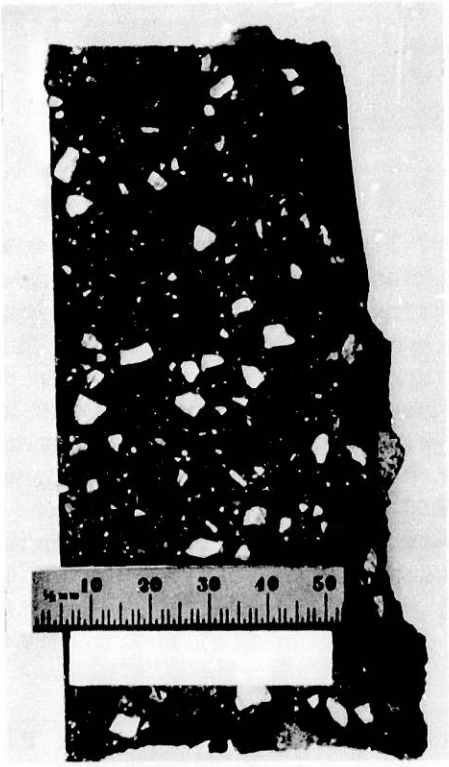

(f)

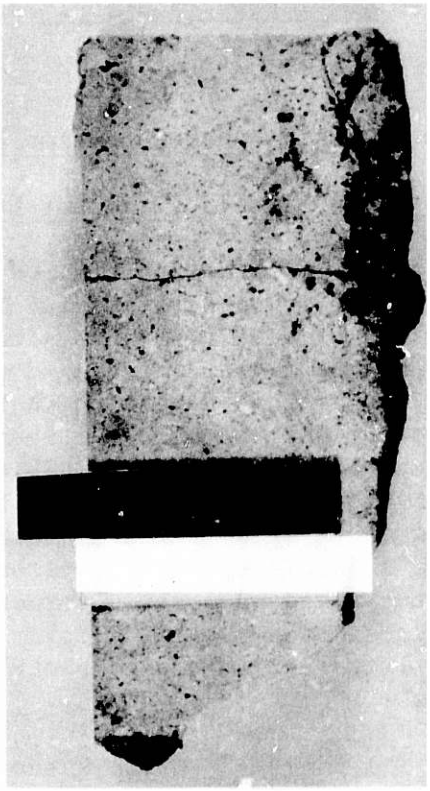

(g)

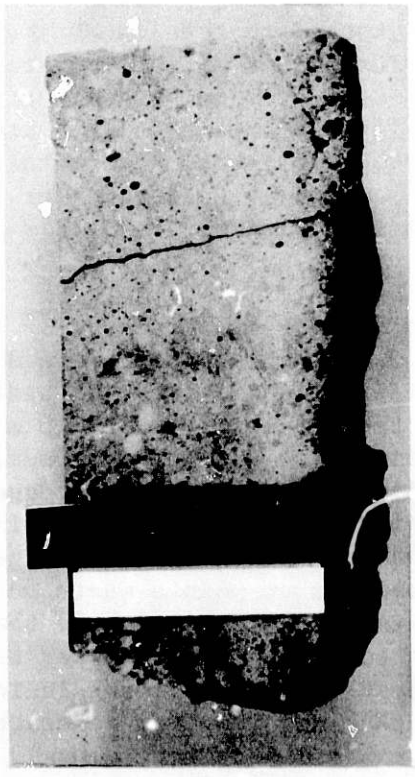

(h)

Fig. 7 (contd.)

Task C -- Development and Application of Nondestructive Evaluation Methods for Coal-conversion Processes *(W.A. Ellingson, K.J. Reimann, C.A. Youngdahl and R.R. Roberts)*

1. Erosive-wear Detection and Monitoring

a. Metallic Transfer Lines

*(1) Ultrasonic Studies -- Pilot Plants.* Much of this quarter has been invested in preparation and installation of equipment for a new in-situ field study of erosion and erosion-monitoring apparatus and techniques at the Morgantown (West Virginia) Energy Technology Center (METC). The inlet region of the cyclone separator in the effluent line of the producer coal-gasification unit at METC has been instrumented with 21 ultrasonic waveguides and transducers. The ANL erosive-wear scanning system formerly used at the Synthane Pilot Plant has been reworked and is being used to monitor the transducer array remotely from the METC producer control room. The producer's data-acquisition system has been coupled to the ANL monitoring system to provide automatic temperature compensation of the indicated thickness values and a graphic display of wall thicknesses at the measuring sites. Installation was completed March 31, and initial testing is in progress.

A paper, "Erosion Rates and Patterns of the HYGAS Pilot Plant's Effluent Cyclone" (J.L. Jones and J.M. Arnold of HYGAS, and C.A. Youngdahl of ANL), was completed, presented by C.A. Youngdahl at the NACE/DOE/LBL Conference on Corrosion/Erosion of Coal Conversion System Materials in Berkeley, CA, January 24-26, 1979, and is being published in the Proceedings of the meeting. Another paper, "Long Term Erosion Monitoring of Metallic Conduits by Ultrasonic Pulse-Echo Techniques" (C.A. Youngdahl and W.A. Ellingson), has been drafted for the 12th Symposium on Nondestructive Evaluation, to be held in San Antonio, TX in April 1979; and a talk, "Ultrasonic Instrumentation Techniques for the Measurement of Erosion of Metallic Components", has been prepared by C.A. Youngdahl and W.A. Ellingson for the 25th International Instrumentation Symposium scheduled for May, 1979 in Anaheim, CA.

*(2) Ultrasonic Studies - Scattering of Acoustic Waves from Rough Surfaces.* Efforts during this period were directed towards improvement of scattering-data manipulation and display in order to obtain more information. As a first step the spectrum of a rough surface was divided by the spectrum from a reflection of a smooth surface. The resultant curve (Fig. 8) shows periodic dips at interference frequencies determined by the depth of the grooves. This computer technique eliminated the effects of transducer and material characteristics, but exaggerated the height of some peaks in the frequency spectrum at points where one small value was divided by another. Moreover, this method approximated the frequency-spectrum curves by fitting straight lines to them. The computer technique was subsequently revised in order to increase the spectral resolution from 5 points per MHz to approximately 40 points. The new computer-generated frequency spectrum, using the fast Fourier transform, much more closely resembles frequency spectra obtained by an analog spectrum analyzer. Figure 9 compares spectra generated by the original and the revised computer programs. In the latter spectrum

(Fig. 9b), a more detailed fine structure is discernible. The two main dips at 5.3 and 5.9 MHz are caused by groove-depth dimensions [longitudinal (L-) waves and L- plus shear-wave interference, respectively)]. It is obvious, however, that it would be difficult to correlate the spectral results with roughness dimensions for an unknown sample. To get additional information, the RF signal from the rough surface was cross-correlated with the signal from a smooth surface. This technique, used widely in communications technology for noise suppression, enables one to determine arrival times of different pulses more accurately. Figure 10 shows the cross-correlation curve of the signal with the frequency spectrum exhibited in Fig. 9. The arrival times of different parts of the total pulse can now be used to calculate the different interference frequencies and correlate them with physical dimensions. However, the actual pulse arrival time cannot be determined accurately because of the high-frequency component, which only allows an estimate of the actual position of the peak of the envelope.

A different approach was therefore tried. Figure 11a shows an average waveform of the echo from a rough surface when insonified through the material. The modulation of the high frequency carries information related to the rough surface, while the high-frequency components are mainly frequencies generated by the transducer. The function shown in Fig. 11 may be expressed as f(t) and assumed to consist of the transducer characteristic g(t) and the rough-surface and material characteristic h(t); these expressions are related by the convolution integral

$$f(t) = \int_{-\infty}^{\infty} g(\tau)\, h(t-\tau t)\, d\tau$$

Since the transducer characteristic is unimportant for rough-surface investigation, it is desirable to eliminate it. This can be done by deconvolution, using inverse fast Fourier transform techniques:

$$H(j\omega) = \frac{F(j\omega)}{G(j\omega)} = \frac{\int_{-\infty}^{\infty} e^{j\omega\tau} \left[ \int_{-\infty}^{\infty} g(\tau)\, h(t-\tau)\, d\tau \right] dt}{\int_{-\infty}^{\infty} g(\tau)\, e^{-j\omega\tau}\, d\tau}$$

$$= \frac{\int_{-\infty}^{\infty} g(\tau) \left[ \int_{-\infty}^{\infty} e^{-j\omega\tau}\, h(t-\tau) dt \right] d\tau}{\int_{-\infty}^{\infty} g(\tau)\, e^{-j\omega\tau}\, d\tau}$$

$$= \frac{\int_{-\infty}^{\infty} g(\tau)\ e^{-j\omega\tau} \left[ \int_{-\infty}^{\infty} e^{-j\omega\tau}\ h(t)\ dt \right] d\tau}{\int_{-\infty}^{\infty} g(\tau)\ e^{-j\omega\tau}\ d\tau}$$

and

$$h(t) = \frac{1}{2\pi} \int_{-\infty}^{\infty} H(j\omega)\ e^{j\omega\tau}\ d\tau$$

The result of the deconvolution of the waveform in Fig. 11a is shown in Fig. 11b. Peaks of different pulses are now clearly discernable and arrival times can be more easily determined. If pulses are separated by a larger time difference as in Fig. 12a, the arrival times are even more distinguishable in their deconvolution, as seen in Fig. 12b.

When only differences in the surface roughness are of interest and a reference smooth surface is available, then the deconvolution can be modified in such a way that the smooth-surface arrival time coincides with the origin and the other arrival times are plotted as functions of the difference in time. This is achieved by subtracting the RF waveform of the smooth surface from that of the rough surface and subsequently performing the deconvolution. An example of this procedure is shown in Fig. 13. The curve is for the same samples used to obtain Fig. 11.

Future work will concentrate on using these new techniques to evaluate the roughened-surface data reported previously.[14]

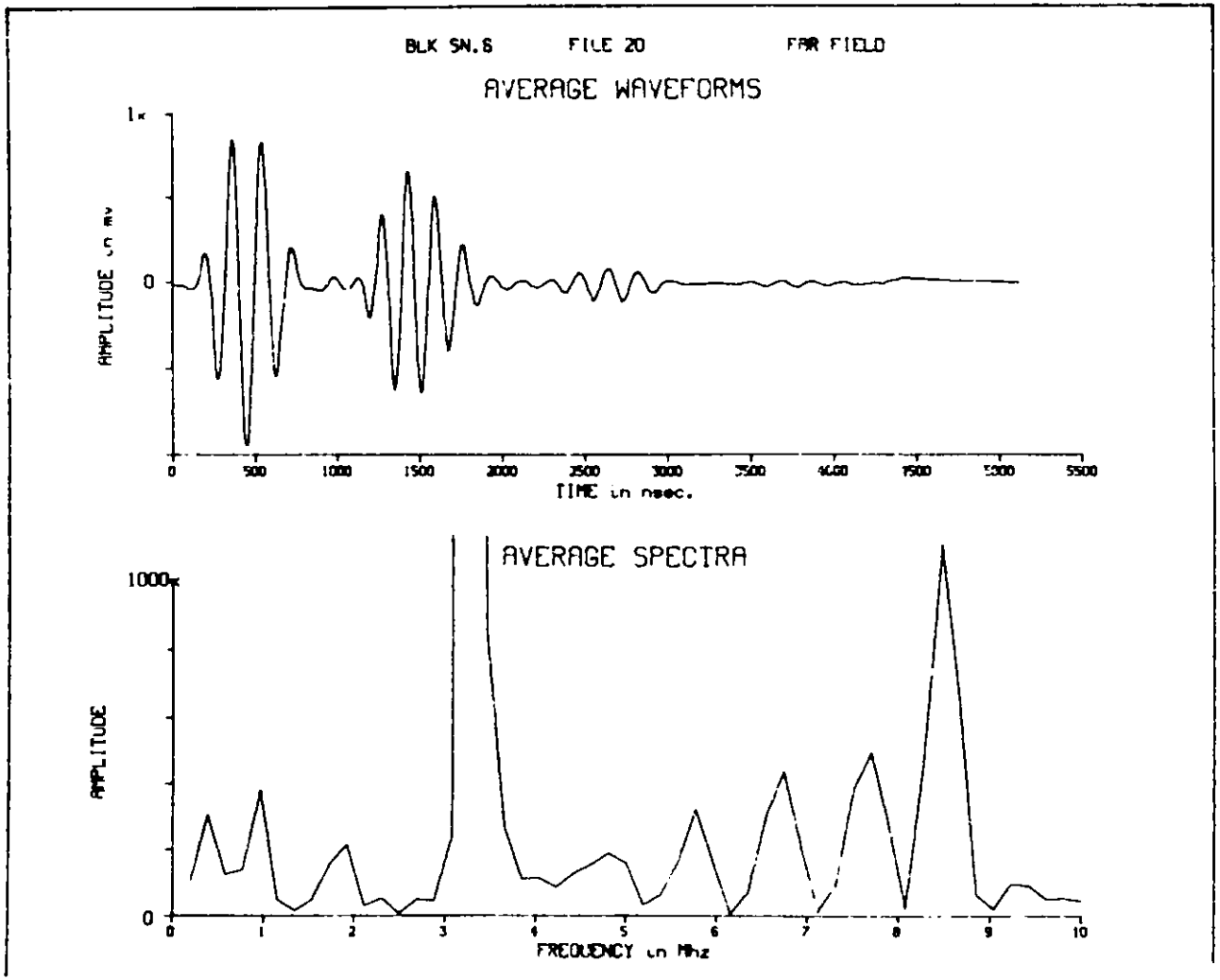


Fig. 8. RF Signal and Frequency Spectrum of Rough Surface. ANL Neg. No. 306-79-526.

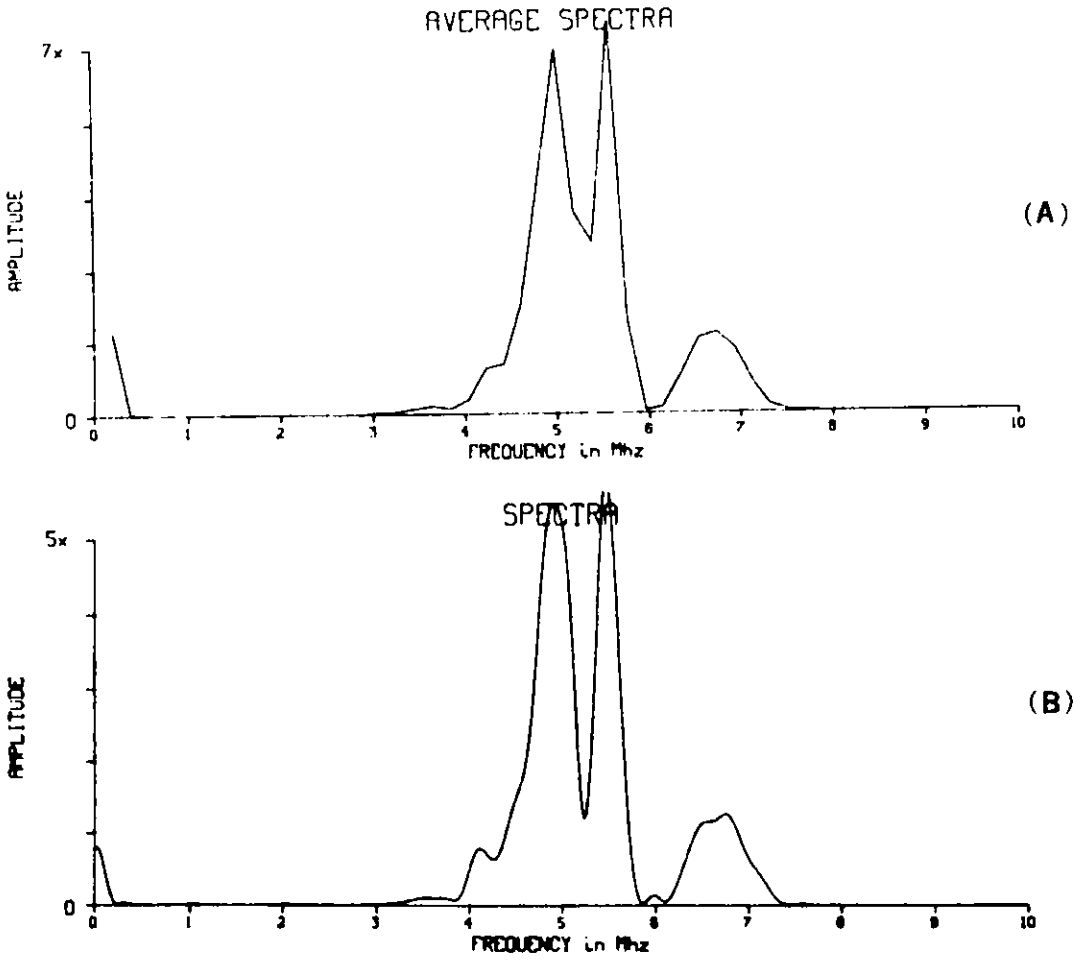


Fig. 9. Frequency Spectra Obtained with (a) Old and (b) Revised Computer Program. ANL Neg. No. 306-79-532.

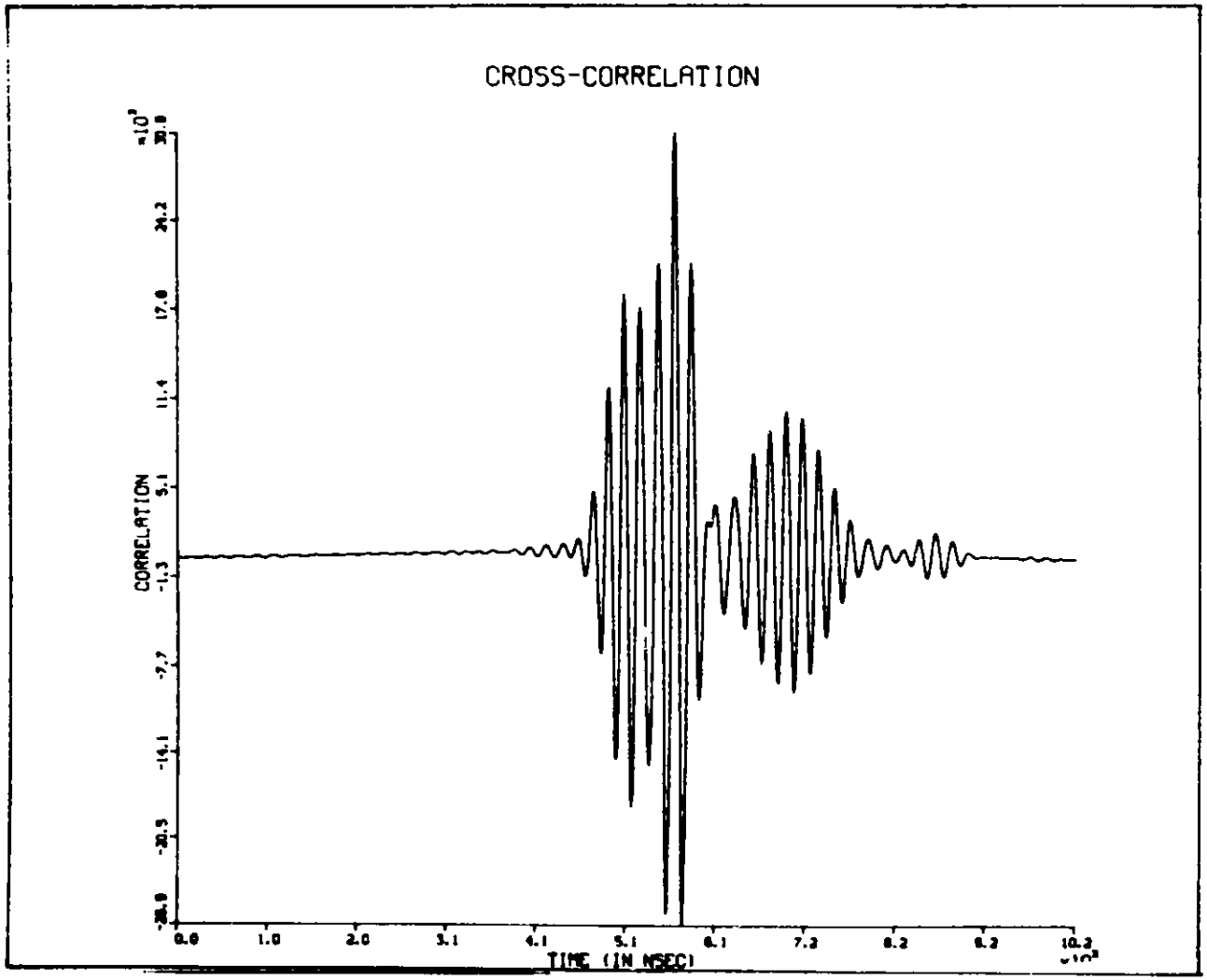


Fig. 10. Cross-correlation of RF Signal for Sample of Fig. 9. ANL Neg. No. 306-79-527.

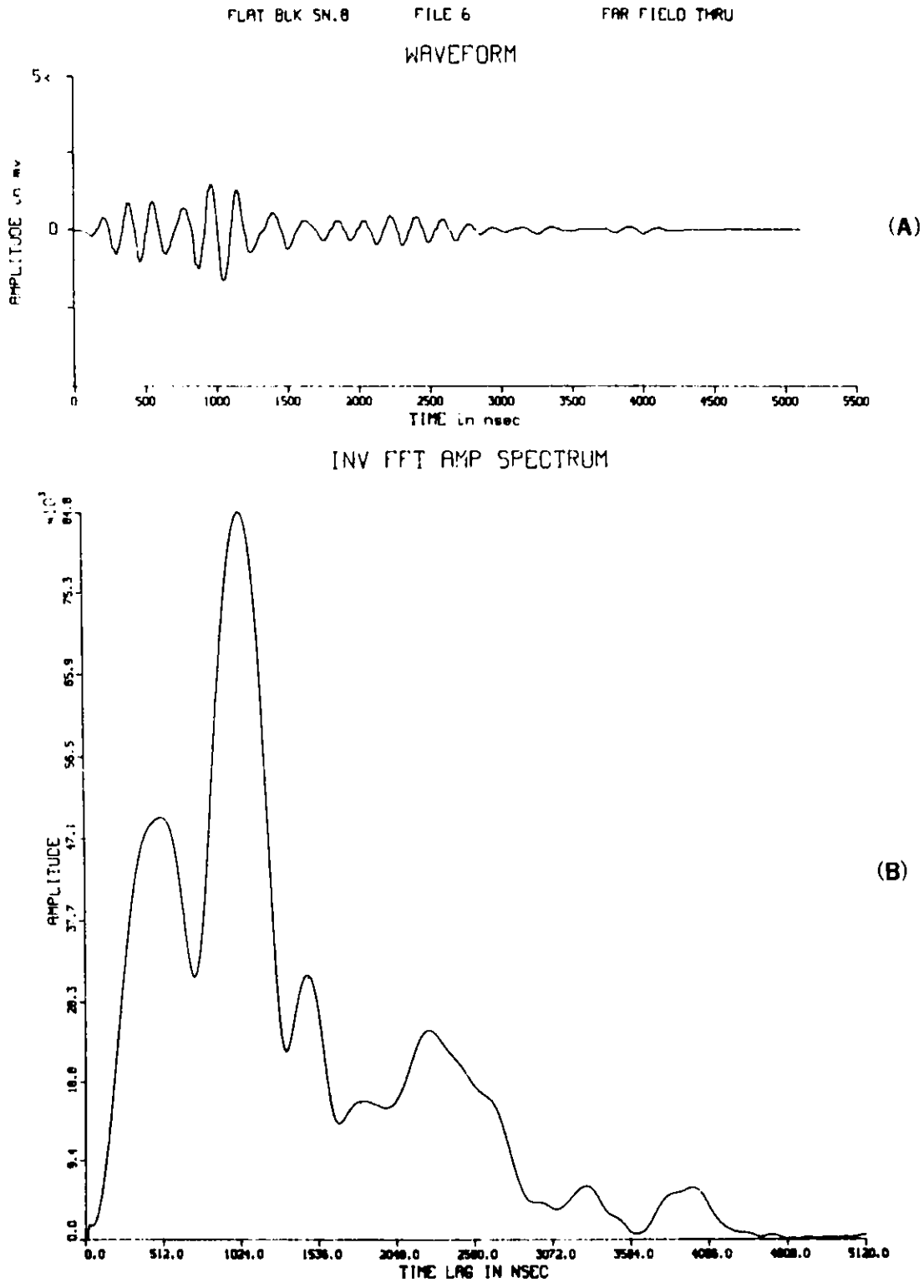


Fig. 11. (a) RF Signal of Rough Surface Insonified through Metal; (b) Deconvoluted Signal of (a). ANL Neg. No. 306-79-528.

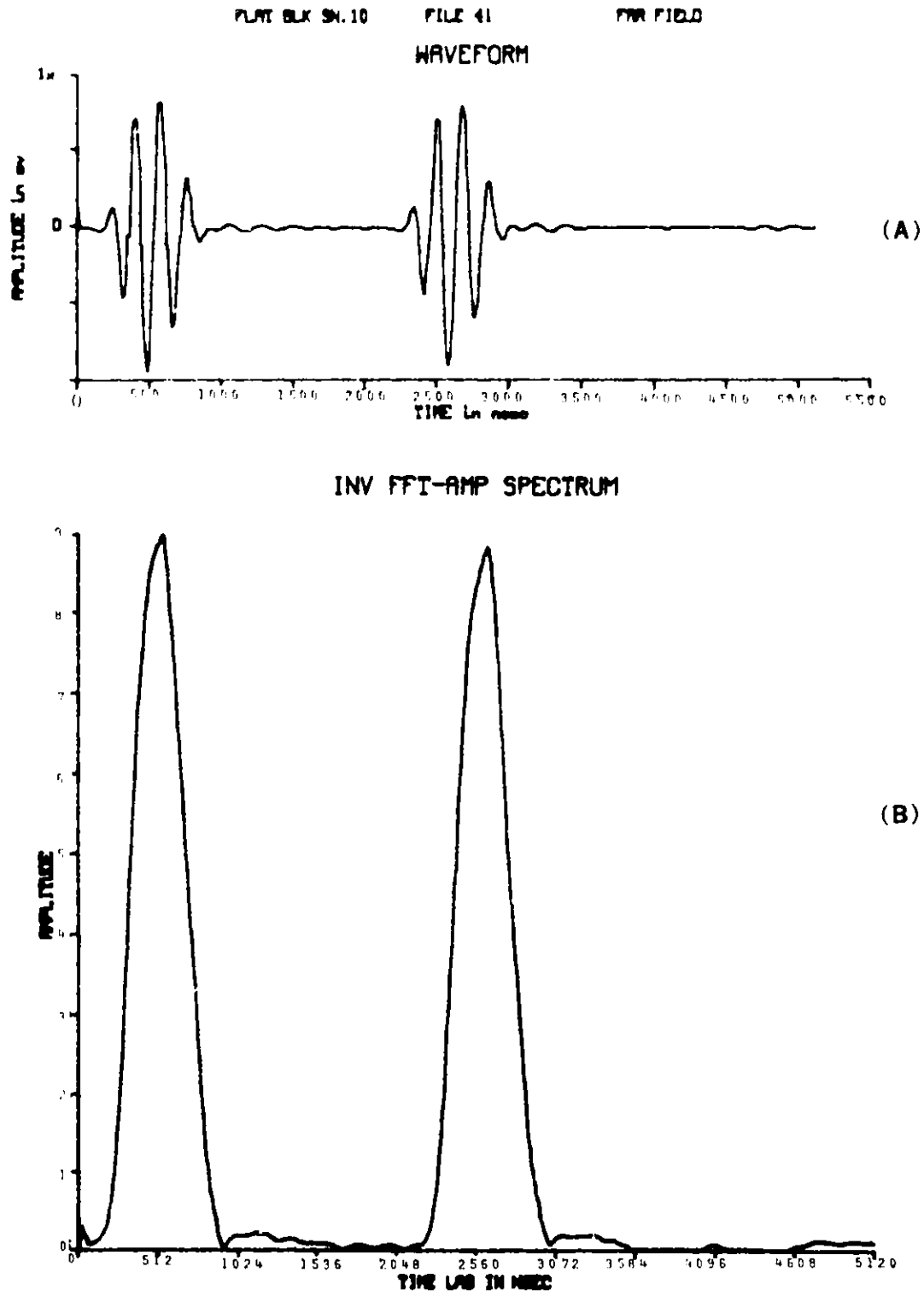


Fig. 12. (a) RF Signal of Rough Surface (Water-Steel Interface); (b) Deconvoluted Signal of (a). ANL Neg. No. 306-79-552.

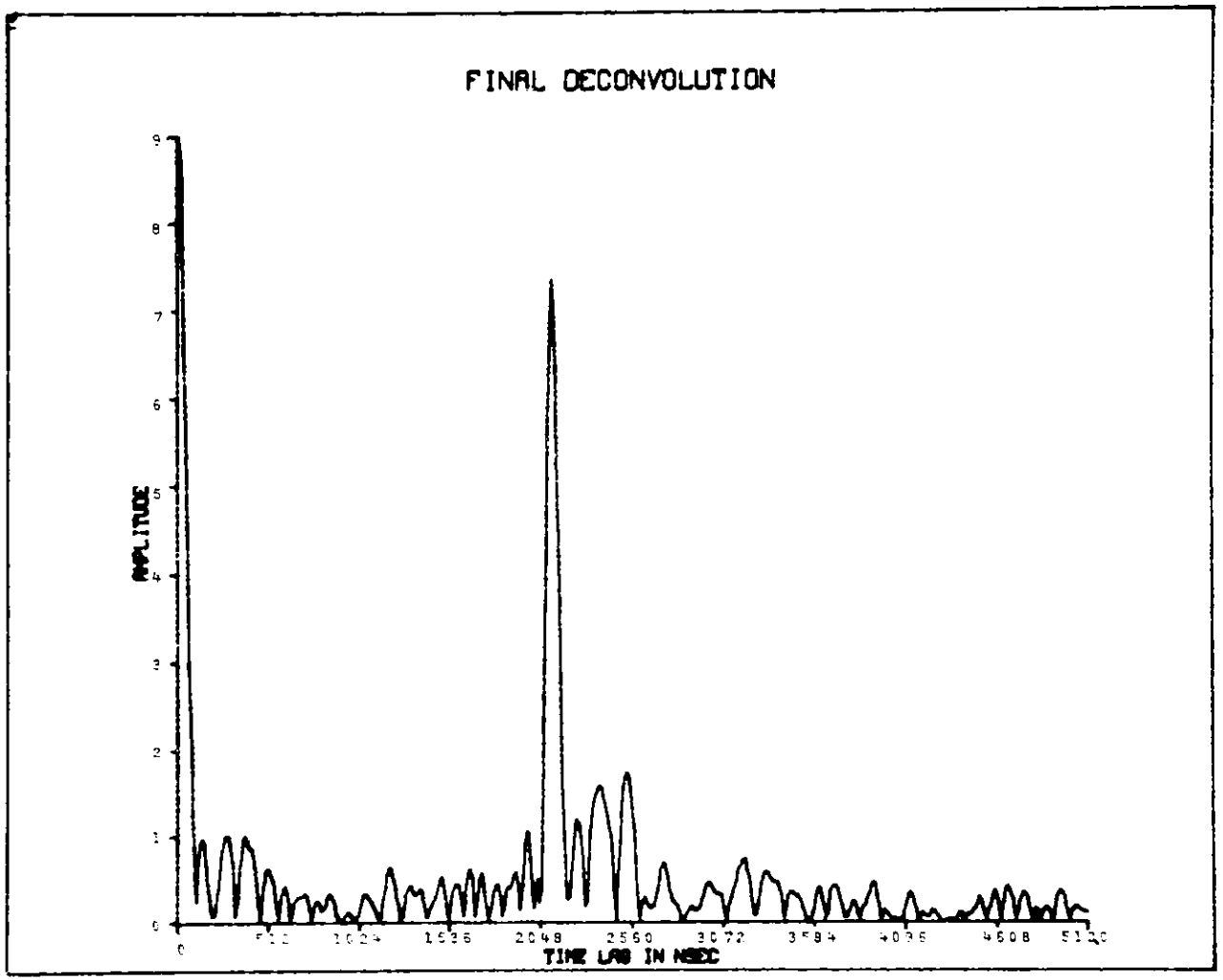


Fig. 13. Deconvoluted Signal of Fig. 12 with Origin Adjusted to Smooth-surface Reflection. ANL Neg. No. 306-79-553.

## 2. Refractory Installation Practices

### a. Detection of Thermally Induced Acoustics from Refractory Concrete Materials

Work has continued this quarter on evaluation of acoustic emission as a means to control the firing schedule of thick castable refractory-concrete linings of the type envisioned for use in the main process vessels of coal-conversion (gasification and liquefaction) and some direct-combustion (primarily pressurized fluid-bed) systems.

The data obtained previously[9,10] from a rapidly heated 15-cm-thick, 26-cm-wide, 25-cm-high monolithic panel cast of high-density Castolast G (Fig. 14) was further reduced and plans were made to cast a similar panel under precuring conditions selected to create a large spall.

The temperature-time profiles at various distances from the hot face are shown in Fig. 15. The heating rate is not fast enough to produce a nonlinear temperature distribution through the test panel. This can be seen by noting that when the maximum hot-face temperature has been reached, no lag is observed before the internal temperatures level off.

It has been suggested[9] that a potential source of acoustic emissions from within the refractory material is the fracture of bonds between the matrix and the individual grains, caused in part by the tensile forces built up when the refractory material undergoes its characteristic shrinkage reversal. The shrinkage reversal takes place over a temperature range which is reached at different times through the refractory thickness as the sample is being heated. The linear expansion curve for Castolast G (showing the shrinkage reversal) was obtained from Harbison Walker[11] and is shown in Fig. 16. The time to reach a specified internal temperature can be obtained from Fig. 15 and will yield the rate at which a given temperature range was driven through the refractory thickness. Figure 17 is a plot of the time required to reach two temperatures, 250 and 315°C, as a function of distance from the hot face. The average slope indicates that in this test, the shrinkage-reversal temperature range (tensile-compressive interface) was driven through the refractory thickness at a rate of 4-4.5 cm/h. This suggests that 8 hours into this firing, the refractory had expanded and shrunk essentially throughout its thickness and that the entire mass should have been expanding. Figure 18 shows the superimposed plots of ringdown counts as a function of time for both the 175-kHz and the broadband transducers. It is interesting to note that between 5 and 6 hours into the heating schedule, the ringdown-count accumulation levels off. Between 8 and 9 hours the counts begin to accumulate again. This suggests that the acoustic-emission phenomenon is sensitive to the shrinkage-reversal process. The voltage level of the instrumentation (set at 0.8 V) could be set higher to discriminate between small and large events. An attempt was made to determine when large and small events occurred by amplitude distribution analysis. Figure 19 shows the characteristic slope obtained at 3, 6-1/4, 9-1/4, and 24-2/3 hours into the heating cycle and Fig. 20 shows typical distributions obtained during the quench cycle. The slopes are all close to unity and do not suggest that significant large-amplitude events have occurred. This agrees with the final visual inspection of the refractory, which indi-

cated only small surface cracks.

The additional acoustic ringdown counts which occur after the hot face has reached the maximum temperature can be accounted for by the additional crack volume which develops after the material has gone through the shrinkage-reversal process.

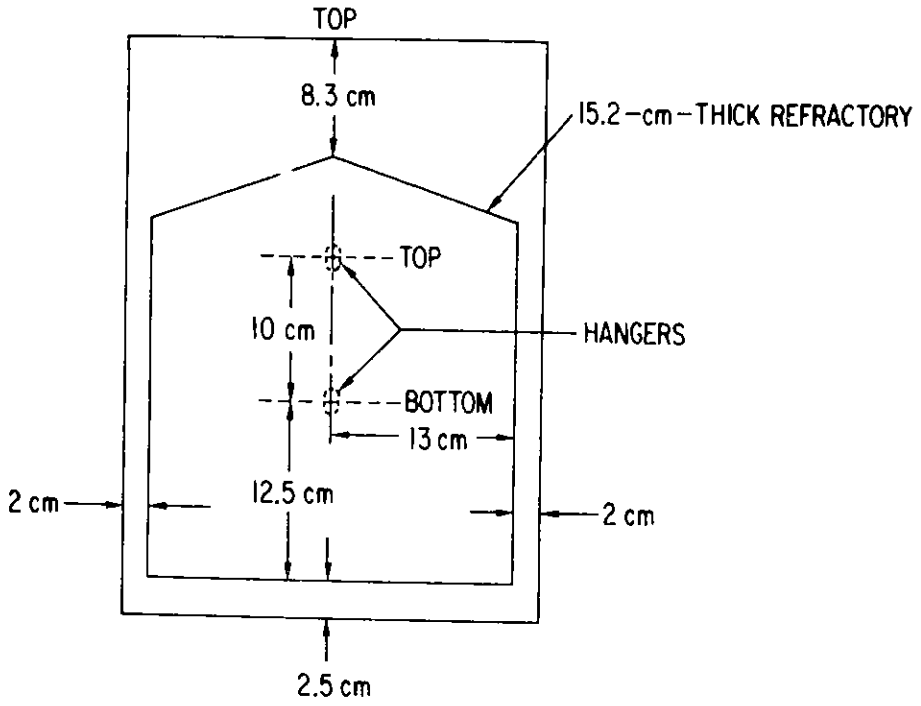


(a)

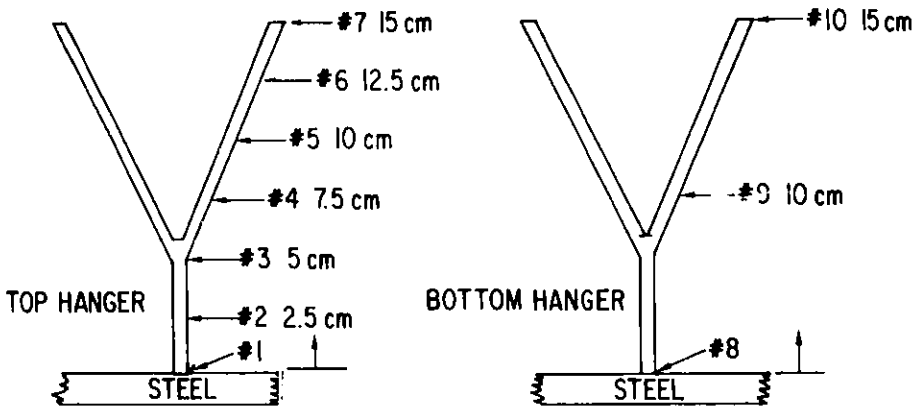


(b)

Fig. 14. (a) Dimensions of High-density Castolast G Panel. (b) Locations of Thermocouples on Top and Bottom Hangers (Hot Face at Top of Figure). MSD Neg. Nos. 65885, 65888.

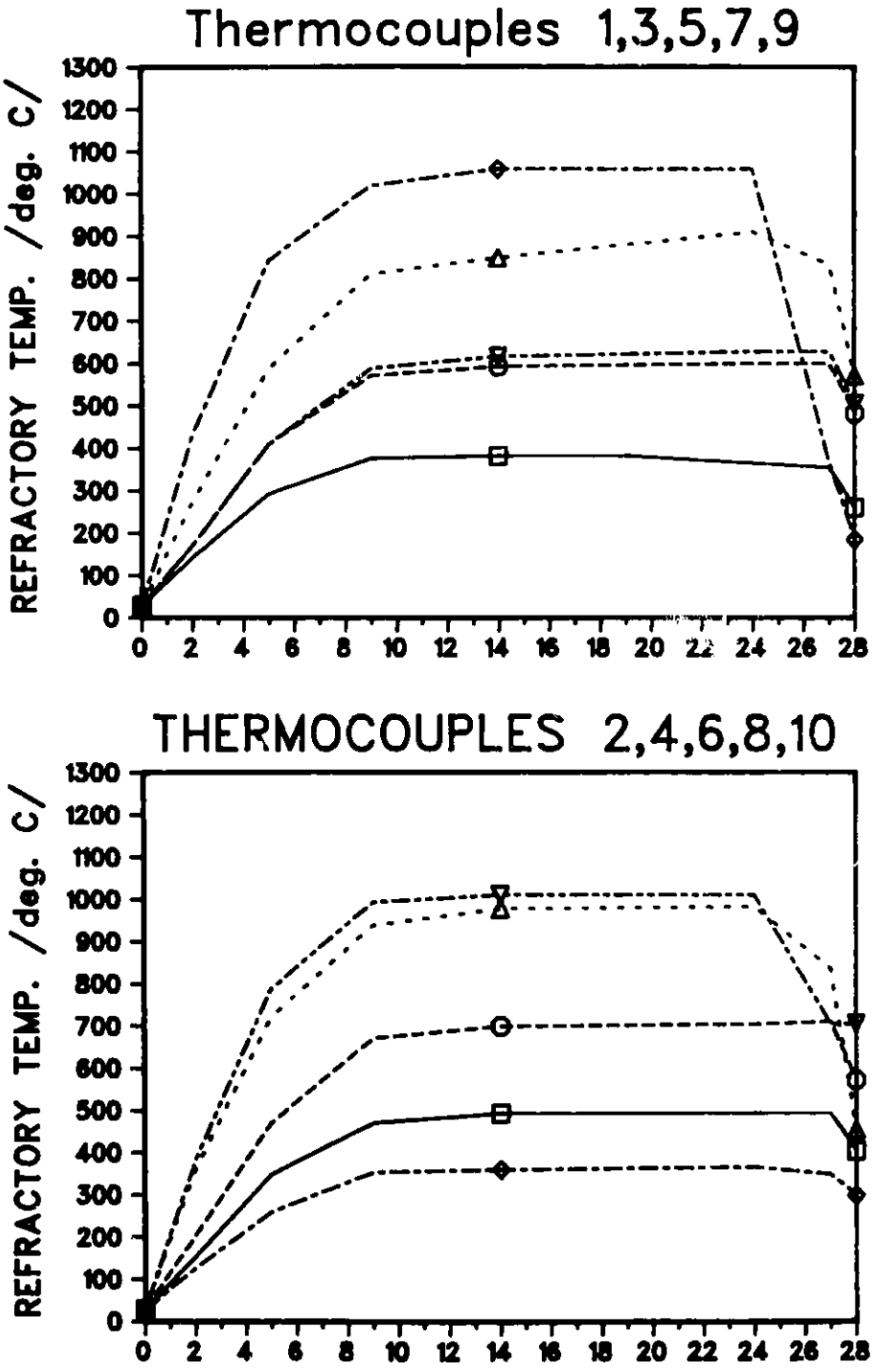


Fig. 15. Temperature-Time Profiles at Thermocouple Positions Indicated in Fig. 14b. ANL Neg. No. 306-79-536.

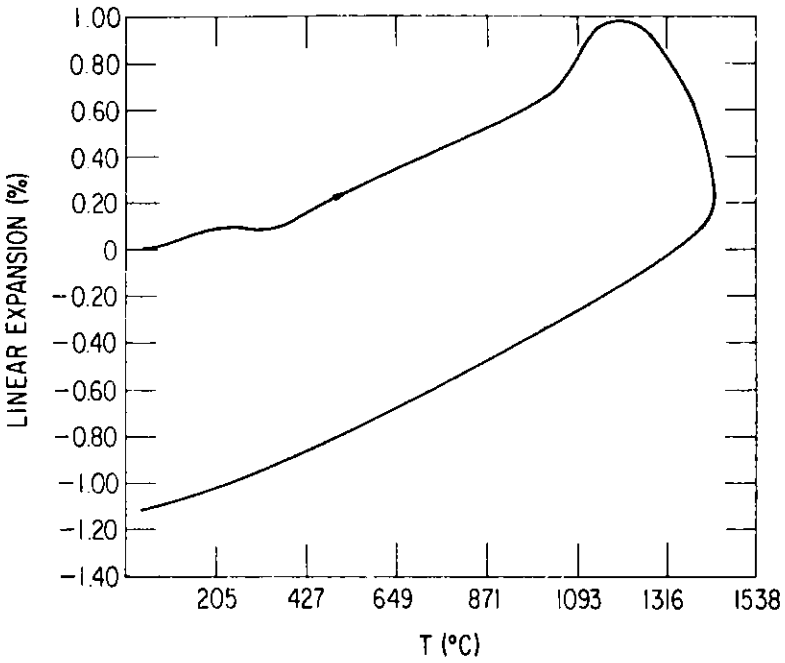


Fig. 16. Thermal Expansion Curve for Castolast G High-alumina Refractory. ANL Neg. No. 306-79-539.

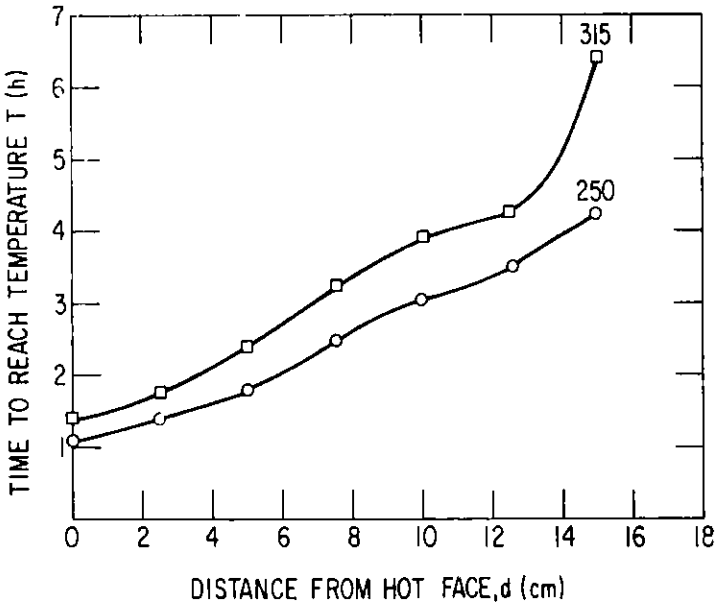


Fig. 17. Time to Reach Critical Shrinkage-reversal Temperatures of 250 and 315°C at a Heating Rate of about 220°C/h. ANL Neg. No. 306-79-538.

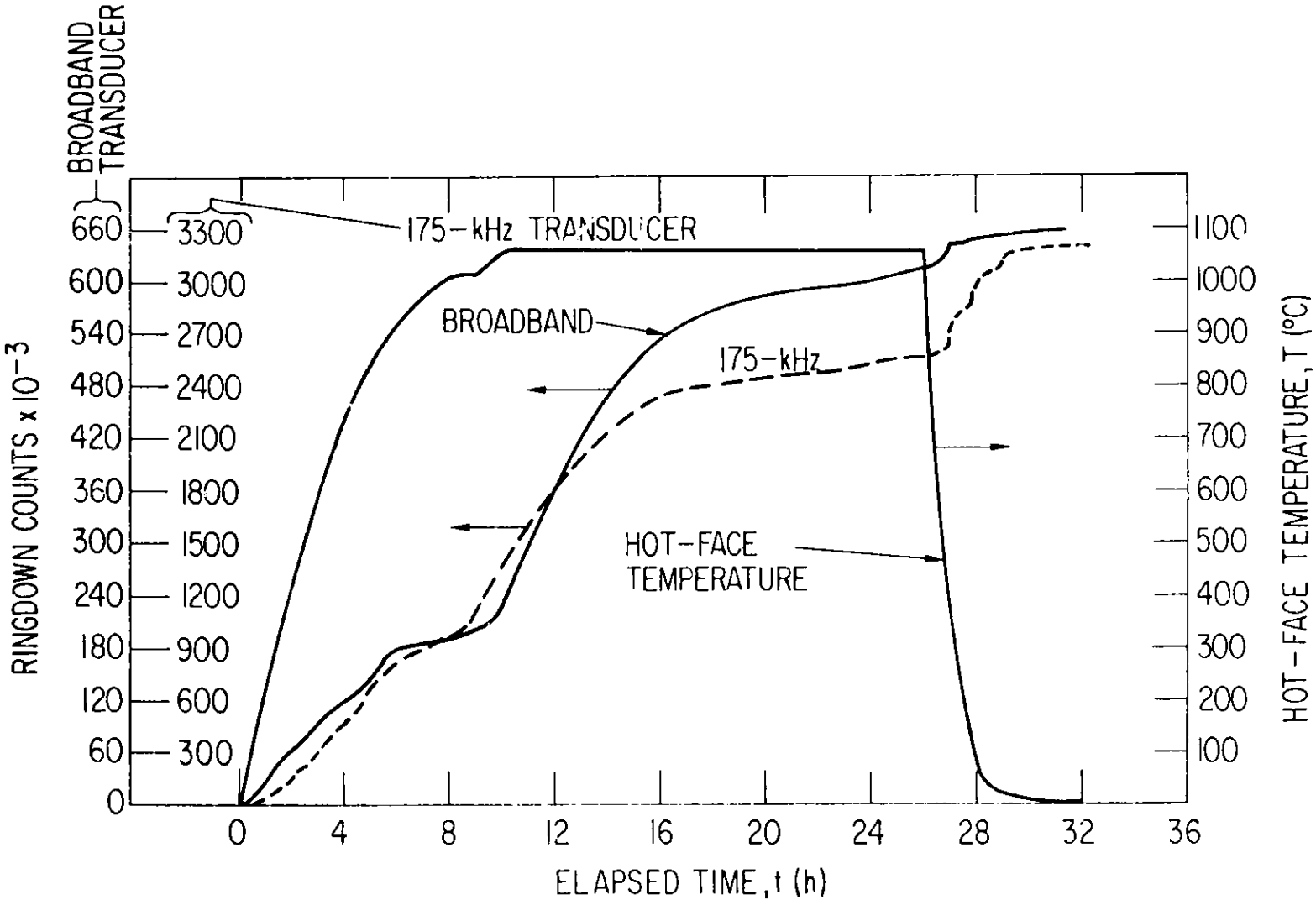


Fig. 18. Ringdown Counts as a Function of Time. Both broadband and 175-kHz resonant transducer outputs are shown. ANL Neg. No. 306-79-533.

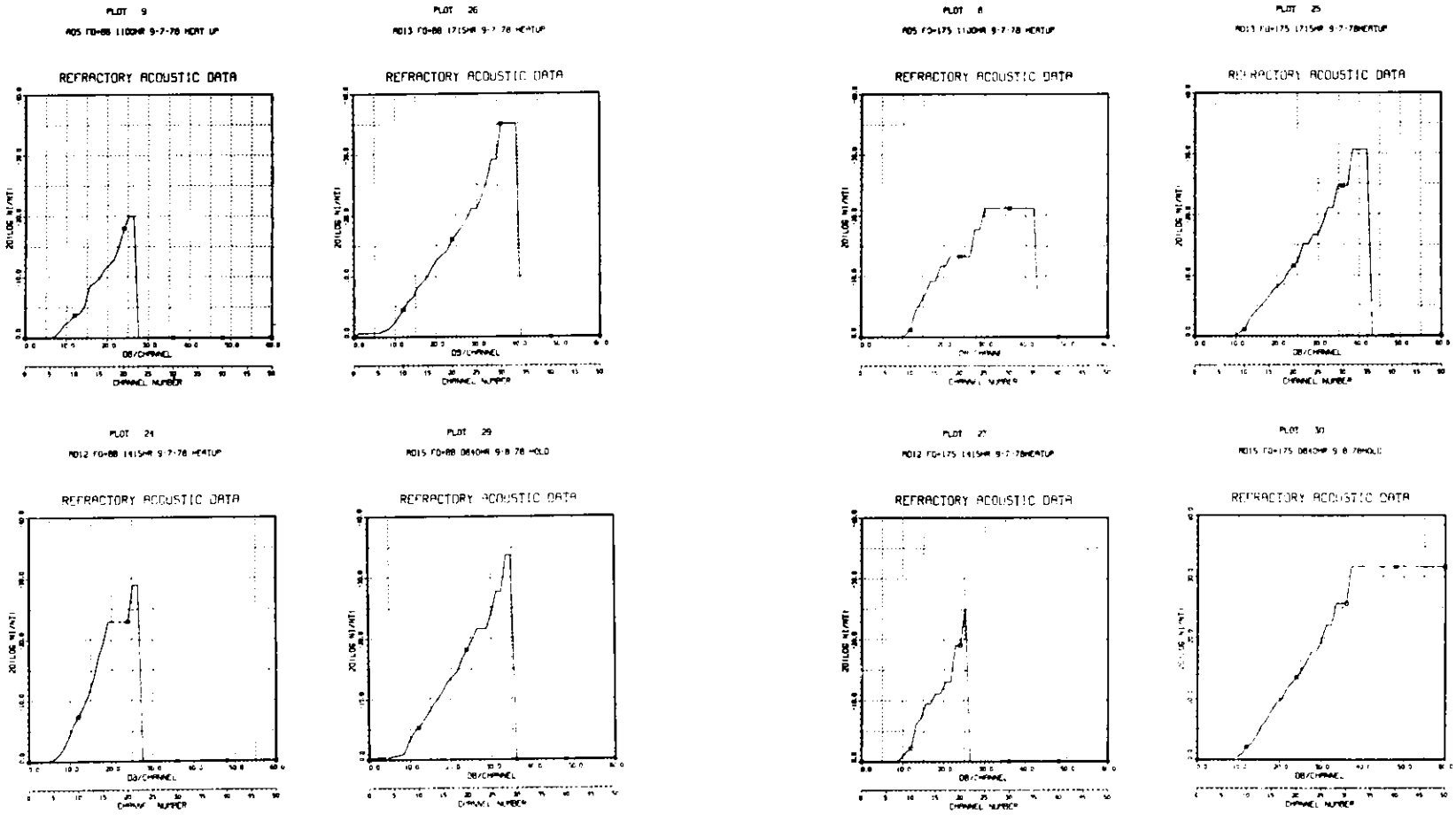


(a) (b)

Fig. 19. Selected Amplitude-distribution Plots for Broadband (a) and Resonant (b) Transducers, Showing the Limited Effect of Bandwidth on Slope. ANL Neg. No. 306-79-530.

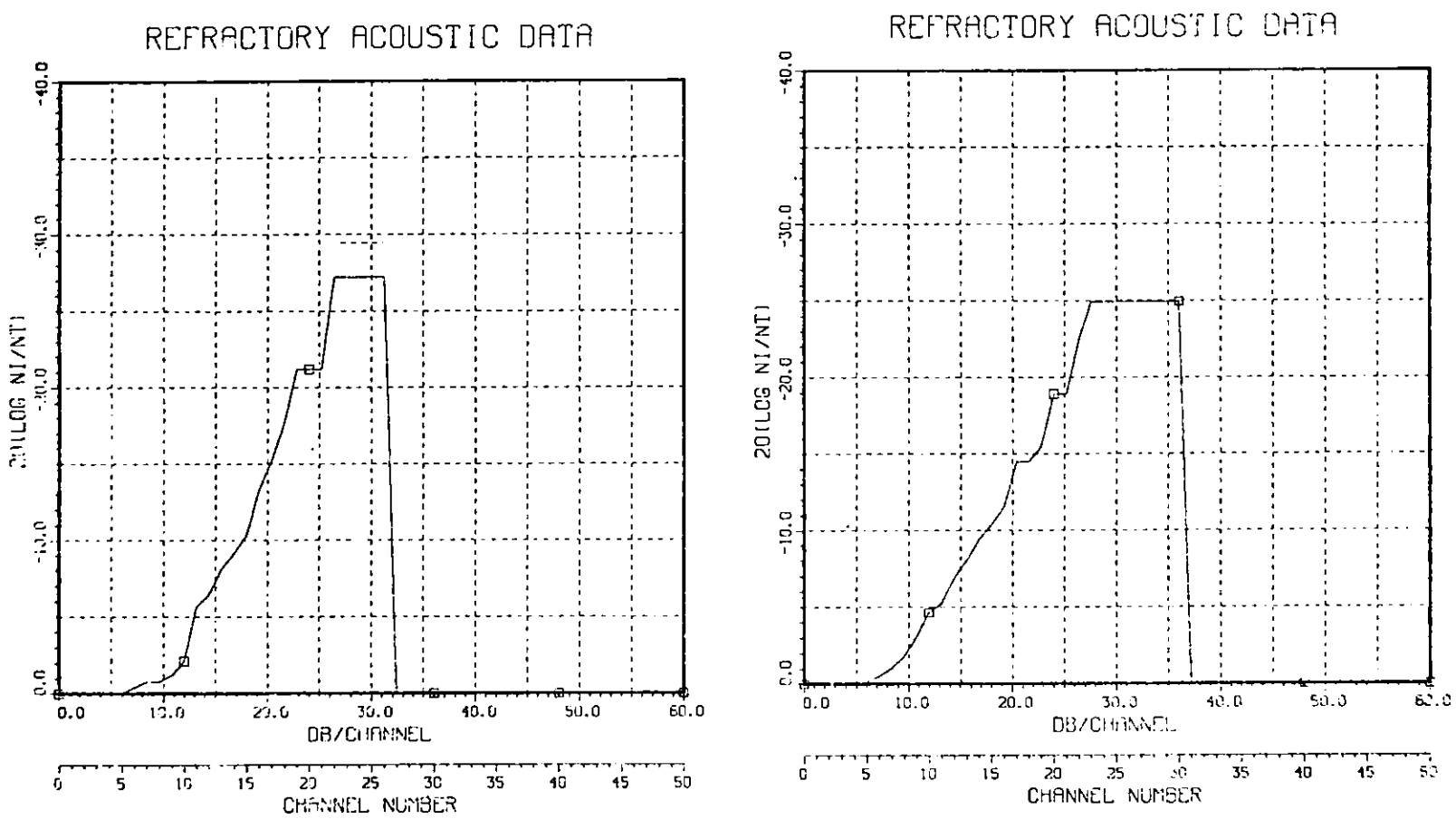


**Fig. 20. Amplitude Distribution for 175-kHz (Left) and Broadband Transducers During Cooling of Thick Panel. ANL Neg. No. 306-79-541.**

3. Component Inspection

a. Acoustic Monitoring of Valves

During this quarter, the noninvasive acoustic leak-detection program has concerned itself with the modification of a coal-slurry loop to extend the gas-leak work to valves for slurries typical of coal-liquefaction processes. The system being modified (see Fig. 21) is capable of providing a driving pressure of 206 kPa (30 psig). Initial tests will be conducted using orifice plates (shown in Fig. 22) with 2.38-mm (3/32-in.), 3.18-mm (1/8-in.), and 6.35-mm (1/4-in.) cylindrical and 6.35- to 3.18-mm and 9.54- to 6.35-mm tapered orifices (the latter two in both converging and diverging positions). Pressure gauges will be located both upstream and downstream of the orifice. Upstream pressures will be varied between 0 and 68.9 kPa (10 psig).

The initial slurry to be tested consists of a 20% coal-water mixture. The instrumentation to be used consists of passive acoustic transducers, Acoustic Emission Technology models AC30L and AC175, with nominal resonance of 30 and 175 kHz, respectively. The decision to work in this frequency range was based on the findings of Dickey et al,[12] who monitored acoustic emissions due to water leakage through cracked and gouged valves. Their data show that an adequate signal-to-noise ratio exists between 8 and 75 kHz, with the largest-amplitude signals centering on 20 kHz. Their data were taken at pressures of 0 to 55.2 kPa (8 psig).

The nature of the system background noise will be determined using a closed orifice plate. Noise signals will be collected at both the orifice plate and random points on the surrounding structure. Signals will initially be monitored by an oscilloscope and a spectrum analyzer. The feasibility of noise subtraction will also be investigated by cross-correlating noise at the orifice plate with noise taken at various points on the structure. If a high correlation can be found, this technique will be integrated into the final instrumentation system.

Once the system noise has been characterized, the 6.35-mm (1/4-in.) orifice plate will be installed and data taken. Data will initially be recorded on film. If deemed advantageous, data can also be recorded on tape and transferred to the computer for more sophisticated data analysis. The desirability of this will be decided after initial data are taken.

The results are expected to show that acoustic emissions in the 10- to 50-kHz range are strongly dependent on upstream pressure. The relationship between acoustic emission and flow rate will be carefully monitored. A high correlation was noted by Dickey et al.[12] between pressure and acoustic emission; however, d(flow rate)/d(acoustic emission amplitude) was practically zero. This will be carefully monitored throughout the operation of our apparatus.

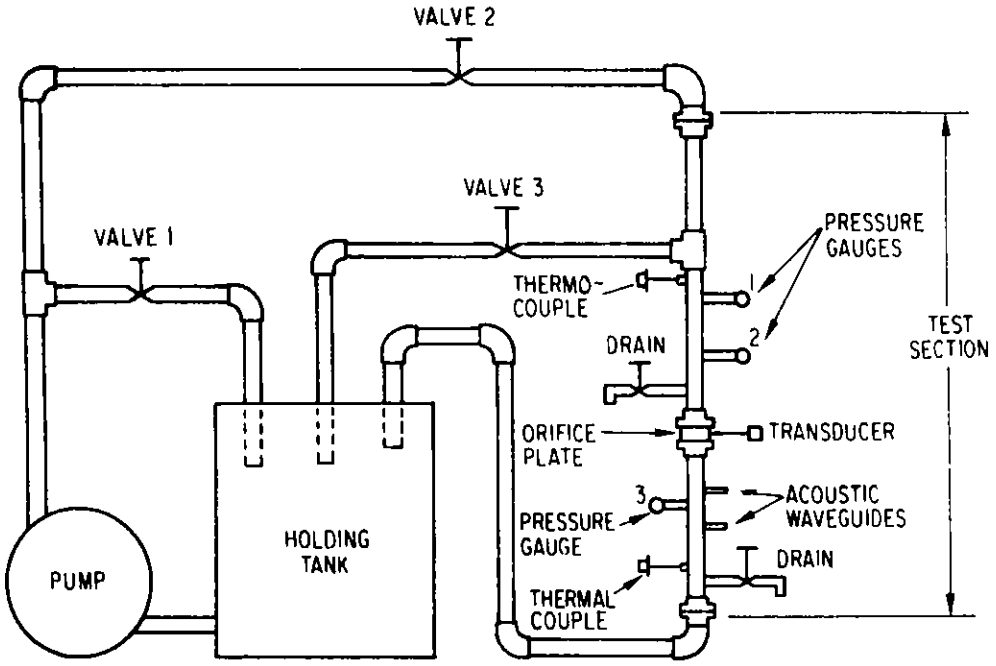


Fig. 21. Diagram of Slurry Loop. Valves 1, 2 and 3 are, respectively, the primary bypass, pressure throttling valve, and secondary bypass. Pressure will range from 0 to 10 psig. ANL Neg. No. 306-79-617.

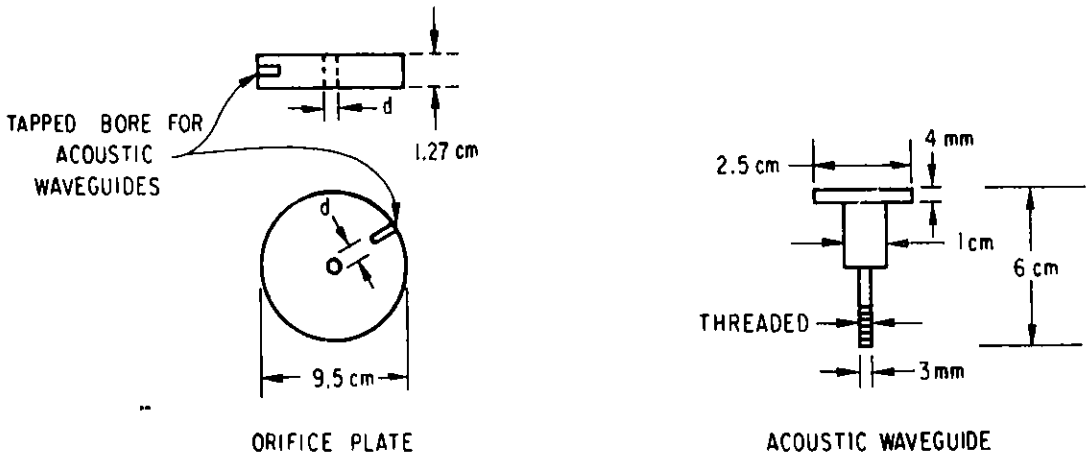


Fig. 22. Diagram of Orifice Plate and Acoustic Waveguide to be Installed in Test Section of Slurry Loop. ANL Neg. No. 306-79-617.

Task D -- Corrosion Behavior of Materials in Coal-conversion Processes

1. Corrosion in Gasification Environments *(K. Natesan)*

The objectives of this program are to (1) develop uniaxial tensile data on four commercial alloys exposed to multicomponent gas environments, (2) experimentally evaluate the high-temperature corrosion behavior of iron- and nickel-base alloys in gas environments with a wide range of oxygen, sulfur, and carbon potentials, and (3) develop a systems approach, based upon available thermodynamic and kinetic information, to evaluate possible corrosion problems in various coal-conversion processes.

The experimental program to generate uniaxial tensile data on four iron- and nickel-base alloys exposed to multicomponent gas environments was discussed previously.[13] The experimental apparatus and the chemical composition of the alloys and gas mixtures used in this program were described in detail.[10] Calculated values for the oxygen and sulfur partial pressures established by the gas mixtures in different runs have also been reported.[9]

During the present quarter, 3.6-Ms (1000-h) exposures of corrosion and uniaxial tensile specimens to gas mixtures 2B and 3B at 750°C, 3B at 871°C, and 3A at 982°C were completed. Postexposure tensile tests of the specimens are being conducted in vacuum at an initial strain rate of $4.1 \times 10^{-4}$ $s^{-1}$.

The corrosion specimens from different experiments were examined by scanning-electron microscopy with an energy-dispersive x-ray analyzer or an electron microprobe. Figures 23-26 show SEM photographs of the cross sections of Incoloy 800, Type 310 stainless steel, Inconel 671, and U. S. Steel Alloy 18-18-2, respectively, after a 3.6-Ms exposure to a complex gas mixture (run FO2B750). Also shown in these figures are the metallic element (chromium, iron, and nickel) and sulfur distributions in the scale/alloy interface regions of the samples. Figures 27-30 show electron-probe photographs of the specimens after a 3.6-Ms exposure to gas mixture 3B at 750°C (run DO3B750). In both these runs, the alloys developed Cr or (Cr,Fe) sulfide scales upon exposure to the gas mixtures. Equilibrium calculations indicate that gas mixtures 2B and 3B should result in almost the same oxygen and sulfur partial pressures and a carbon activity of unity in the environment at 750°C. But these gas mixtures will establish significantly different activities for oxygen, sulfur, and carbon at 871 and 982°C, the temperatures selected for other experiments. The type and thickness of scale layers and depths of intergranular penetration of the base materials from various experiments are listed in Table VIII.

Figures 31-34 and 35-38 show cross sections of specimens exposed to the 3B mixture at 871°C (run FO3B871) and to the 3A mixture at 982°C. The specimens exposed at 871°C developed sulfide scales, the type and thickness of which are given in Table VIII. Of the alloys exposed at 982°C, Incoloy 800 developed a (Cr,Fe) sulfide outer layer and an inner layer of Cr-rich oxide. The thickness of the scale was ∿533 μm and the depth of intergranular penetration was ∿367 μm. On the other hand, Type 310 stainless steel, Inconel 671,

and U. S. Steel Alloy 18-18-2 developed a thinner Cr-rich oxide scale with significant penetration of sulfur into the base metal. Mechanical testing of the specimens from these experiments is in progress.

Additional experiments are under way to evaluate the effect of variations in the exposure environment on the uniaxial tensile behavior of the selected alloys.

TABLE VIII. Information on Corrosion-Product Layers for Spec[illegible] After 3.6-Ms Exposures to Complex Gas Mixtures from Different Experimental Runs

| Run No. | $P_{O_2}$, atm | $P_{S_2}$, atm | $a_c$ | Alloy | Scale Thickness, μm | Depth of Penetration, μm | Type of Scale |
|---|---|---|---|---|---|---|---|
| **Temperature 750°C** | | | | | | | |
| FO2B750 | $1.9 \times 10^{-22}$ | $9.7 \times 10^{-9}$ | 1.0 | Incoloy 800 | 130 | 140 | (Cr,Fe) Sulfide |
| | | | | Type 310 SS | 35 | 147 | (Cr,Fe) Sulfide |
| | | | | Inconel 671 | 133 | 71 | Cr Sulfide |
| | | | | U.S. Steel Alloy 18-18-2 | 180 | 43 | Fe Sulfide |
| DO3B750 | $1.9 \times 10^{-22}$ | $1.1 \times 10^{-8}$ | 1.0 | Incoloy 800 | 118 | 150 | (Fe,Cr Sulfide)/Cr Oxide |
| | | | | Type 310 SS | 95 | 158 | Cr-Fe-Ni Sulfide |
| | | | | Inconel 671 | 116 | 126 | Cr-Ni Sulfide |
| | | | | U.S. Steel Alloy 18-18-2 | 125 | 32 | Fe Sulfide/Cr Oxide |
| **Temperature 871°C** | | | | | | | |
| DO3B871 | $4.9 \times 10^{-21}$ | $8.6 \times 10^{-8}$ | 1.0 | Incoloy 800 | 40 | 107 | Cr Sulfide |
| | | | | Type 310 SS | 133 | 80 | (Cr,Fe) Sulfide |
| | | | | Inconel 671 | 9 | 11 | Cr Sulfide |
| | | | | U.S. Steel Alloy 1°-18-2 | 67 | 133 | Cr Sulfide |
| **Temperature 982°C** | | | | | | | |
| BO3A982 | $1.8 \times 10^{-16}$ | $1.6 \times 10^{-6}$ | 0.014 | Incoloy 800 | 533 | 367 | (Cr,Fe) Sulfide/Cr Oxide |
| | | | | Type 310 SS | 21 | 253 | Cr Oxide |
| | | | | Inconel 671 | 78 | 267 | Cr Oxide |
| | | | | U.S. Steel Alloy 18-18-2 | 20 | 347 | Cr Oxide |

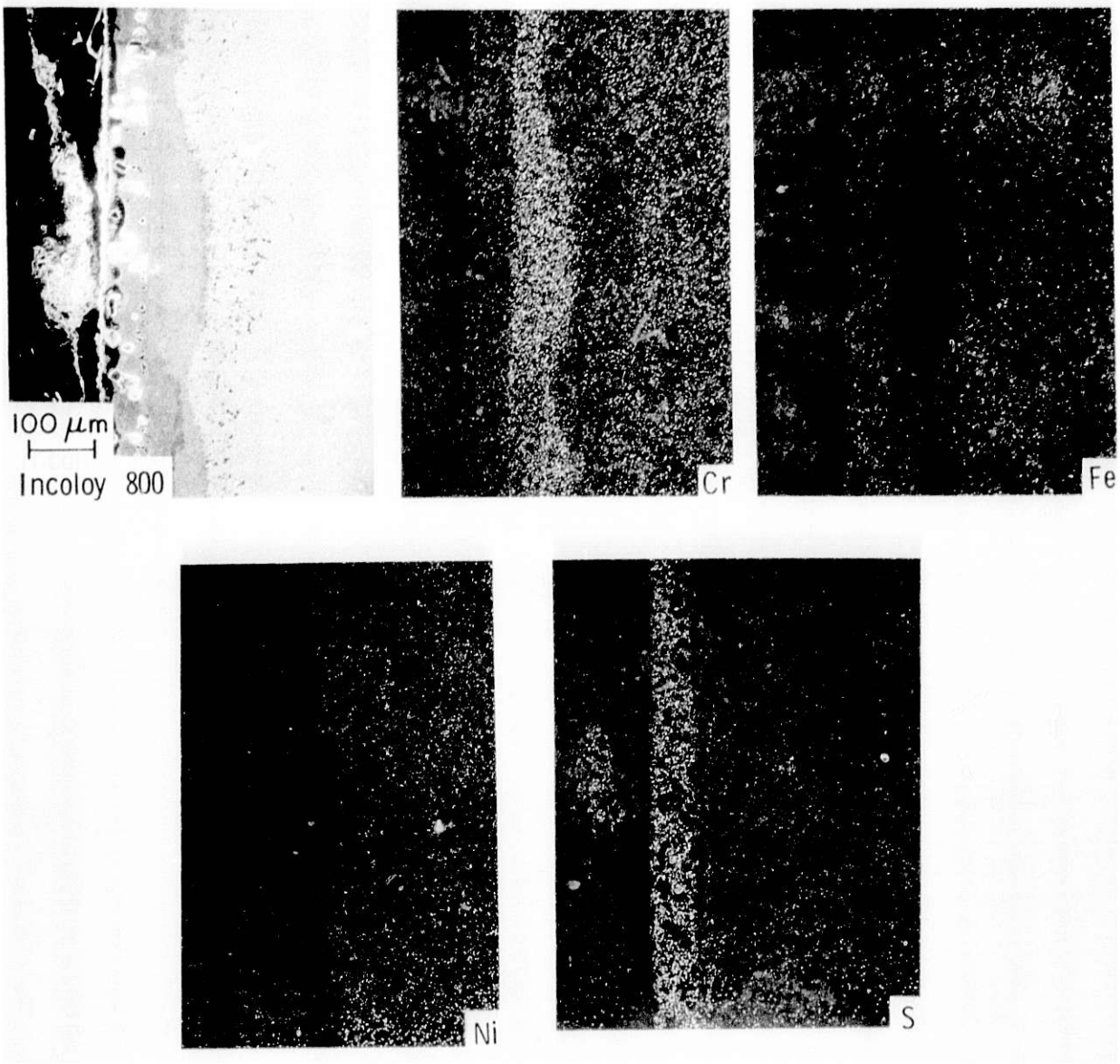


Fig. 23. X-ray Photograph and Cr, Fe, Ni, and S Distribution in Incoloy 800 Specimen After a 3.6-Ms Exposure to a Complex Gas Mixture at 750°C (Run FO2B750). In the distribution pictures, light regions indicate a high concentration of the respective elements.
ANL Neg. No. 306-79-329.

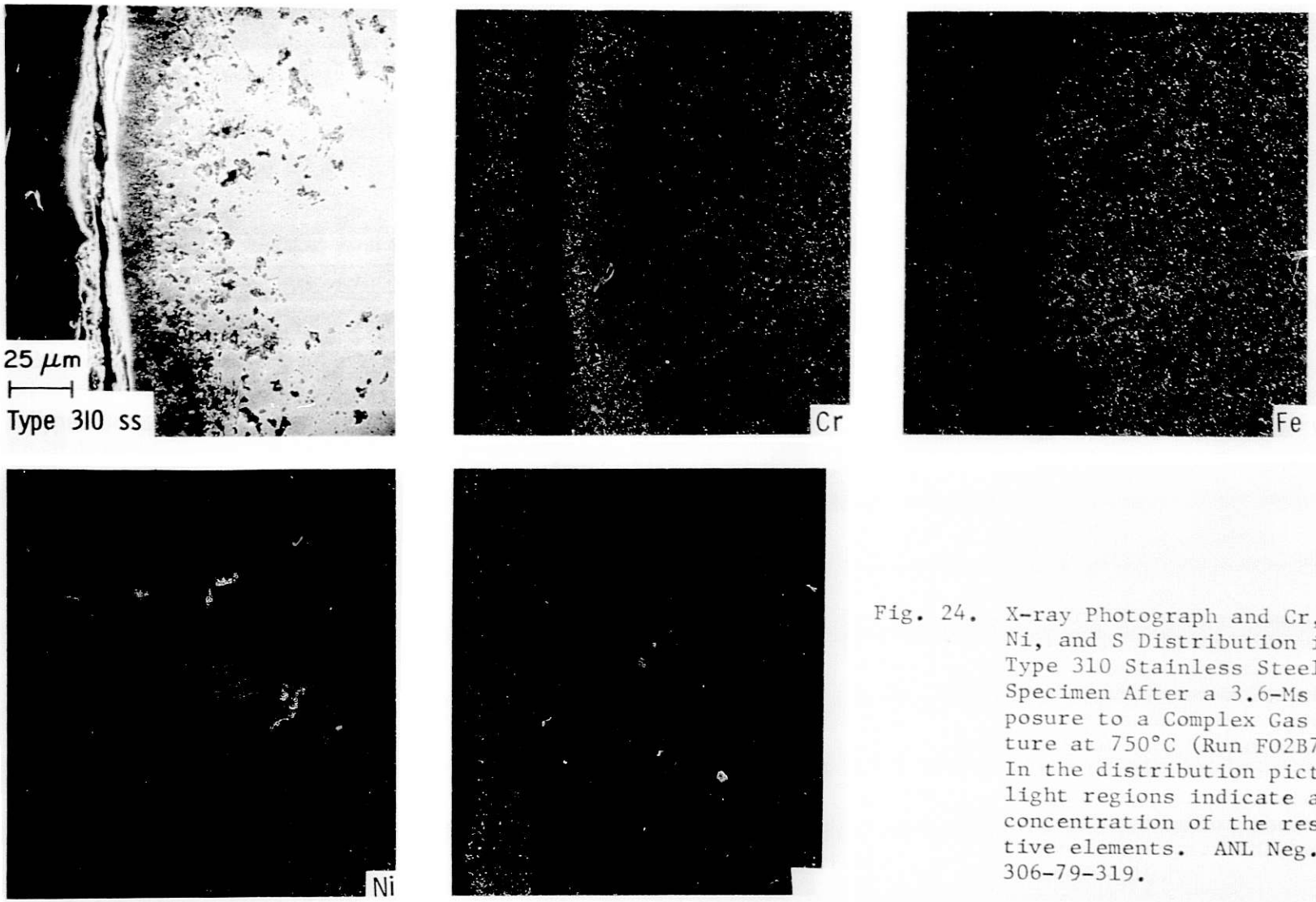


Fig. 24. X-ray Photograph and Cr, Fe, Ni, and S Distribution in Type 310 Stainless Steel Specimen After a 3.6-Ms Exposure to a Complex Gas Mixture at 750°C (Run FO2B750). In the distribution pictures, light regions indicate a high concentration of the respective elements. ANL Neg. No. 306-79-319.

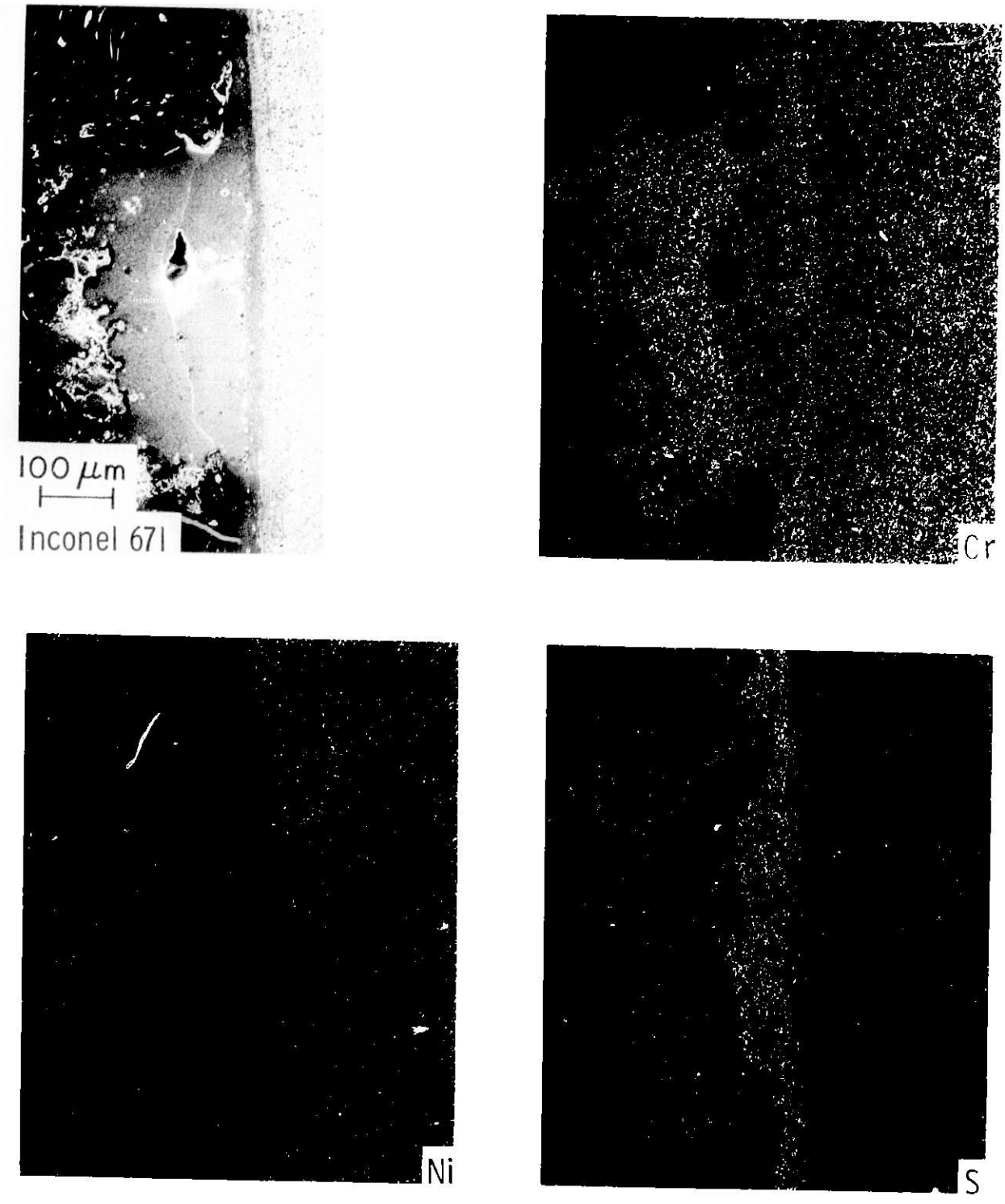


Fig. 25. X-ray Photograph and Cr, Ni, and S Distribution in Inconel 671 Specimen After a 3.6-Ms Exposure to a Complex Gas Mixture at 750°C (Run FO2B750). In the distribution pictures, light regions indicate a high concentration of the respective elements. ANL Neg. No. 306-79-330.

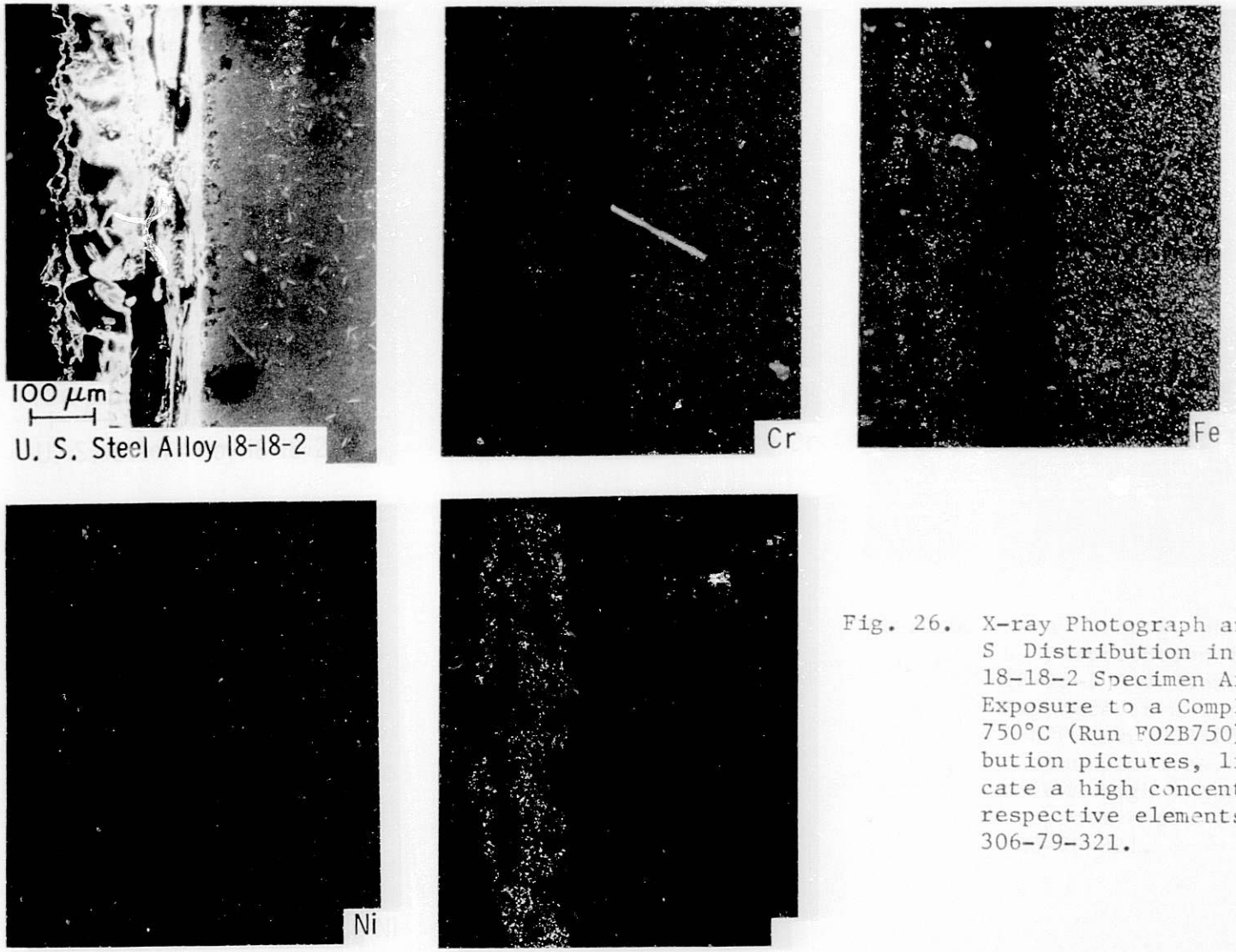


Fig. 26. X-ray Photograph and Cr, Fe, Ni, and S Distribution in U.S. Steel Alloy 18-18-2 Specimen After a 3.6-Ms Exposure to a Complex Gas Mixture at 750°C (Run FO2B750). In the distribution pictures, light regions indicate a high concentration of the respective elements. ANL Neg. No. 306-79-321.

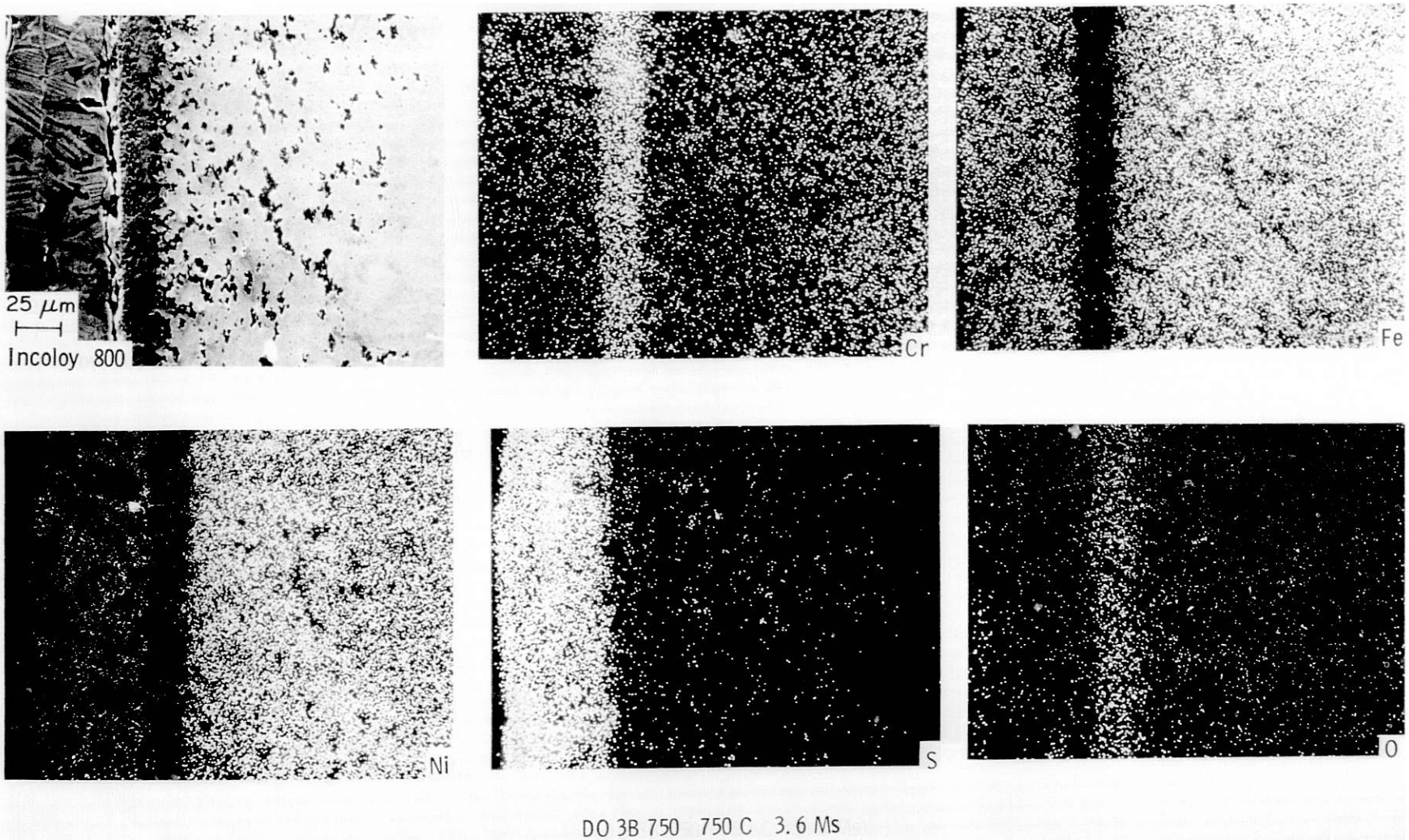


Fig. 27. X-ray Photograph and Cr, Fe, Ni, S, and O Distribution in Incoloy 800 Specimen After a 3.6-Ms Exposure to a Complex Gas Mixture at 750°C (Run DO3B750). In the distribution pictures, light regions indicate a high concentration of the respective elements. ANL Neg. No. 306-79-315.

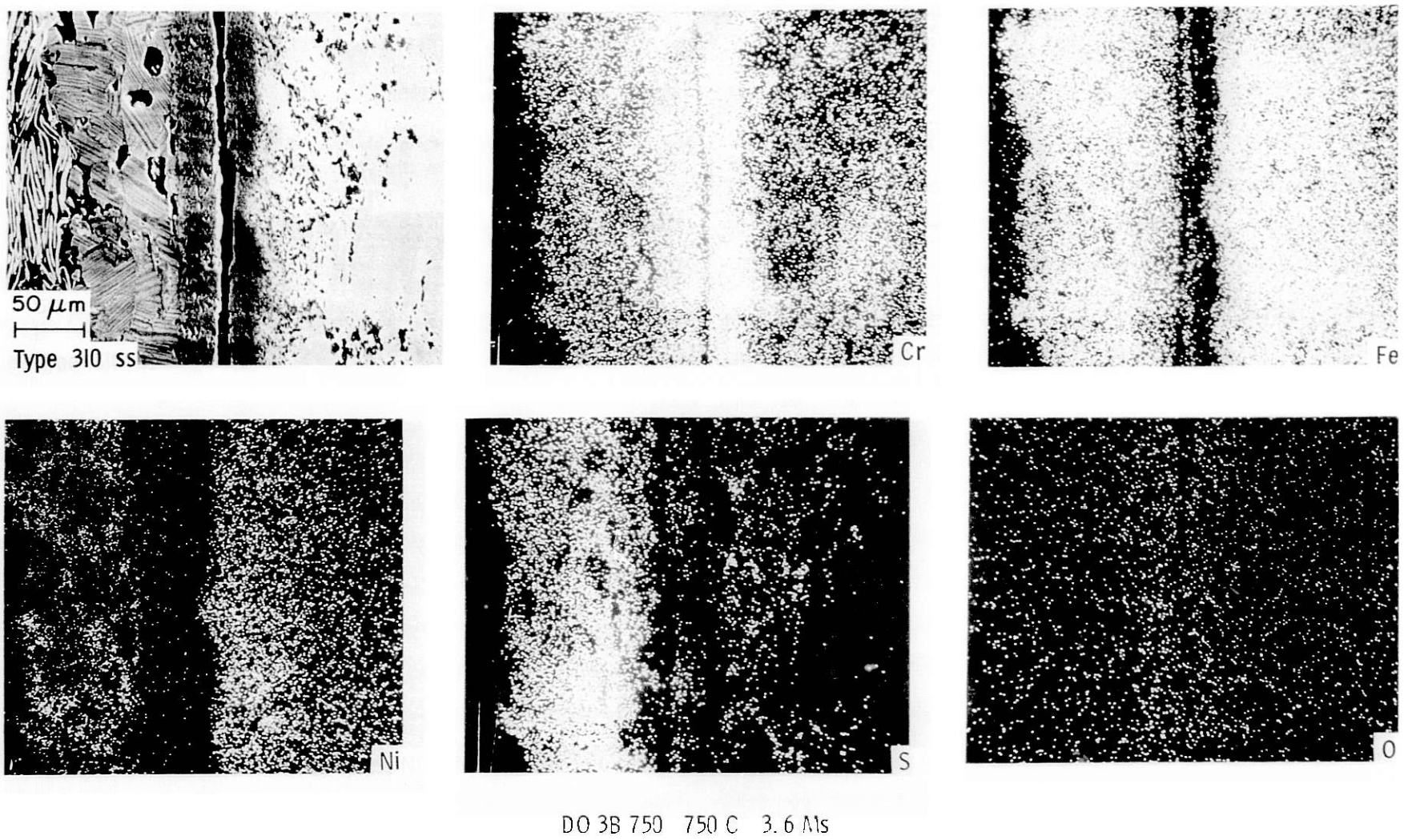


Fig. 28. X-ray Photograph and Cr, Fe, Ni, S, and O Distribution in Type 310 Stainless Steel Specimen After a 3.6-Ms Exposure to a Complex Gas Mixture at 750°C (Run DO3B750). In the distribution pictures, light regions indicate a high concentration of the respective elements. ANL Neg. No. 306-79-316.

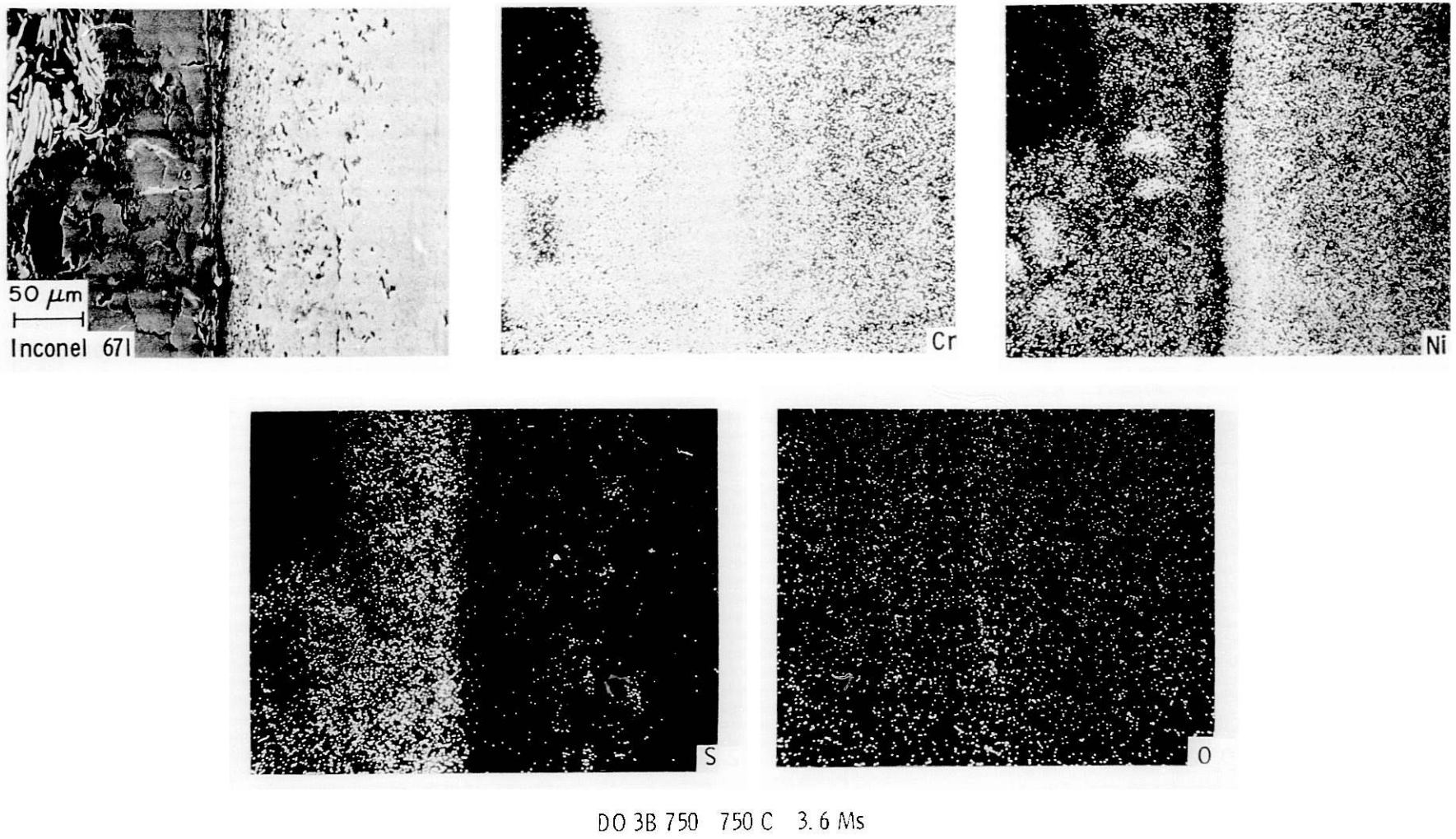


Fig. 29. X-ray Photograph and Cr, Ni, S, and O Distribution in Inconel 671 Specimen After a 3.6-Ms Exposure to a Complex Gas Mixture at 750°C (Run DO3B750). In the distribution pictures, light regions indicate a high concentration of the respective elements. ANL Neg. No. 306-79-328.

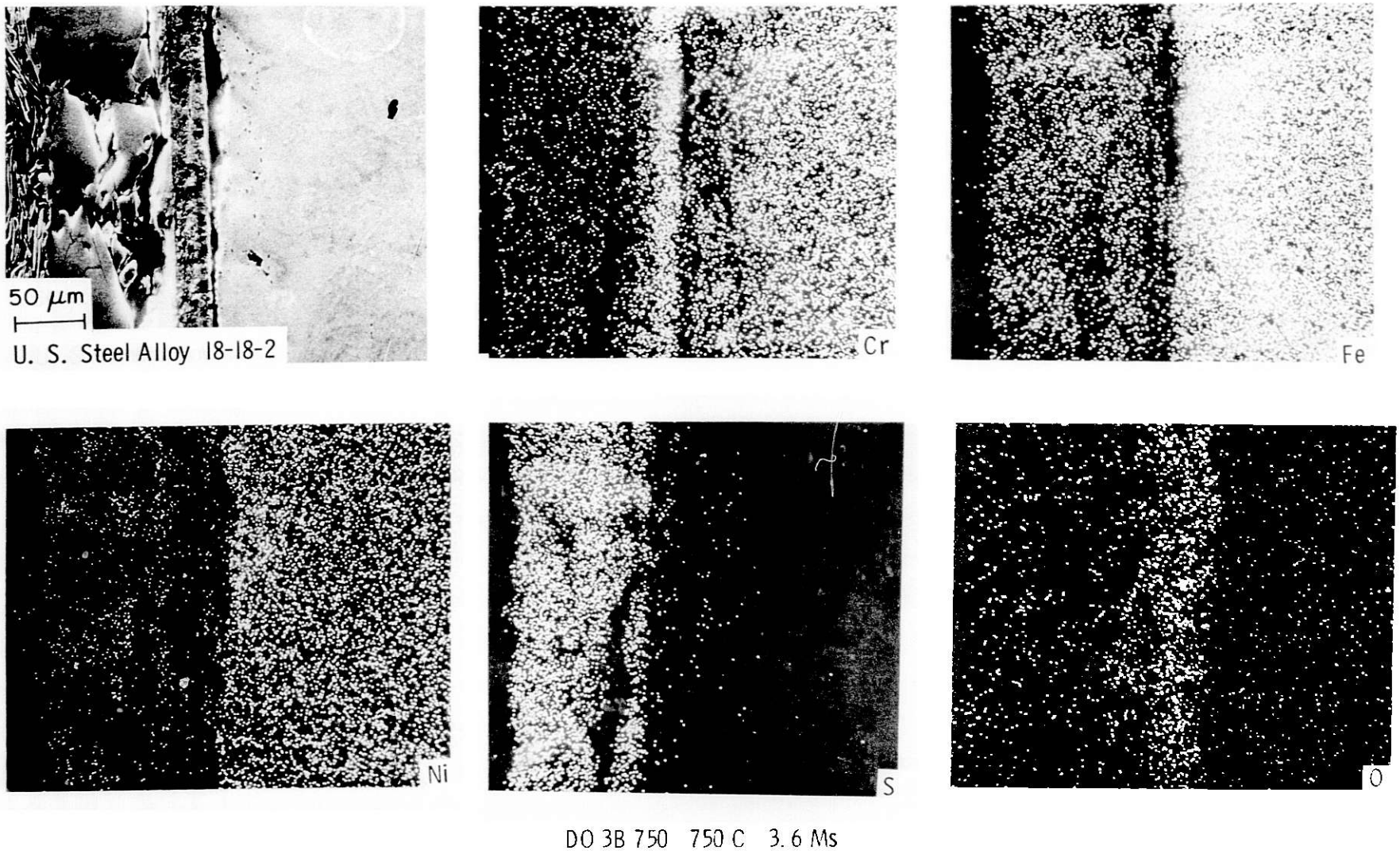


Fig. 30. X-ray Photograph and Cr, Fe, Ni, S, and O Distribution in U.S. Steel Alloy 18-18-2 Specimen After a 3.6-Ms Exposure to a Complex Gas Mixture at 750°C (Run DO3B750). In the distribution pictures, light regions indicate a high concentration of the respective elements. ANL Neg. No. 306-79-317.

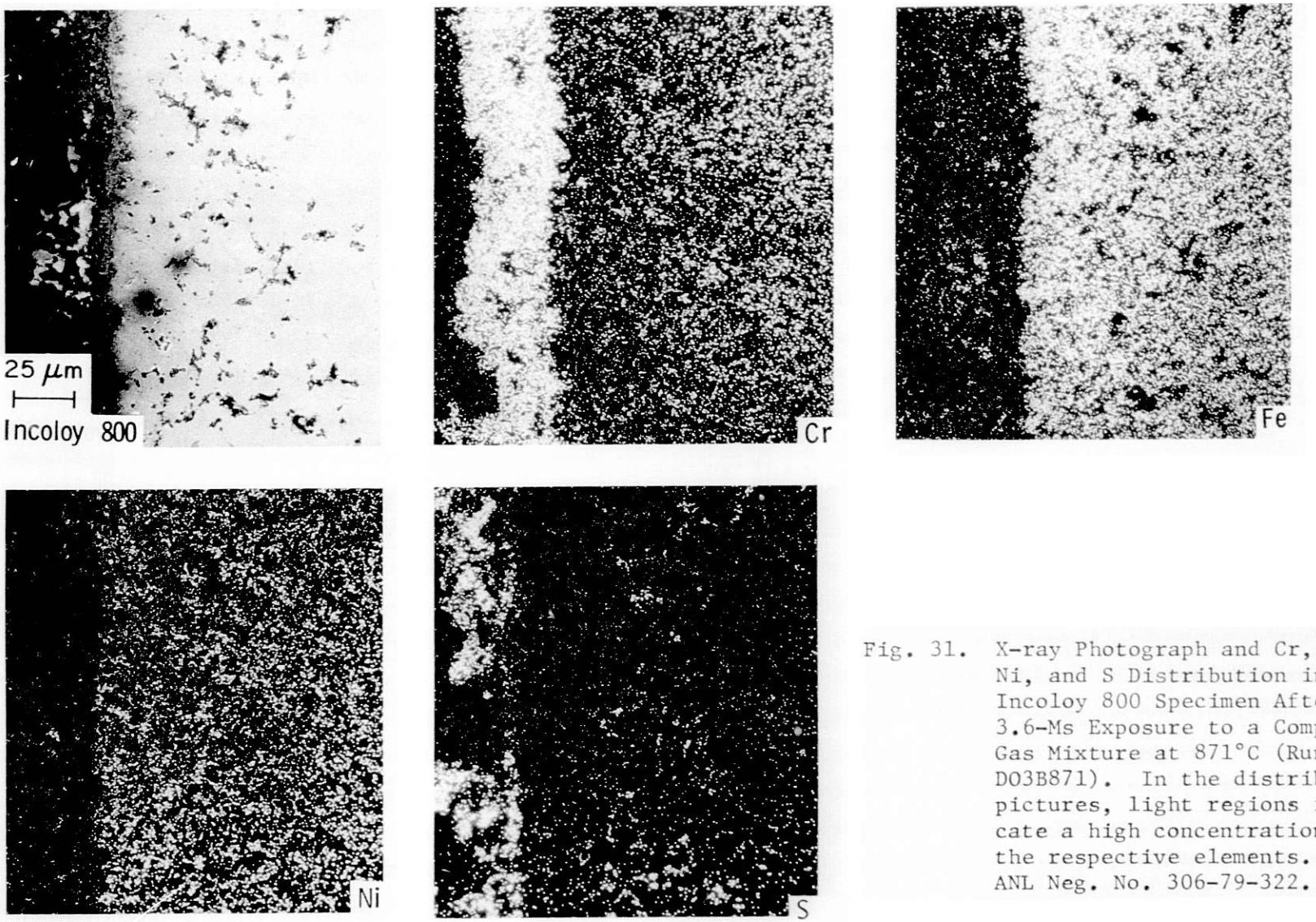


Fig. 31. X-ray Photograph and Cr, Fe, Ni, and S Distribution in Incoloy 800 Specimen After a 3.6-Ms Exposure to a Complex Gas Mixture at 871°C (Run DO3B871). In the distribution pictures, light regions indicate a high concentration of the respective elements. ANL Neg. No. 306-79-322.

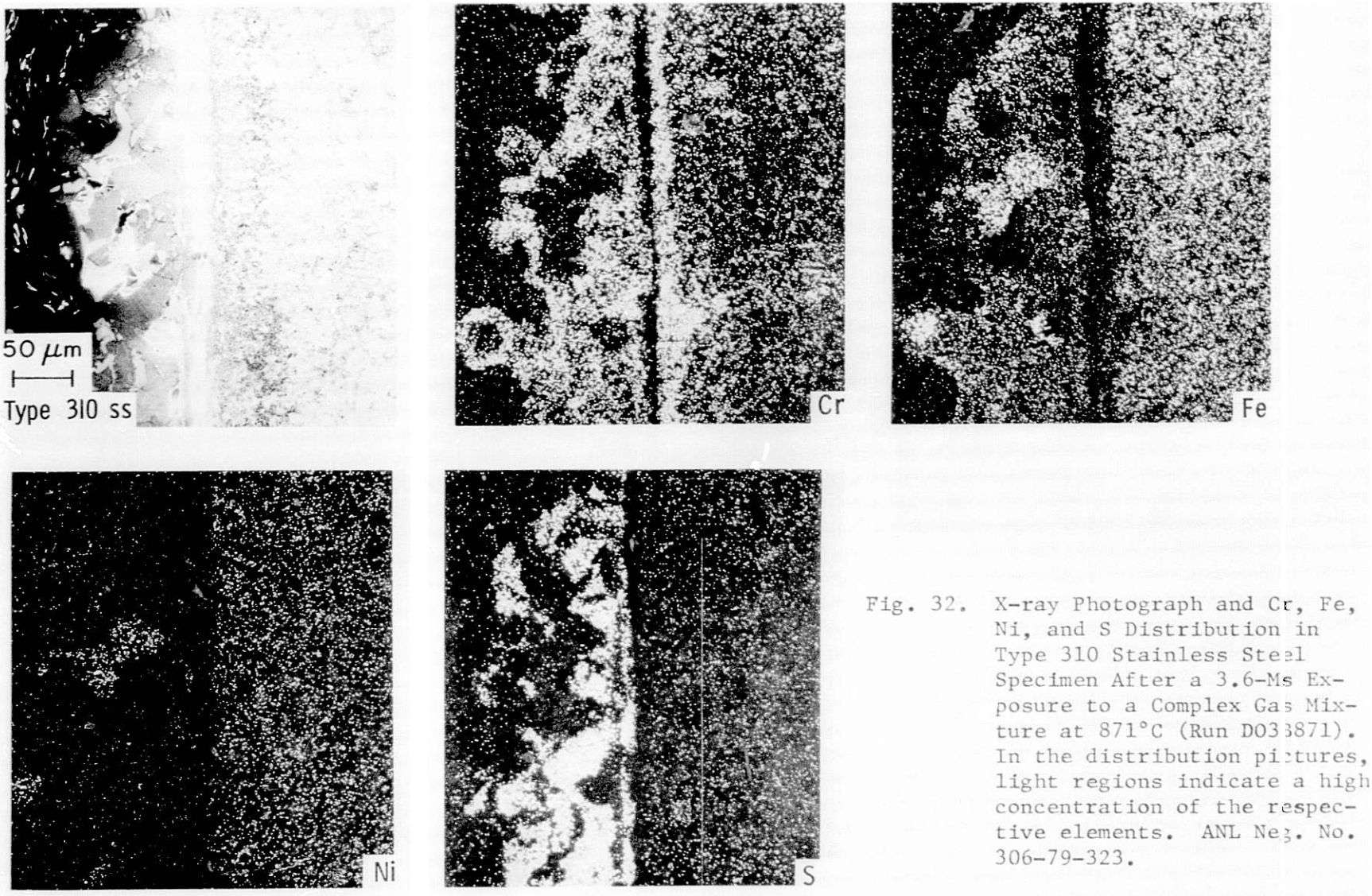


Fig. 32. X-ray Photograph and Cr, Fe, Ni, and S Distribution in Type 310 Stainless Steel Specimen After a 3.6-Ms Exposure to a Complex Gas Mixture at 871°C (Run DO3B871). In the distribution pictures, light regions indicate a high concentration of the respective elements. ANL Neg. No. 306-79-323.

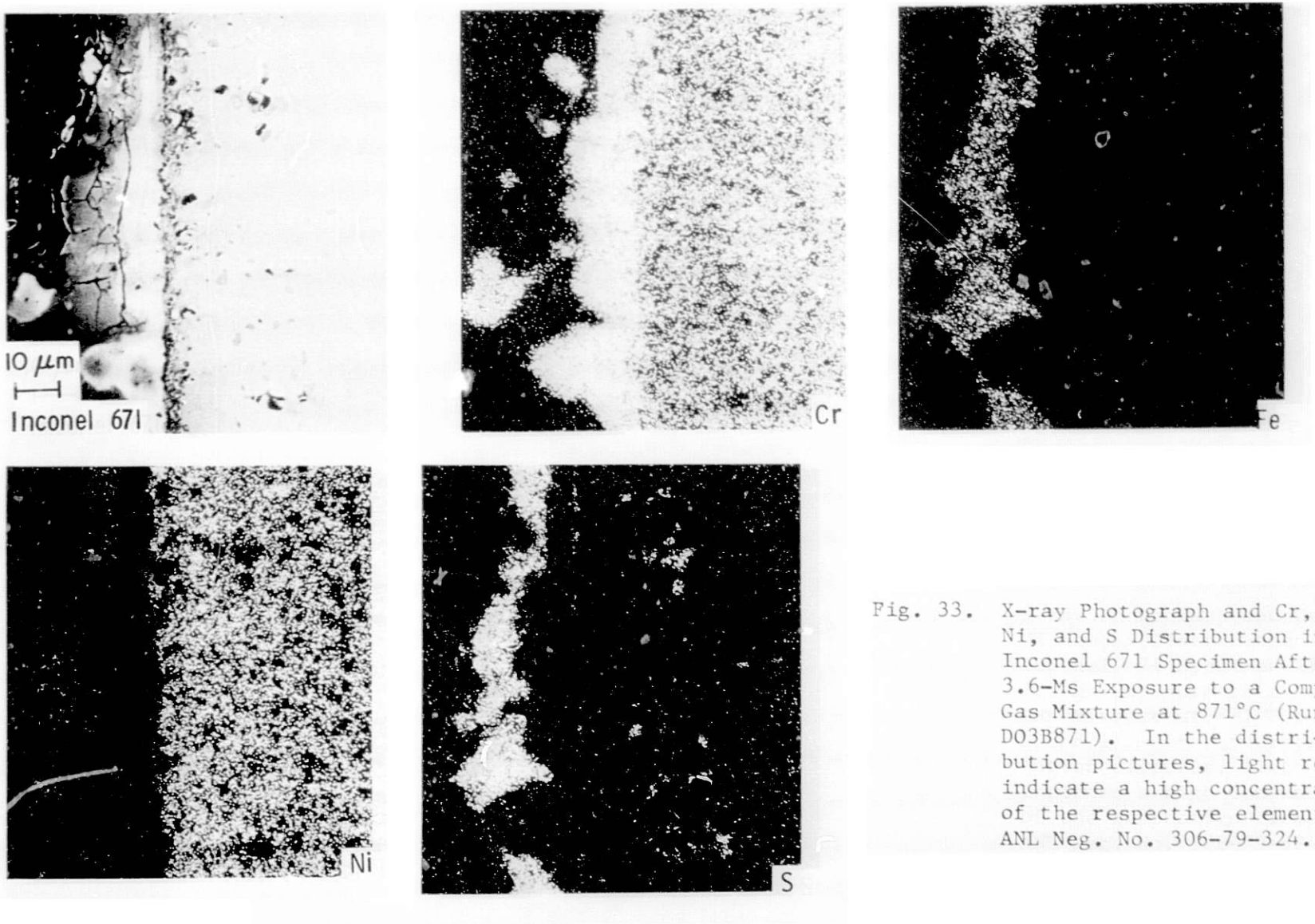


Fig. 33. X-ray Photograph and Cr, Fe, Ni, and S Distribution in Inconel 671 Specimen After a 3.6-Ms Exposure to a Complex Gas Mixture at 871°C (Run DO3B871). In the distribution pictures, light regions indicate a high concentration of the respective elements. ANL Neg. No. 306-79-324.


Fig. 34. X-ray Photograph and Cr, Fe, Ni, Si, and S Distribution in U.S. Steel Alloy 18-18-2 Specimen After a 3.6-Ms Exposure to a Complex Gas Mixture at 871°C (Run D03B871). In the distribution pictures, light regions indicate a high concentration of the respective elements. ANL Neg. No. 306-79-325.

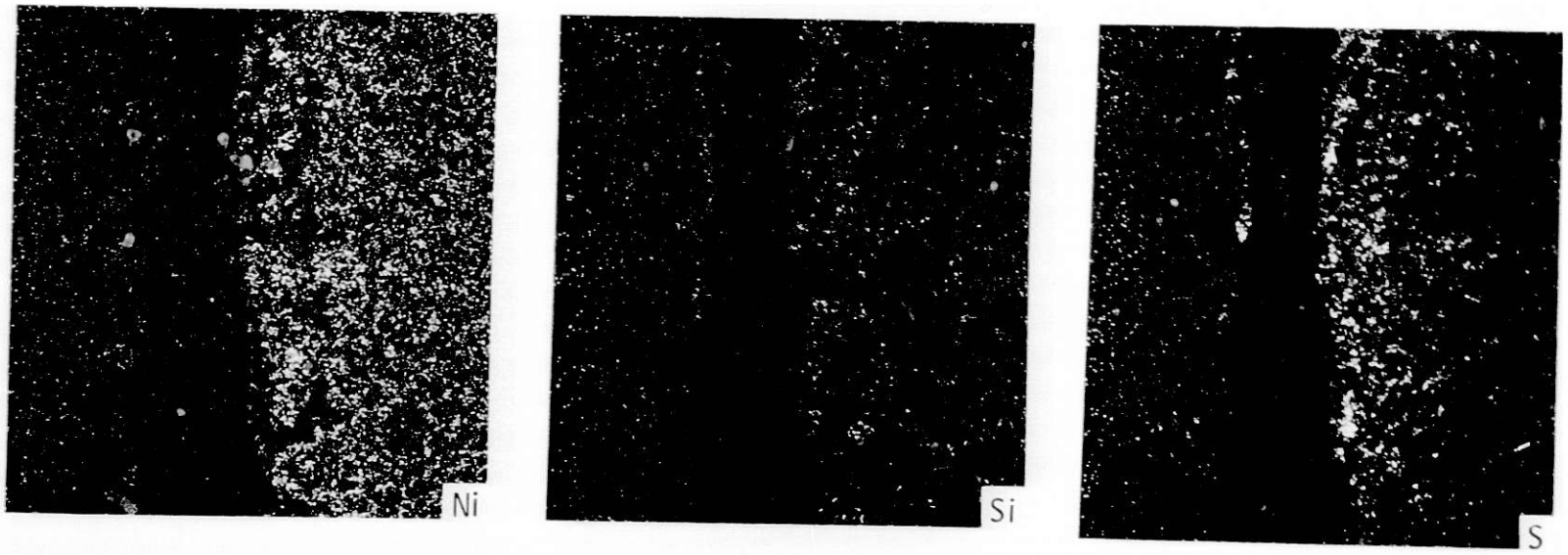


DO 3B 871 871 C 3.6 Ms

Fig. 34
(contd.)

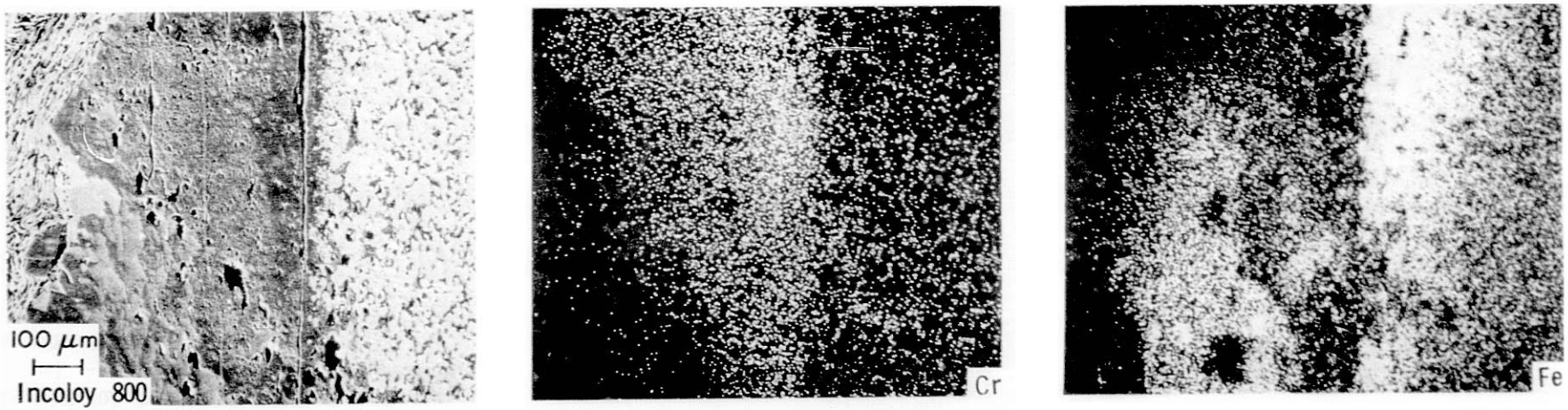


Fig. 35. X-ray Photograph and Cr, Fe, Ni, S, and O Distribution in Incoloy 800 Specimen After a 3.6-Ms Exposure to a Complex Gas Mixture at 982°C (Run BO3A982). In the distribution pictures, light regions indicate a high concentration of the respective elements. ANL Neg. No. 306-79-327.

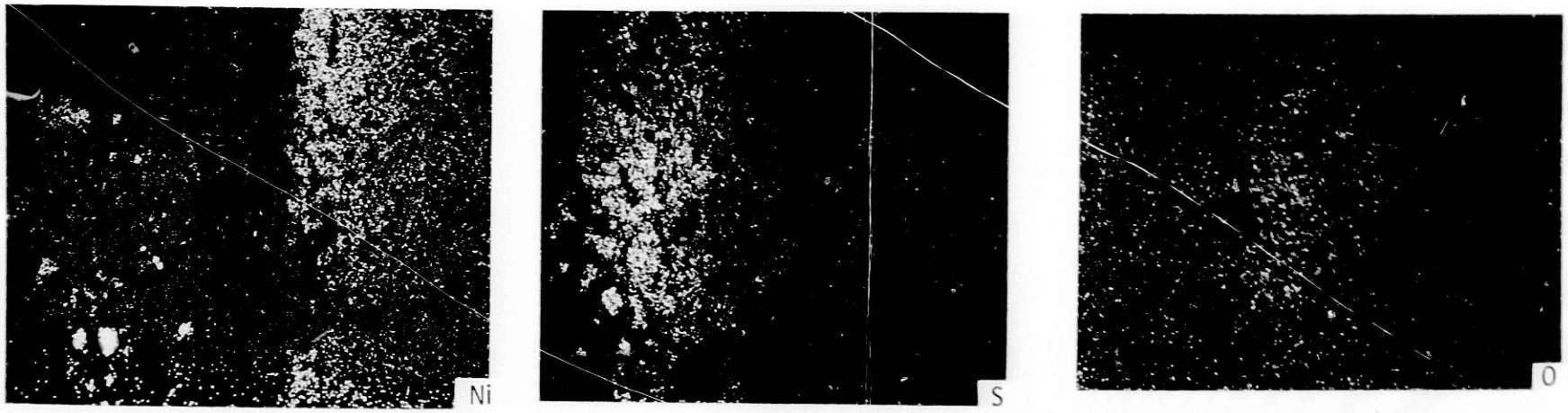


BO 3A 982 982 C 3.6 Ms

Fig. 35
(contd.)

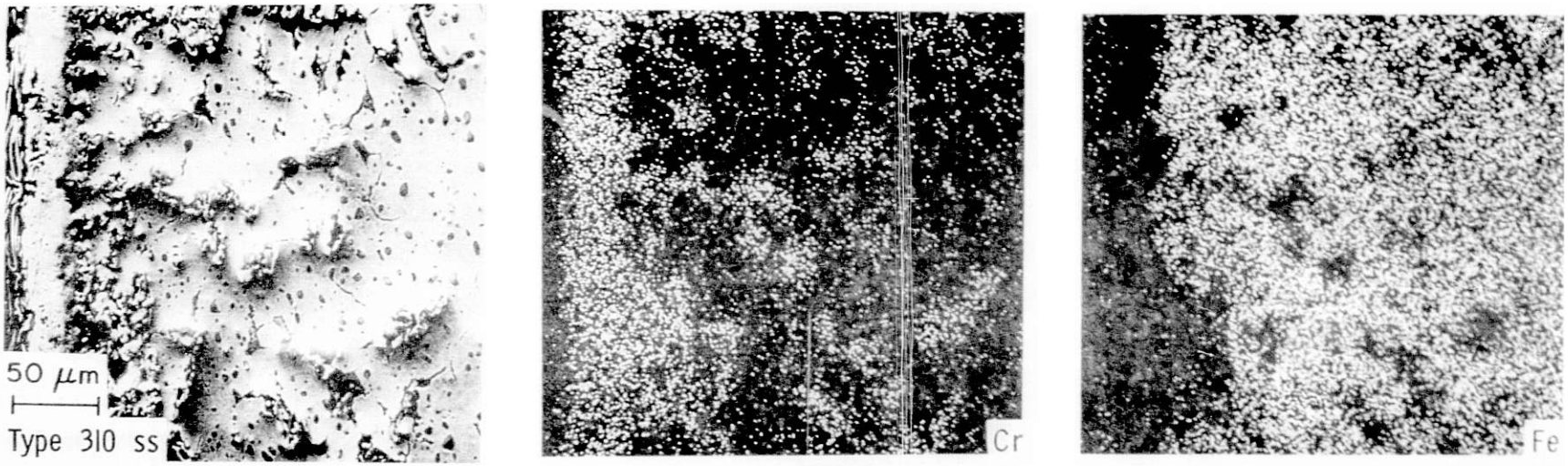


Fig. 36. X-ray Photograph and Cr, Fe, Ni, S, and O Distribution in Type 310 Stainless Steel Specimen After a 3.6-Ms Exposure to a Complex Gas Mixture at 982°C (Run B03A982). In the distribution pictures, light regions indicate a high concentration of the respective elements. ANL Neg. No. 306-79-326.

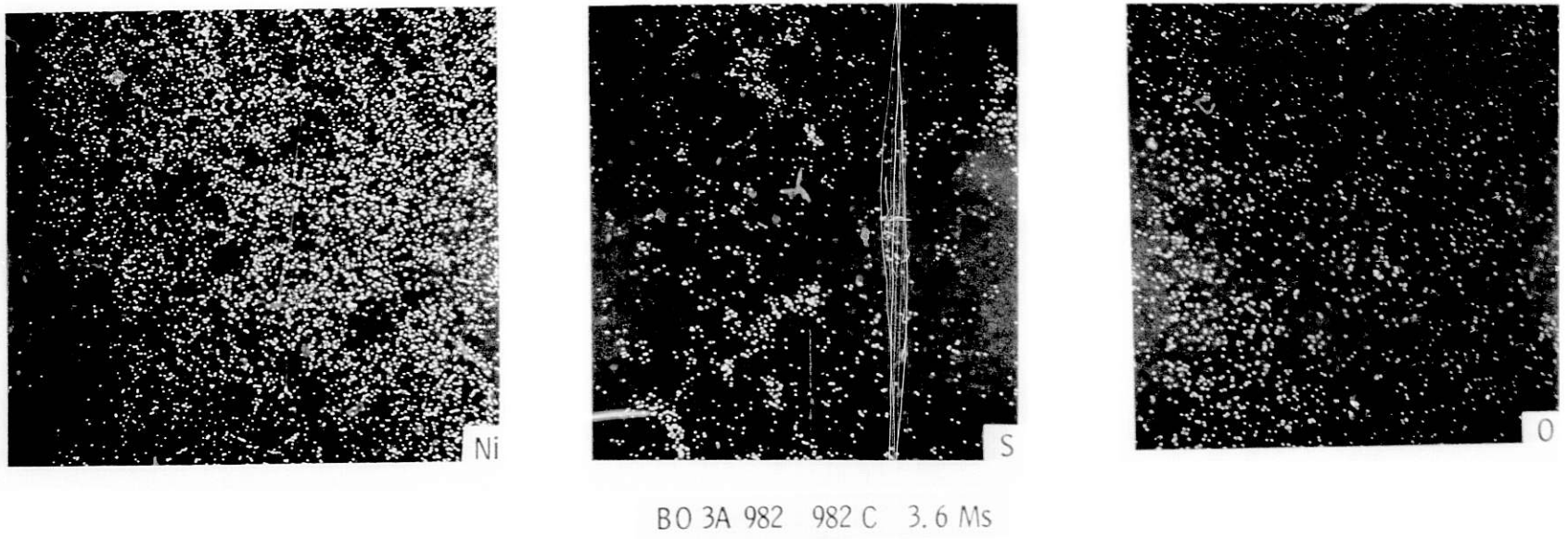


Fig. 36
(contd.)

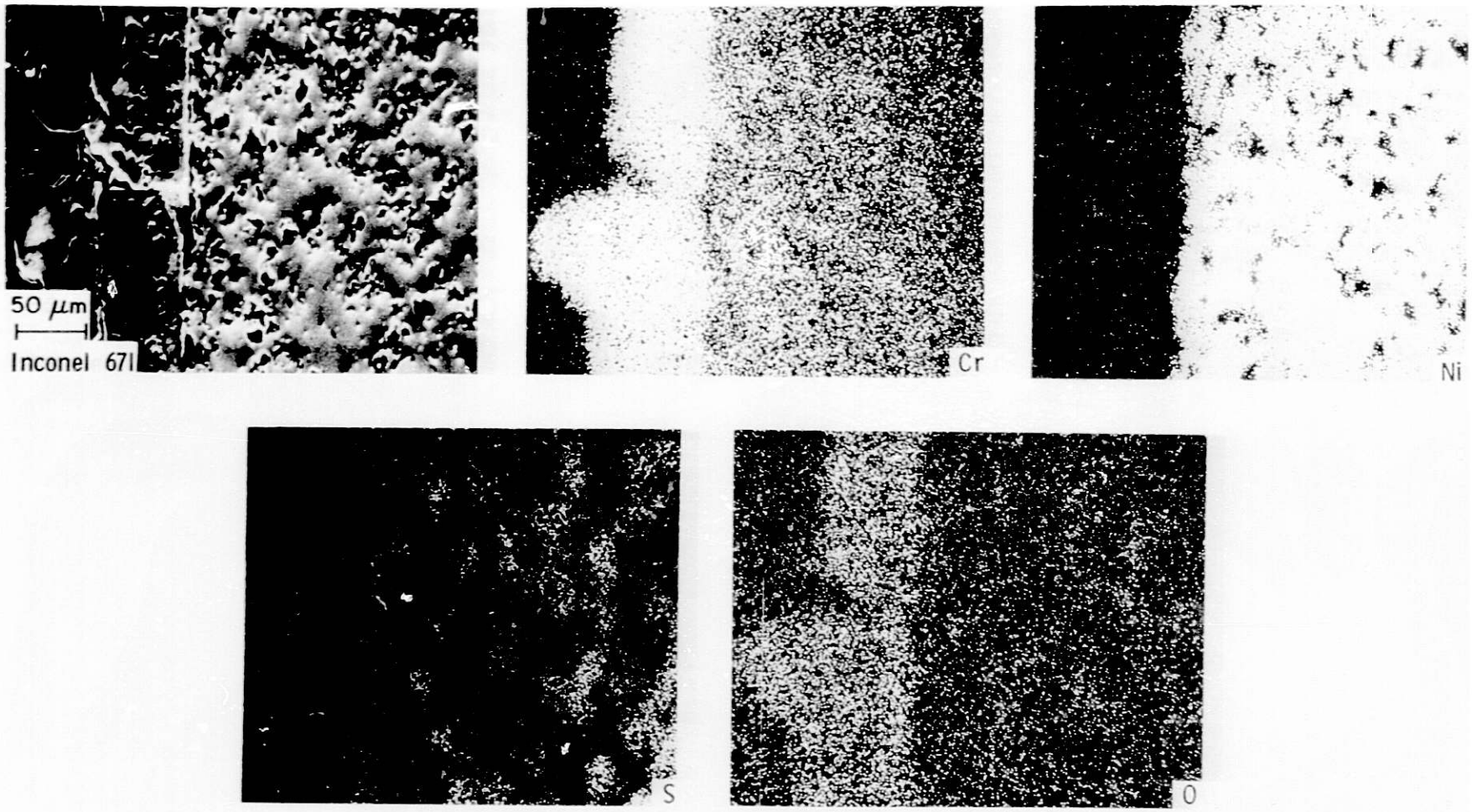


Fig. 37. X-ray Photograph and Cr, Ni, S, and O Distribution in Inconel 671 Specimen After a 3.6-Ms Exposure to a Complex Gas Mixture at 982°C (Run BO3A982). In the distribution pictures, light regions indicate a high concentration of the respective elements. ANL Neg. No. 306-79-320.


Fig. 38. X-ray Photograph and Cr, Fe, Ni, S, and O Distribution in U.S. Steel Alloy 18-18-2 Specimen After a 3.6-Ms Exposure to a Complex Gas Mixture at 982°C (Run BO3A982). In the distribution pictures, light regions indicate a high concentration of the respective elements. ANL Neg. No.306-79-318.

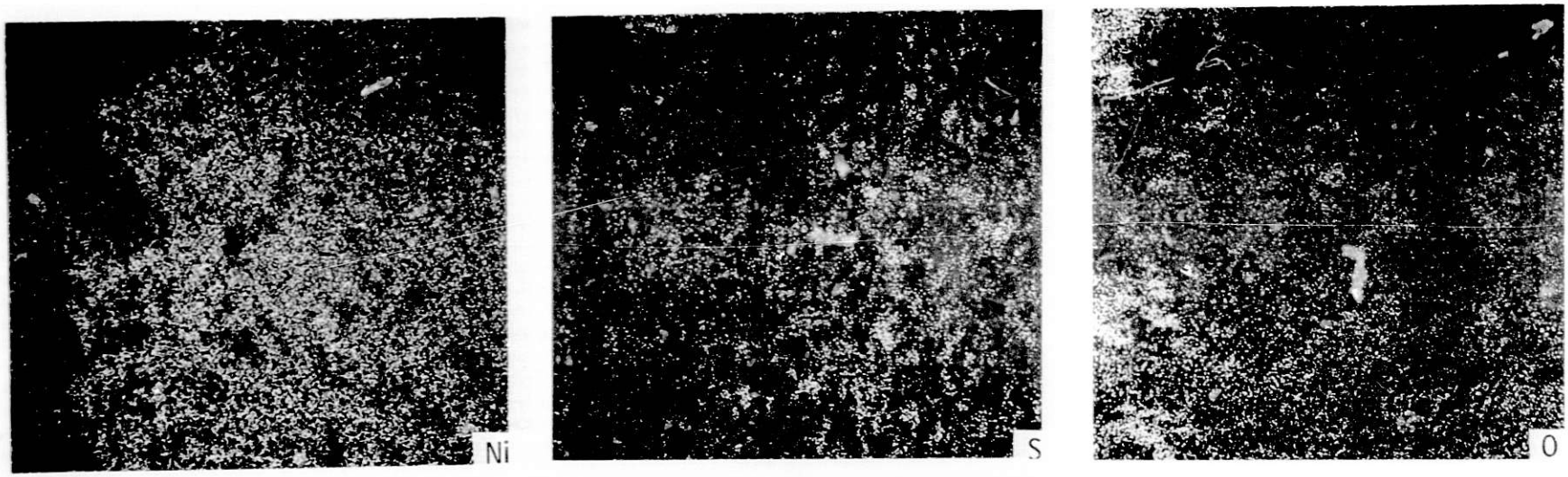


BO 3A 982 982 C 3.6 Ms

Fig. 38
(contd.)

## 2. Effect of Sulfation Accelerators and Corrosion Inhibitors on Materials in Fluidized-bed Combustion Systems *(O. K. Chopra)*

### a. Introduction

The rate and extent of sulfation of many limestones can be enhanced by impregnating the stone with sulfation accelerators, such as NaCl, $CaCl_2$, or $Na_2CO_3$. However, the use of salts in fluidized-bed combustion systems requires an evaluation of the possible effects of these constituents on the corrosion of structural materials to identify factors that could decrease the reliability and lifetime of system components. The objectives of the present program are to evaluate the effect of sulfation accelerators on the corrosion behavior of candidate materials for an atmospheric-pressure fluidized-bed combustion system, and to correlate the corrosion results with the process conditions to define maximum levels for constituents that are responsible for accelerated corrosion of plant materials.

The process-development unit, atmospheric-pressure fluidized-bed coal-combustion (AFBC) facility at Argonne National Laboratory was used to conduct the corrosion tests. Four 360-ks (100-h) corrosion tests with and without sulfation accelerators have been completed in the AFBC facility. In each test, three air-cooled corrosion probes and four corrosion coupon holders, each holding seven specimens, were installed at various locations in the fluidized bed and the freeboard sections of the combustor. The experimental conditions for the corrosion tests are given in Table IX.

The composition of the materials used for the corrosion studies is given in Table X. The materials, specimen location, and temperature of the corrosion probes for three experiments were given in the last quarterly report.[4] Analogous information for the corrosion probes in test CT-4 is given in Table XI.

### b. Results

Photographs of the air-cooled probes and coupon holders from test CT-4 are shown in Figs. 39 and 40, respectively. The air-cooled tubular specimens and the flat coupons, which were placed inside the fluidized bed, had surface oxide scales and 20- to 30-μm-thick surface deposits from the bed material. The corrosion specimens from the freeboard section of the combustor had a fine powdery deposit on the bottom surfaces only.

The corrosion specimens are being examined metallographically to evaluate the corrosion behavior in terms of the thickness of the surface scale and the depth of internal corrosive penetration. Metallographic examinations of the corrosion coupons from all the tests have been completed. Average values of the thickness of the surface scale and internal penetration for coupons placed inside the fluidized bed during test CT-4 are given in Table XII. The average temperature of these specimens was ∿1128 K (855°C).

The corrosion specimens had an ∿3-μm-thick oxide scale on the surface. The internal corrosive penetration consisted primarily of internal oxidation along the grain boundaries and patches of sulfides ahead of the oxidation front. The average thickness of surface scale and depth of internal

corrosive penetration measured on the side surfaces of the specimens are shown in Figs 41 and 42 for specimens located inside the fluidized bed at distances of 102 and 610 mm, respectively, above the fluidizing gas distributor plate. The results show that the addition of 0.3 mol % $CaCl_2$ to the fluidized bed had no significant effect on the corrosion behavior of any of the materials. In general, the addition of 0.5 mol % NaCl or 1.9 mol % $Na_2CO_3$ increased the total corrosion, i.e., the combined value of the thickness of surface scale and depth of internal corrosive penetration, for most of the materials. The high-nickel alloys, namely Inconels 601, 617, and 671, RA333, and Incoloy 800, showed a significant increase in internal corrosive penetration. Micrographs of the cross section of Inconels 617 and 671 specimens from corrosion tests in which salt was present are shown in Fig. 43.

A comparison of the corrosion behavior of Type 310 stainless steel shown in Figs. 41 and 42 indicates that the total corrosion of the material was greater at the location 102 mm above the gas distributor plate than at the 610-mm position. For Haynes Alloy 188 and Types 310 and 347 stainless steel, the total corrosion with and without salt was essentially the same. Micrographs of Type 310 stainless steel specimens located inside the fluidized bed 102 and 610 mm above the gas distributor plate are shown in Figs. 44 and 45, respectively.

Metallographic examination of the corrosion coupons from holders C-4 and C-3, which were placed in the freeboard section of the combustor 394 and 1300 mm above the top of the bed, respectively, revealed no measurable corrosion; only the cast alloy C-12 was oxidized. The average temperatures of the specimens on coupon holder C-4 for runs CT-1, -2, -3, and -4 were 946, 966, 974, and 920 K, respectively. The average temperature of the specimens placed on coupon holder C-3 was $\sim$ 100 to 110 K lower.

Scanning-electron micrographs of the surface region of alloy C-12 after corrosion tests with salt addition are shown in Fig. 46. The thickness of the surface oxide for tests CT-2 and -3 was between 100 and 140 μm, whereas in CT-4, the extent of oxidation was less because the temperature was $\sim$ 50 K lower.

c. Conclusions

**Results from the 360-ks tests indicate that the addition of 0.3 mol % $CaCl_2$ to the fluidized bed had no significant effect on the corrosion behavior of the various materials. The addition of 0.5 mol % NaCl or 1.9 mol % $Na_2CO_3$ increased the corrosion rates of most of the materials. In general, the austenitic stainless steels and Haynes Alloy 188 exhibit better resistance to accelerated corrosion in the presence of salts than the high-nickel alloys. The various materials that were located in the freeboard section of the combustor at temperatures between 800 and 975 K showed no detectable corrosion, with the exception of Fe-9Cr-1Mo steel (alloy C-12), which was oxidized. Longer-duration tests will be conducted to further evaluate the effect of salts on the corrosion behavior of various structural materials.**

TABLE IX. Calcium-to-Sulfur Molar Ratios Required to Maintain 700 ppm $SO_2$ in the Dry Off-gas

| Run No. | Addition to Fluidized Bed | Ca/S Molar Ratio |
|---|---|---|
| CT-1 | None | 3.4 |
| CT-2 | 0.3 mol % $CaCl_2$ | 3.5 |
| CT-3 | 0.5 mol % NaCl | 3.6 |
| CT-4 | 1.9 mol % $Na_2CO_3$ | 2.0 |

[a]Experimental Conditions:

Bed Temperature - 850°C
Pressure - 101.3 kPa (1 atm)
Fluidizing Velocity - 1 m/s
Fluidized-bed Height - 813 mm
Excess $O_2$ - 3% in dry off-gas
Coal - Sewickley (-12 +100 mesh), 5.46% S
Sorbent - Grove limestone (-10 +30 mesh), 95.3% $CaCO_3$

TABLE X. Composition (wt %) of Candidate Materials

| | Fe | Ni | Cr | Co | Mo | Mn | Si | C | Others |
|---|---|---|---|---|---|---|---|---|---|
| *Cobalt Base* | | | | | | | | | |
| Haynes 188 | 3.0[a] | 22.0 | 22.0 | Bal. | - | 1.25[a] | 0.3 | 0.10 | 14.0 W, 0.09 La |
| *Nickel Base* | | | | | | | | | |
| Inconel 601 | 14.1 | Bal. | 23.0 | - | - | 0.5 | 0.25 | 0.05 | 1.35 Al, 0.25 Cu |
| Inconel 617 | - | Bal. | 22.0 | 12.5 | 9.0 | - | - | 0.07 | 1.0 Al |
| Inconel 671 | - | - | - | - | - | - | - | - | - |
| Alloy 713C[b] | - | Bal. | 12.5 | - | 4.2 | - | - | 0.12 | 2.0 Nb, 0.8 Ti, 6.1 Al, 0.1 Zr |
| IN 738[b] | - | Bal. | 16.0 | 8.5 | 1.75 | - | - | 0.17 | 2.6 W, 0.9 Nb, 3.4 Ti, 3.4 Al, 1.75 Ta, 0.1 Zr |
| Hastelloy-X | 18.0 | Bal. | 22.0 | 1.5 | 9.0 | 0.5 | 0.5 | 0.10 | 0.6 W |
| RA 333 | 18.0 | Bal. | 25.0 | 3.0 | 3.0 | 1.5 | 1.25 | 0.05 | 3.0 W |
| *Austenitic Steels* | | | | | | | | | |
| Type 309 SS | Bal. | 13.5 | 23.0 | - | - | 2.0[a] | 1.0[a] | 0.20[a] | |
| Type 310 SS | Bal. | 20.5 | 25.0 | - | - | 2.0[a] | 1.5[a] | 0.25[a] | |
| Type 316 SS | Bal. | 12.0 | 17.0 | - | 2.5 | 2.0[a] | 0.5[a] | 0.10[a] | |
| Type 321 SS | Bal. | 10.5 | 18.0 | - | - | 2.0[a] | - | 0.08[a] | Ti |
| Type 347 SS | Bal. | 11.0 | 18.0 | - | - | 2.0[a] | - | 0.08[a] | Nb, Ta |
| Incoloy 800 | Bal. | 32.5 | 21.0 | - | - | 1.5 | 1.0 | 0.10 | 0.38 Al, 0.38 Ti |
| HK-40[b] | Bal. | 20.0 | 26.0 | - | 0.5[a] | 2.0[a] | 2.0[a] | 0.40 | |
| Nitronic 40 | Bal. | 6.75 | 20.5 | - | - | 9.0 | 0.25 | 0.40 | |
| *Ferritic Steels* | | | | | | | | | |
| 2¼Cr-1Mo | Bal. | | | | | | | | |
| 9Cr-1Mo | Bal. | | | | | | | | |
| E Brite 26-1 | Bal. | 0.5[a] | 26.0 | - | 1.2 | 0.4[a] | 0.4[a] | 0.01 | |
| Type 446 Steel | Bal. | - | 25.0 | - | - | 1.5[a] | 1.0[a] | 0.20[a] | |
| C-12[b] | Bal. | - | 9.0 | - | 1.1 | 0.5 | 1.0[a] | 0.20 | |
| HC[b] | Bal. | 4.0[a] | 13.0 | - | 0.5[a] | 1.0[a] | 2.0[a] | 0.50[a] | |
| CA-40[b] | Bal. | 1.0[a] | 20.5 | - | 0.5[a] | 1.0[a] | 1.5[a] | 0.3 | |

[a]Maximum.

[b]Cast alloy.

TABLE XI. Materials, Location, and Temperature of Corrosion Specimens for Run CT-4

| Corrosion-probe Designation[a] | Specimen Materials[b] | Probe Location | Mean Temperature, °C |
|---|---|---|---|
| | | Bed Section | |
| C-2 | Inconel 625, Inconel 718, Incoloy 800, Type 310 SS, Inconel 617, Type 304 SS, Type 316 SS | 102 mm above gas distributor plate | 854 |
| AC-2 | Inconel 601, Type 321 SS, Type 310 SS, Incoloy 800, Inconel 617, RA 333, Type 309 SS | 305 mm above gas distributor plate | 626,648,673[c] |
| AC-1 | Type 446 SS, Type 304 SS, 2¼Cr-1Mo Steel, Incoloy 800, 9Cr-1Mo Steel, Type 316 SS, Type 309 SS | 508 mm above gas distributor plate | 538,587,611[c] |
| C-1 | Inconel 601, Inconel 671, Hastelloy-X, Type 310 SS, Haynes 188, RA 333, Type 347 SS | 610 mm above gas distributor plate | 855 |
| | | Freeboard Section | |
| C-4 | Alloy HK-40, Alloy HC, Alloy CA-40, Alloy C-12, Alloy 713C, IN 738, Incoloy 800 | 394 mm above top of bed | 647 |
| AC-3[d] | Inconel 601, Type 321 SS, 9Cr-1Mo Steel, Incoloy 800, 2¼Cr-1Mo Steel, Type 310 SS, Type 309 SS | 1003 mm above top of bed | 548,574,579[c] |
| C-3 | Haynes 188, Hastelloy-X, Inconel 601, Inconel 617, Inconel 671, RA 333, Type 310 SS | 1308 mm above top of bed | 535 |

[a] AC = air-cooled probe; C = uncooled coupon holder.

[b] Materials listed according to stacking sequence on the probe; first specimen towards pipe bushing, last specimen near end cap.

[c] The temperatures listed for air-cooled probes were measured in specimens of Type 321 SS, Type 304 SS, Incoloy 800, and Type 309 SS.

[d] No coolant air was required for this probe.

TABLE XII. Average Thickness of Surface Scale and Depth of Internal Corrosive Penetration Measured in Corrosion Coupons from Run CT-4

| Specimen Holder | Material | Surface Scale | | | Corrosive Penetration | | | Remarks |
|---|---|---|---|---|---|---|---|---|
| | | Top | Bottom | Side | Top | Bottom | Side | |
| C-1 | Inconel 601 | 2.7[a] | 2.1 | 3.0 | 6.8 | 12.3 | 16.6 | Some grain-boundary attack ~ 50 μm deep. |
| | Inconel 671 | 7.6 | 4.7 | 3.1 | 50.8 | 46.6 | b | Corrosion behavior not uniform. |
| | Hastelloy-X | 3.0 | 3.0 | 2.9 | - | 10.2 | 12.9 | |
| | Type 310 SS | 3.4 | 3.4 | 3.2 | 13.5 | 17.8 | 12.8 | Internal corrosion mainly sulfides. |
| | Haynes 188 | 2.1 | 1.8 | 2.1 | 8.0 | 9.8 | 9.5 | Some grain-boundary attack ~ 24 μm deep. |
| | RA 333 | 2.0 | c | 2.4 | 9.8 | 11.8 | 10.2 | |
| | Type 347 SS | 2.7 | 2.7 | 2.4 | 10.2 | 9.8 | 9.3 | Internal corrosion mainly sulfides. |
| C-2 | Inconel 625 | 3.8 | 3.1 | 4.1 | 21.1 | 22.9 | 23.7 | |
| | Inconel 718 | 2.2 | 2.2 | 2.7 | 11.0 | 10.2 | 14.6 | |
| | Incoloy 800 | 3.4 | 3.6 | 3.6 | 21.2 | 25.0 | 19.5 | |
| | Type 310 SS | 3.4 | 3.2 | 3.4 | 18.2 | 18.2 | 19.1 | |
| | Inconel 617 | 3.2 | 3.6 | 3.6 | 25.4 | 21.2 | 26.5 | |
| | Type 304 SS | 2.9 | 2.4 | 3.0 | 18.6 | 16.2 | 22.0 | |
| | Type 316 SS | 3.4 | 3.4 | 3.4 | 16.1 | 22.2 | 23.3 | |

[a] All measurements in μm.

[b] Extensive corrosion on one side of the specimen and very little internal corrosive penetration on the other.

[c] Surface scale spalled.

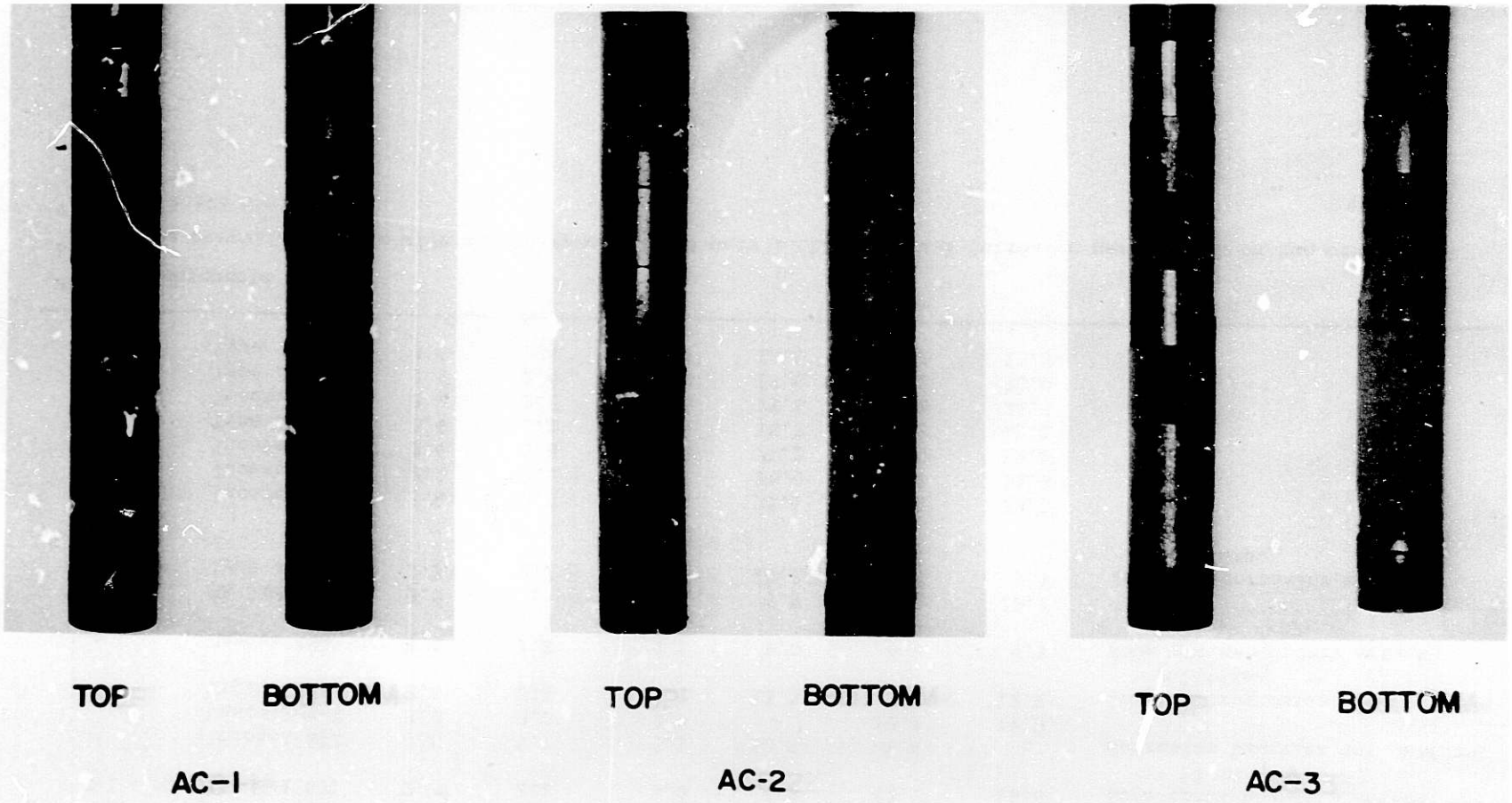


Fig. 39. Top and Bottom Views of Air-cooled Probes from Corrosion Test Run CT-4. Specimens stacked from top to bottom according to the sequence given in Table XI. ANL Neg. No. 306-79-386.

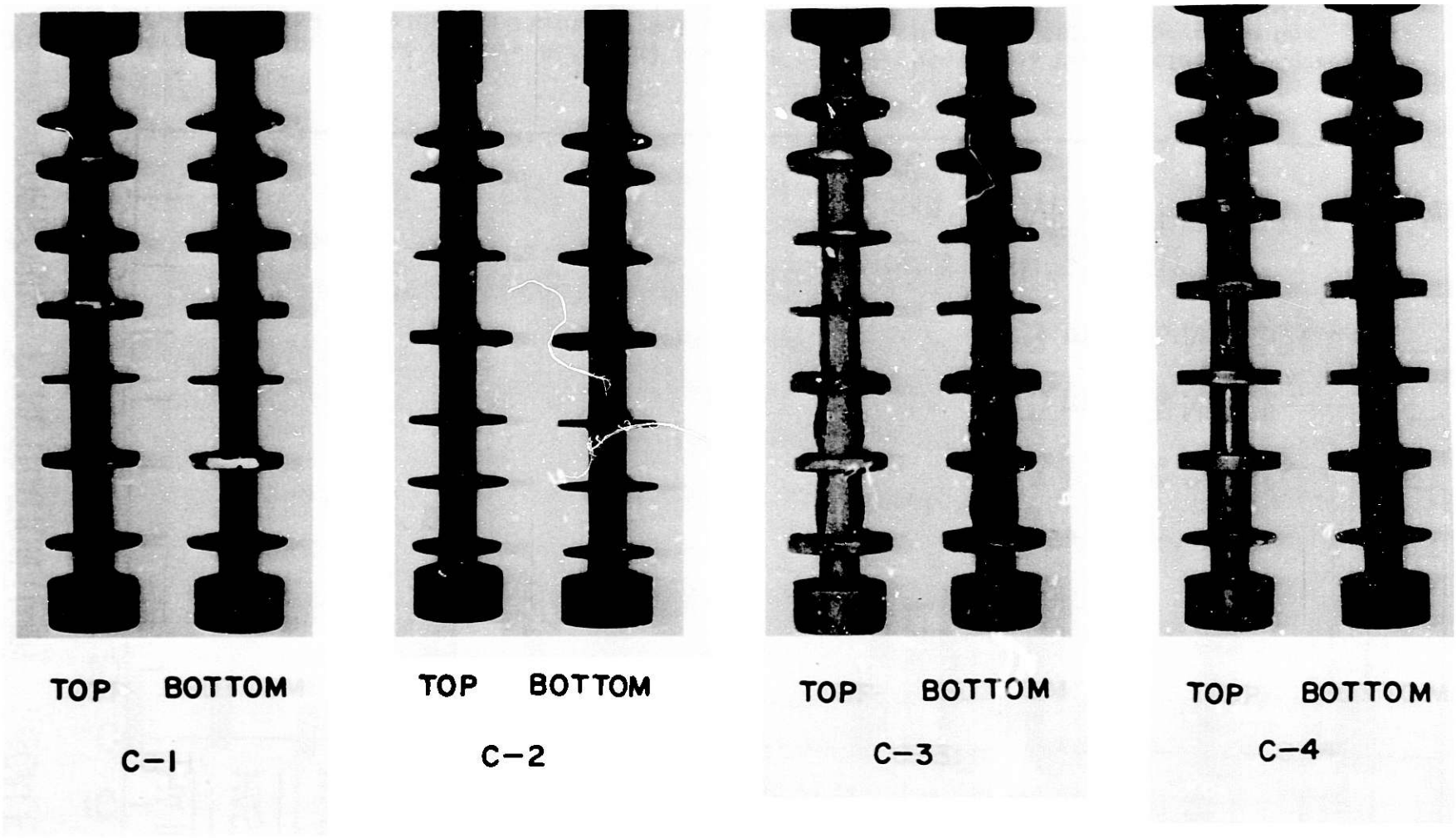


Fig. 40. Top and Bottom Views of Coupon Holders from Corrosion Test Run CT-4. Specimens stacked from top to bottom according to the sequences given in Table XI. ANL Neg. No. 306-79-385.

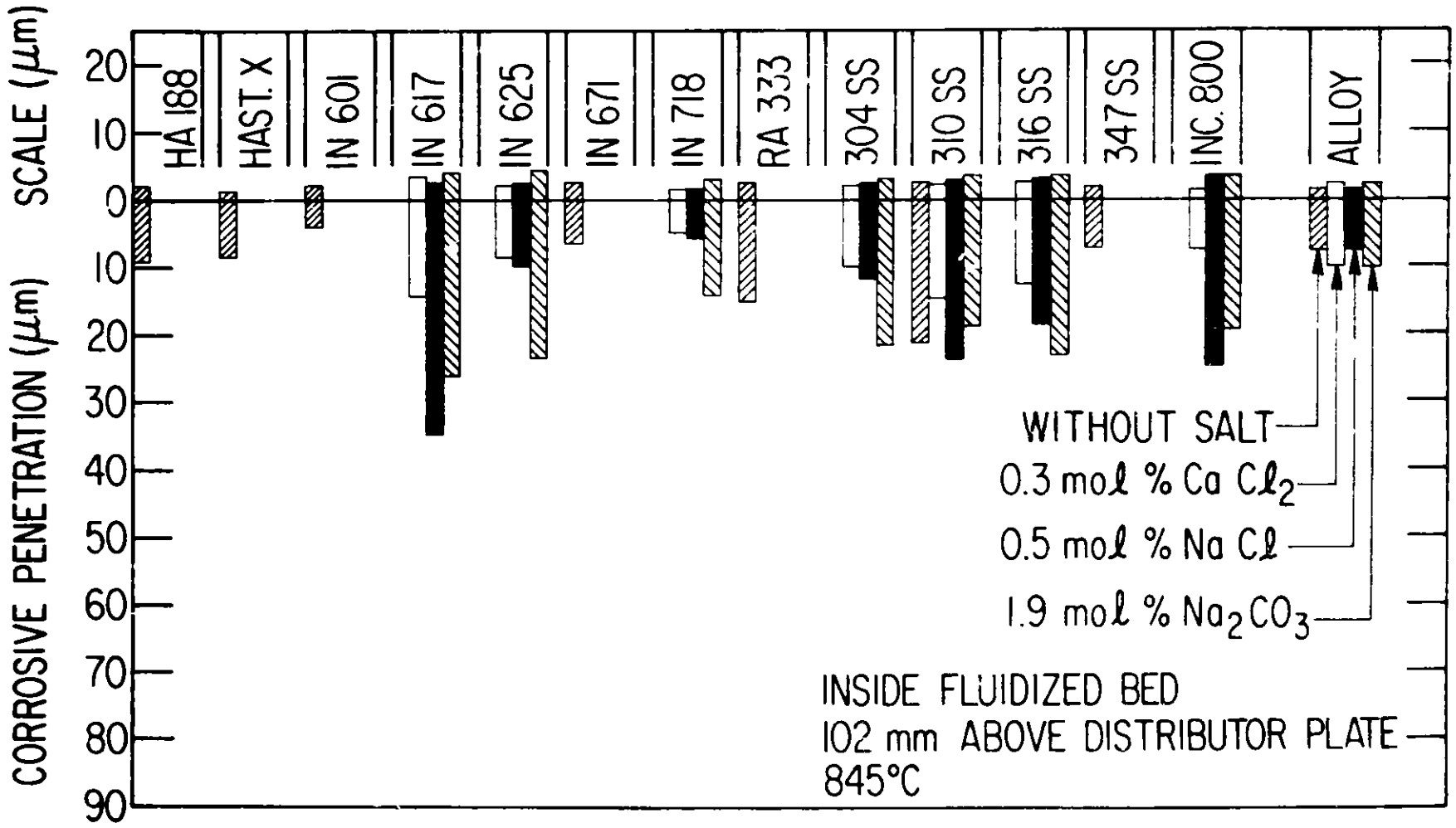


**Fig. 41.** **Average Thickness of Surface Scale and Depth of Internal Corrosive Penetration for Corrosion Coupons Exposed Inside the Fluidized Bed for 360 ks at a Location 102 mm Above the Gas Distributor Plate.** ANL Neg. No. 306-79-380.

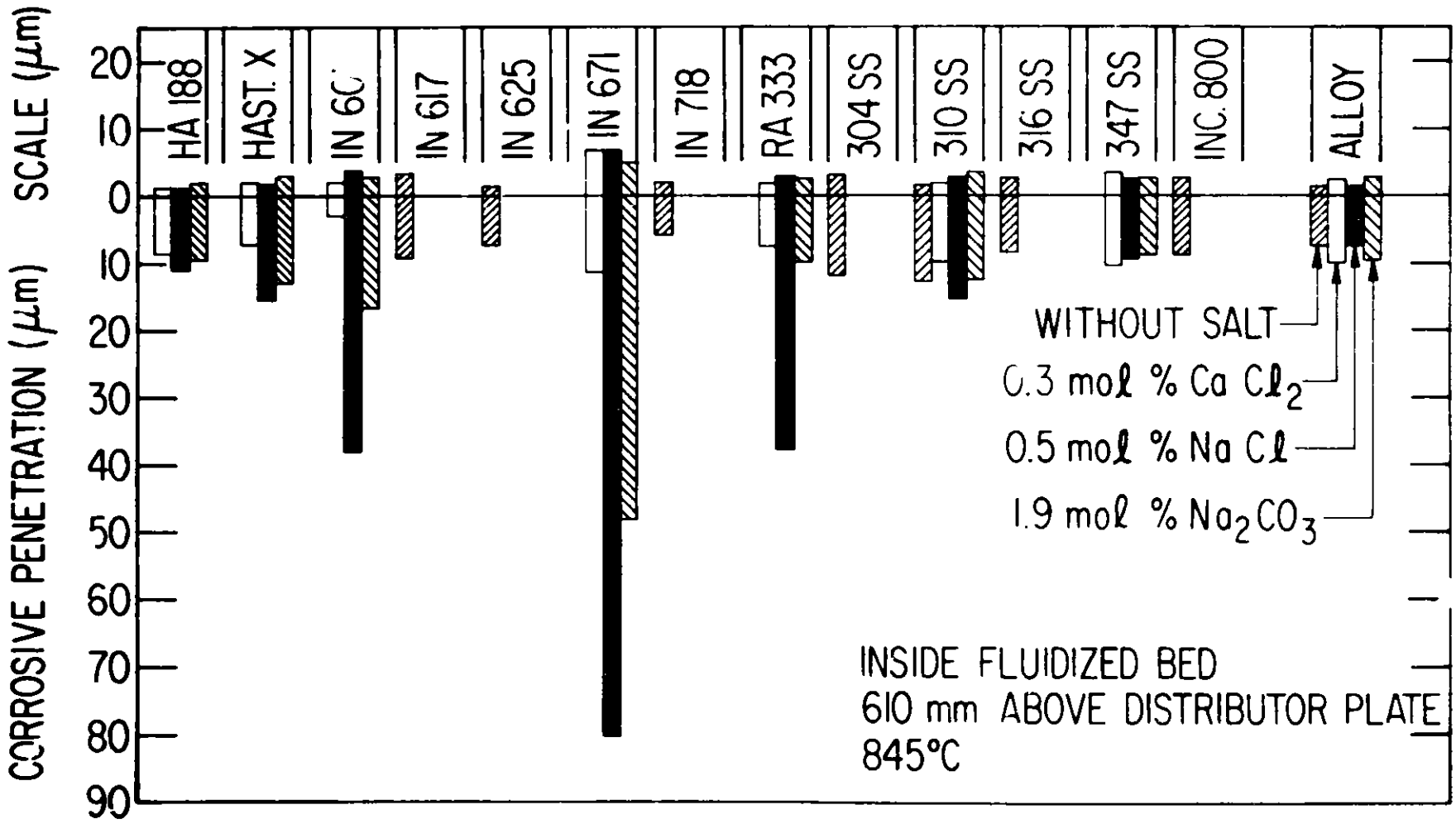


Fig. 42. **Average Thickness of Surface Scale and Depth of Internal Corrosive Penetration for Corrosion Coupons Exposed Inside the Fluidized Bed for 360 ks at a Location 610 mm Above the Gas Distributor Plate.** ANL Neg. No. 306-79-379.

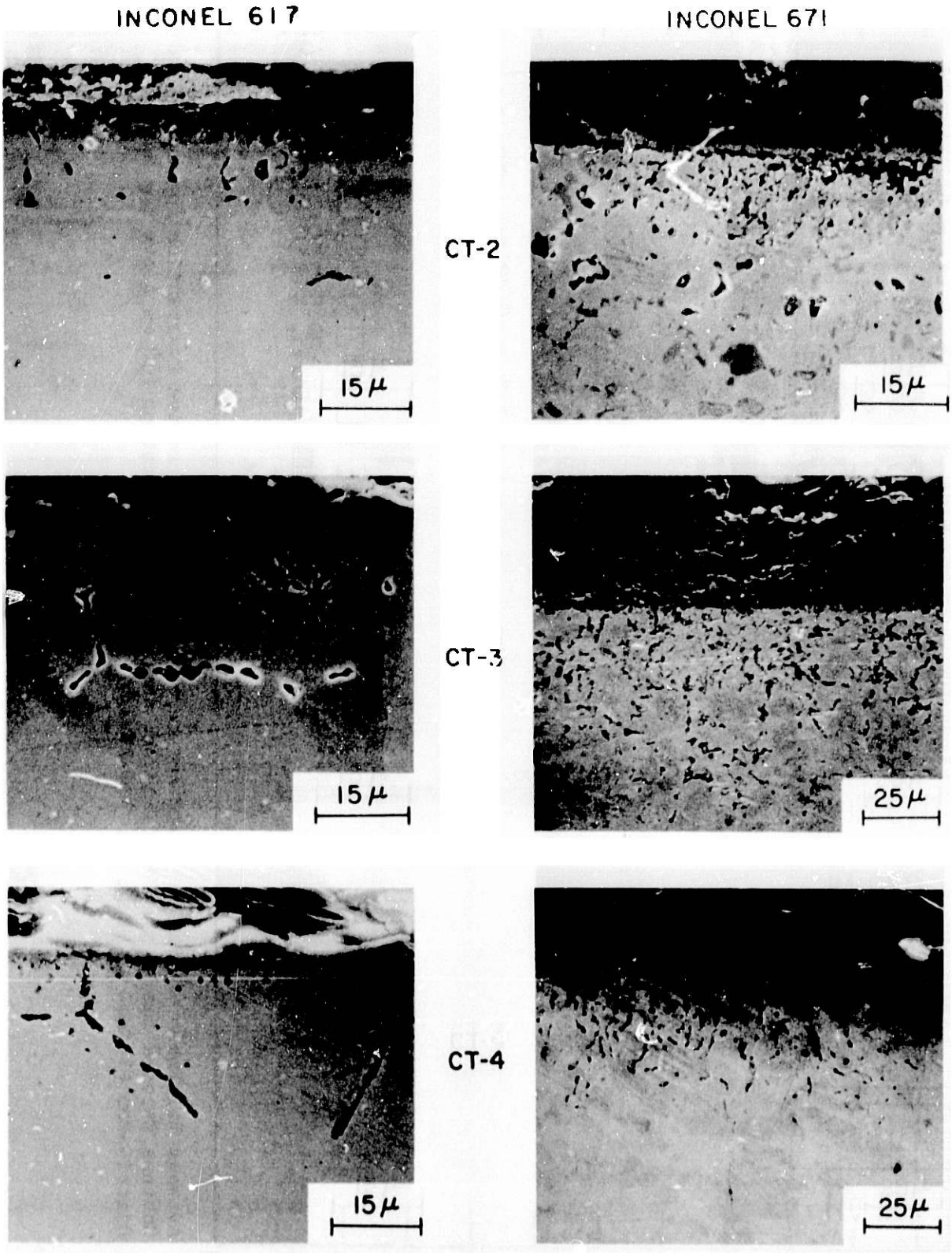


Fig. 43. SEM Photographs of Inconel 617 and 671 After a 360-ks Exposure at 1123 K Inside the Fluidized Bed. ANL Neg. No. 306-79-382.

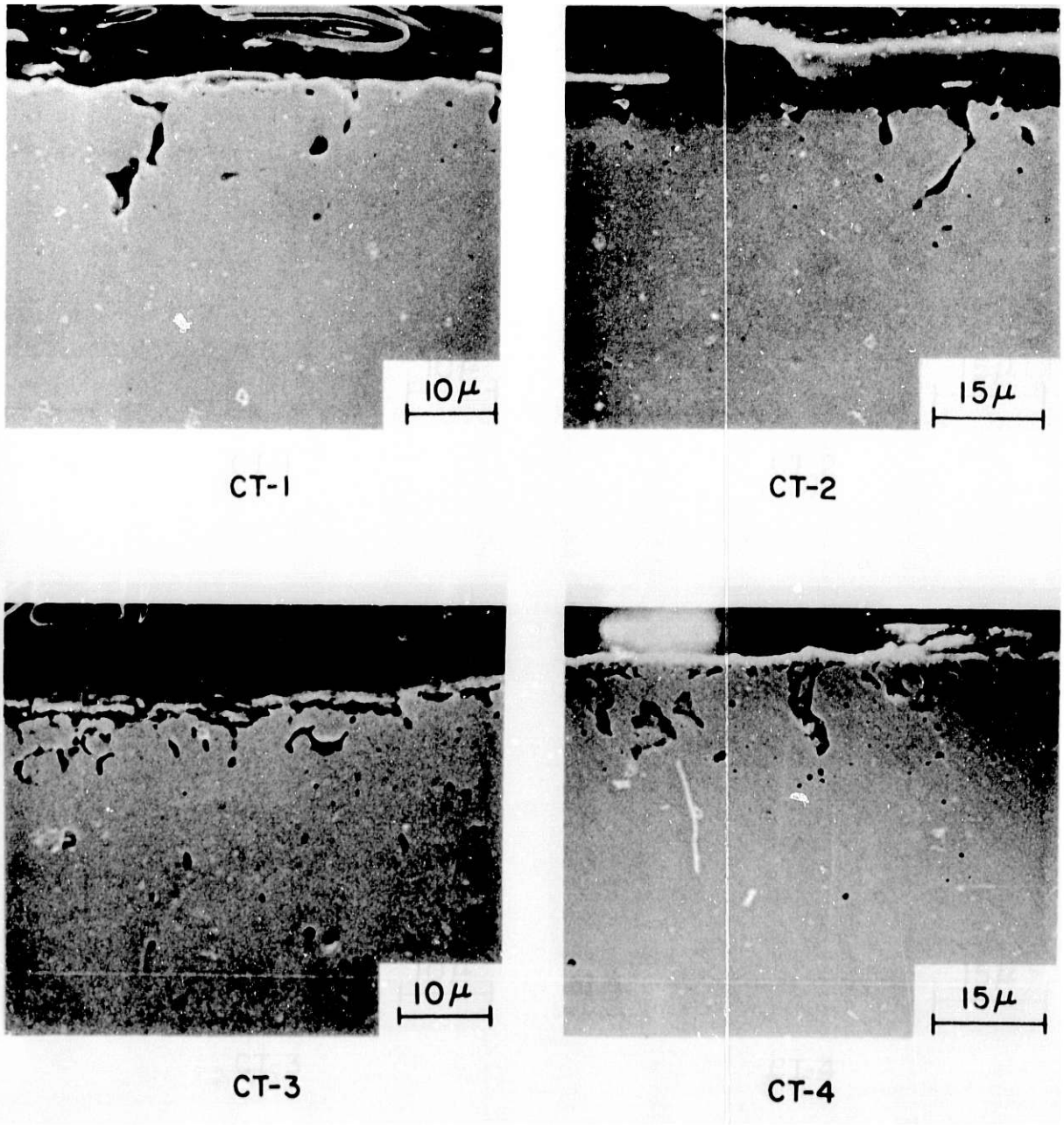


Fig. 44. SEM Photographs of Type 310 Stainless Steel After a 360-ks Exposure at 1123 K Inside the Fluidized Bed at a Location 102 mm Above the Gas Distributor Plate. ANL Neg. No. 306-79-381.

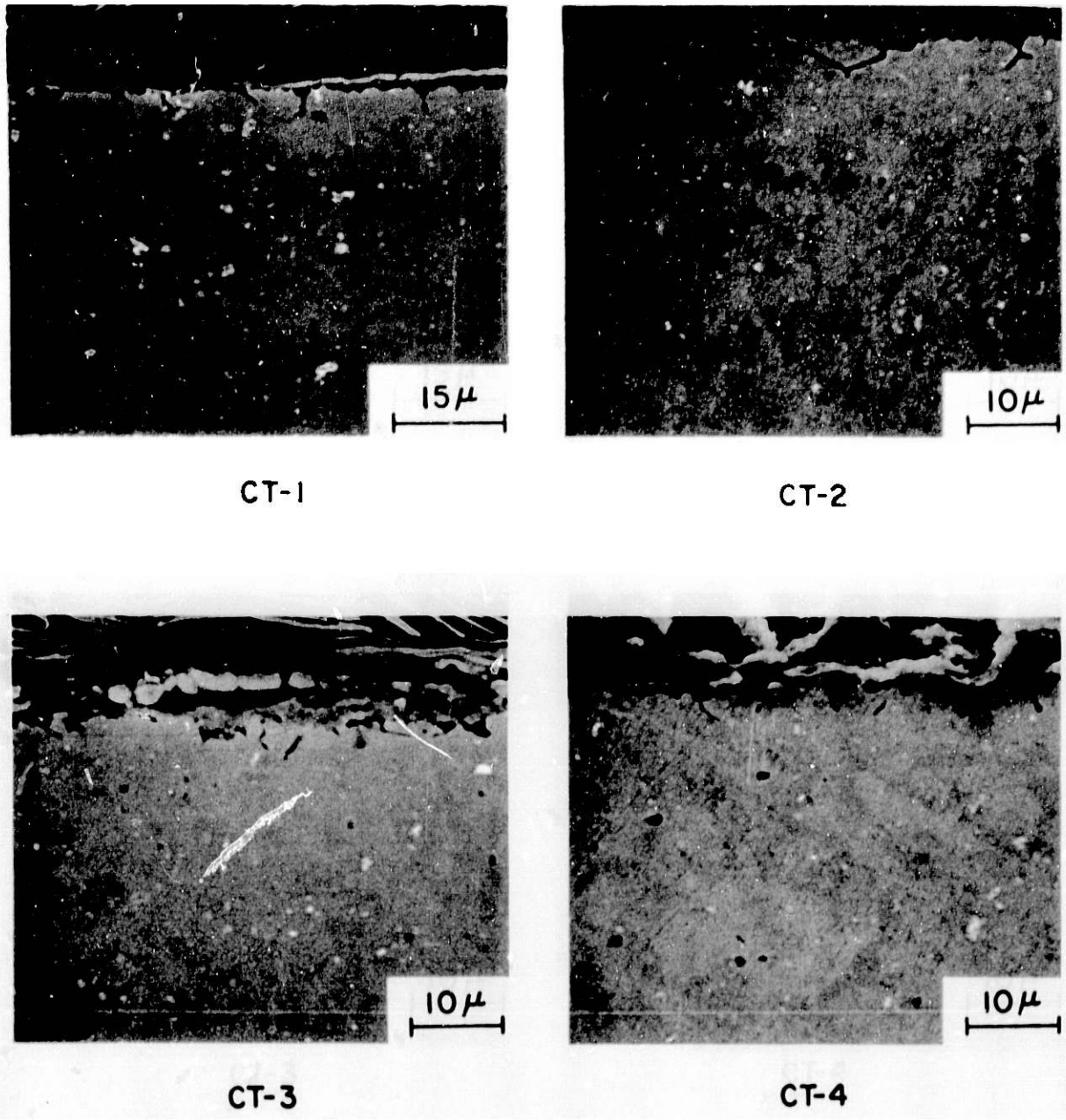


Fig. 45. SEM Photographs of Type 310 Stainless Steel After a 360-ks Exposure at 1123 K Inside the Fluidized Bed at a Location 610 mm Above the Gas Distributor Plate. ANL Neg. No. 306-79-383.

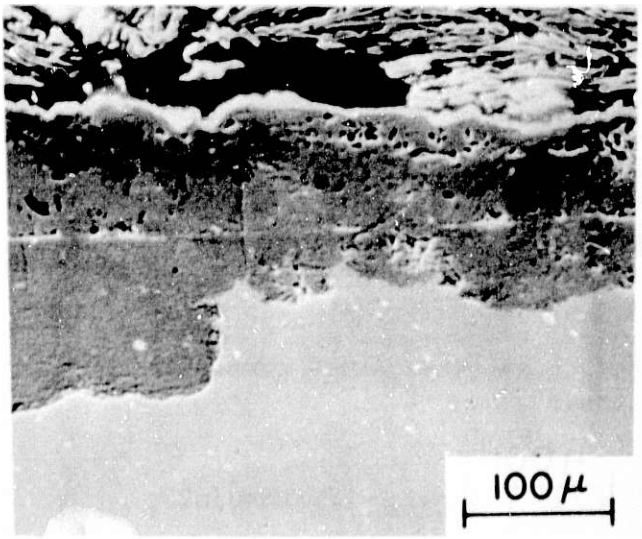


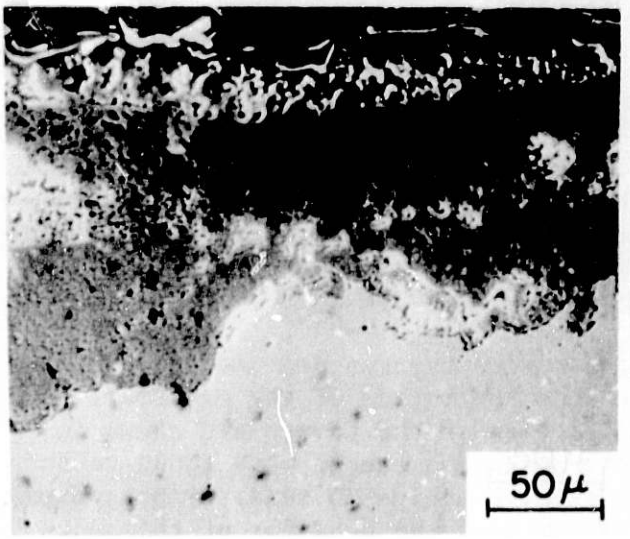


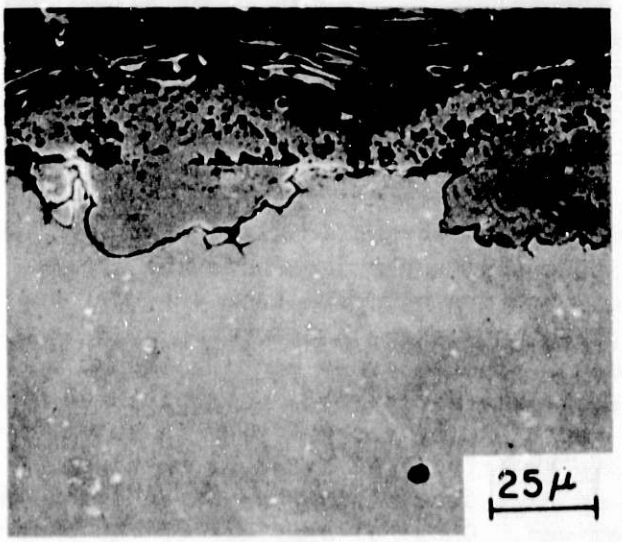


Fig. 46. SEM Photographs of Alloy C-12 After a 360-ks Exposure in the Freeboard Section of the Combustor. ANL Neg. No. 306-79-384.

Task E -- Erosion Behavior of Materials in Coal-conversion Processes *(J.Y. Park, S. Danyluk, and W.J. Shack)*

During this quarter, the repair of the corrosion/erosion test apparatus has continued. The cause of the cooling-water leak which resulted in a flood during the previous corrosion-calibration test is being sought. However, accurate control of the water content in the test environment may not be achievable because of condensation at cold regions of the test chamber. The Kanthal heating element was discovered to be damaged during the previous test run, and is being replaced.

After the repair is completed, high-temperature corrosion calibration and screening tests will be resumed.

Task F -- Component Performance and Failure Analysis *(S. Danyluk, G.M. Dragel, and L.E. Pahis)*

a. Examination of Components from the Grand Forks Energy Technology Center

A number of failed components from the Grand Forks Energy Technology Center fixed-bed slagging gasifier facility and the liquefaction facility were examined to determine the failure cause or causes. The components included three tuyere tips that are used to continuously feed an oxygen-steam mixture into the gasifier, a vapor-barrier liner from the gasifier, and three small flow-control valves from the liquefaction unit. The results of the investigations are summarized below.

*(1) Tuyere Tips* - Four water-cooled tuyeres are used to continuously inject an oxygen-steam mixture into the bottom of the gasifier. A schematic of the gasifier and a detailed view of the tuyere are shown in Fig. 47. The tuyeres, made of Type 347 stainless steel, were found to be severely corroded, pitted and cracked after a series of runs. Since other tuyeres were subjected to similar environments, the behavior of this particular set was unexplained and an analysis was conducted to determine whether a materials problem was the cause of the failure. The exact operating temperature of the tuyeres is unknown but the maximum should be $\sim$ 1370°C, the temperature of the coal slag, and the minimum $\sim$ 30°C, the approximate temperature of the exit water from the taphole cooling coil. The composition of the atmosphere in the approximate vicinity of the tuyeres is unknown. The failure was noticed after $\sim$ 300 h of operation at these conditions.

The tuyeres are constructed as shown schematically in Fig. 48. A weld joins the outer shell with the inner sleeve that conducts the steam-oxygen mixture. A photograph showing a sectioned tuyere from the west end of the gasifier is shown in Fig. 49a; the corrosion that occured as a result of exposure to the atmosphere is evident. In the cross section shown in Fig. 49b, the weld and base metal are clearly delineated. A photograph of a quarter section of a tuyere from the south end of the gasifier is shown in Fig. 50a. Cracks at the weld-substrate interface can be seen; they appear more clearly as intergranular cracks in Fig. 50b. This type of behavior was observed in all three tuyere tips examined. Chemical analysis of the base

material did not produce any unusual findings, nor did the microhardness tests. At present, the cracks are attributed to stress corrosion related to the weld and the corrosive environment in the gasifier. The electron microprobe will be used to determine the chemistry of the corrosive scale at the OD and in the grain boundaries.

*(2) Vapor-barrier Liner* - A perforation in the liner, a Type 310 stainless steel shroud from the upper section of the gasifier vessel, was observed by Mr. P. Dempsey of Stearns-Roger while the gasifier was being dismantled for relocation into an adjacent structure. The shroud had been in intermittent service in the coal pilot plant for ∿ 21 years with temperature excursions as high as 1800°F. A summary of his report stated that the vessel had become red around the 6-inch nozzle during its next to last run before dismantling but that ultrasonic inspection revealed no damage to the vessel wall. Upon inspection it was noticed that the shell covering the fibraflex insulation had corroded areas everywhere except at the top of the dome. The shroud was 10-gauge when originally installed in 1957. Sections of the shroud and tar-impregnated sections of insulation were shipped to ANL for investigation.

Cross sections of the vapor barrier were polished and electron-microprobe data were obtained. The results, shown in Fig. 51, confirm that sulfur has penetrated the grain boundaries and formed chrome sulfides while iron and nickel are depleted in the grain boundaries.

The as-polished cross section was subsequently etched in NaOH at 1.5 V for 2 s, revealing the presence of sigma phase at the grain boundaries (Fig. 52). It has been found that the formation of sigma phase in ferritic and austenitic stainless steels during long periods of exposure to temperatures in the 560-980°C range causes embrittlement after cooling to room temperature.[15] Sigma phase is formed by the transformation of ductile delta-ferrite[16] and its effects on ductility of Type 310 stainless steel have previously been reported.[17] However, the formation of sigma phase as a result of the exposures cited above is only now becoming apparent. Components containing sigma phase must be handled carefully to prevent fracturing.

*(3) Flow-control Valves* - Three small flow-control valves from the slurry-letdown system of the liquefaction facility were found to be leaking. A visual inspection revealed "wire drawing" on the seating surfaces. The valves, manufactured by Masoneilan, operate at ∿ 200°C and ∿ 4000 psi. Two of the failed stems were of Type 316 stainless steel while the third was of the same base material with a Stellite B coating. A schematic of the valve cross section is shown in Fig. 53.

Photographs of all three valve stems are shown in Fig. 54. Scanning electron micrographs (SEMs) of the eroded regions of two of the stems are shown in Figs. 55 and 56. Figure 55 shows SEMs of two regions of one of the uncoated valve seats. The region pictured in Fig. 55(a) was subject to a low particle-impact angle; that shown in (b) and (c) was subject to a high angle. Plowing and shearing, as well as the slowing down and stopping of the impinging particles, are clearly evident in both regions. Figure 56 shows the results of the erosion of the Stellite B coating. Regions with both high and low impact angles are again present. While the general pattern of erosion

is similar to that shown in Fig. 55, the microstructural surface features are distinctly different. The more ductile austenitic material (Fig. 55) is plowed more easily than the harder Stellite B coating (Fig. 56). When this report was prepared, the service histories of the three valves were not available for comparison. This will be done in the subsequent report.

b. Morgantown Energy Technology Center - Ball Valve Leakage in the Valve Dynamic Test Unit

A 15.24-cm ball valve from the Morgantown Energy Technology Center (METC) Valve Dynamic Test Unit developed excessive leakage while being tested in simulated lockhopper service. The valve failed to close completely after 3,134 cycles. The leakage was partly attributed to limestone fines wedged between the seats and body. It was observed at METC that the chrome oxide coating on the valve seats and ball had chipped and the valve stem was bent and twisted. The seats, ball and stem were shipped to Argonne National Laboratory-Materials Science Division for analysis of the integrity of the valve-seat coating.

A metallurgical examination of the valve seats revealed that the chipping of the coating had occurred at the valve-stem slot and in the over-spray area, regions which are not usually in contact with the ball. This should not have affected valve performance. A metallographic examination of the coating-substrate interface did not reveal any obvious defects. The coating thickness on the ball varied by $\sim$ 50% between areas in contact and not in contact with the seat. Wear of the coating might have contributed to the high leakage rates. However, the variation in thickness was within the manufacturer's specification. In summary, the leakage of the valve cannot be directly attributed to a materials cause, other than the possibility that chips from the coating wedged between the valve seat and body. The deformation of the stem resulted from the excessive torque (calculated at > 470 ft-lb) applied by the actuator to rotate the valve.

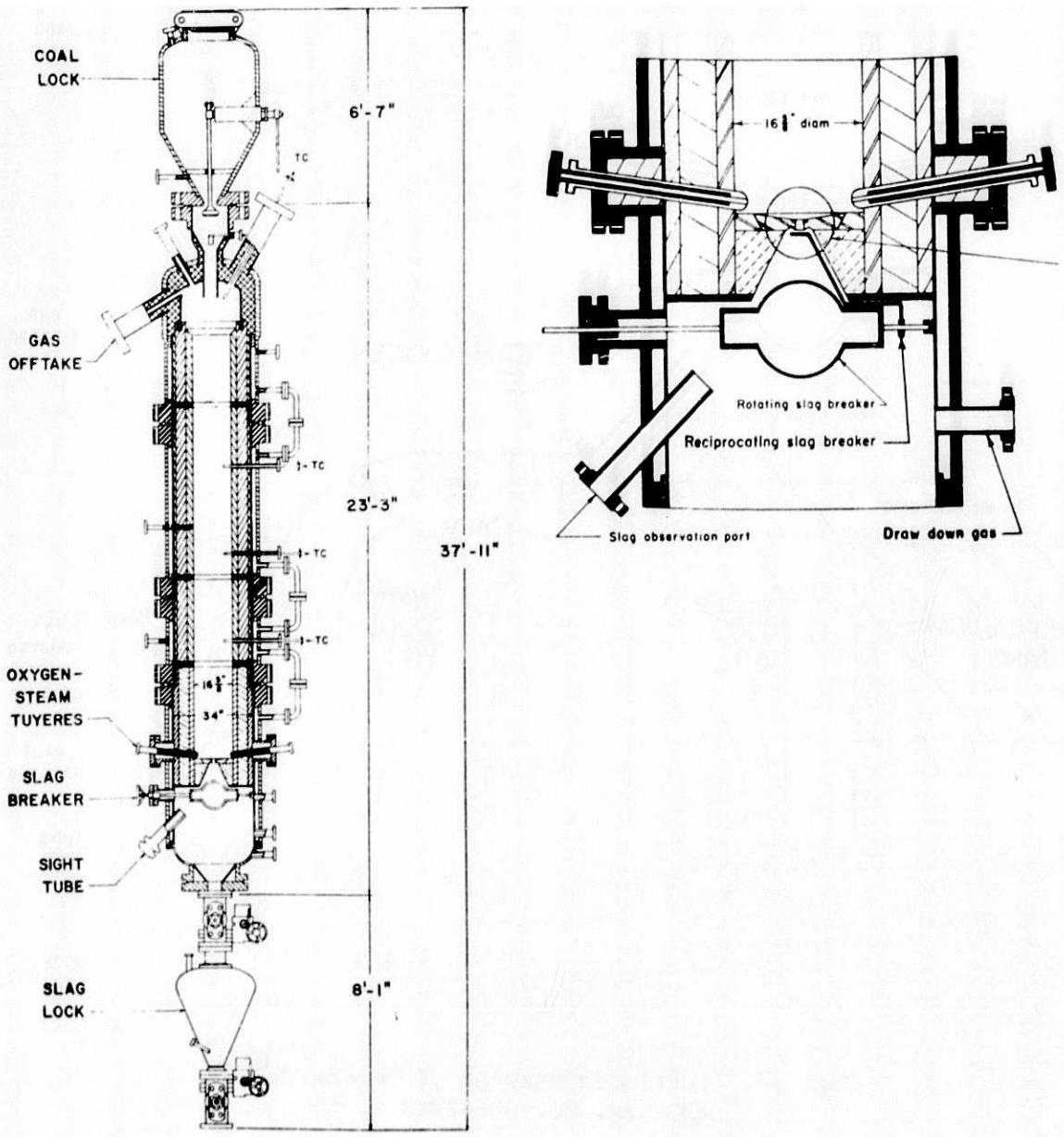


Fig. 47. Schematic of the Grand Forks Energy Technology Center Slagging Gasifier and a Detailed View of the Tuyere Region. ANL Neg. No. 306-78-567R.

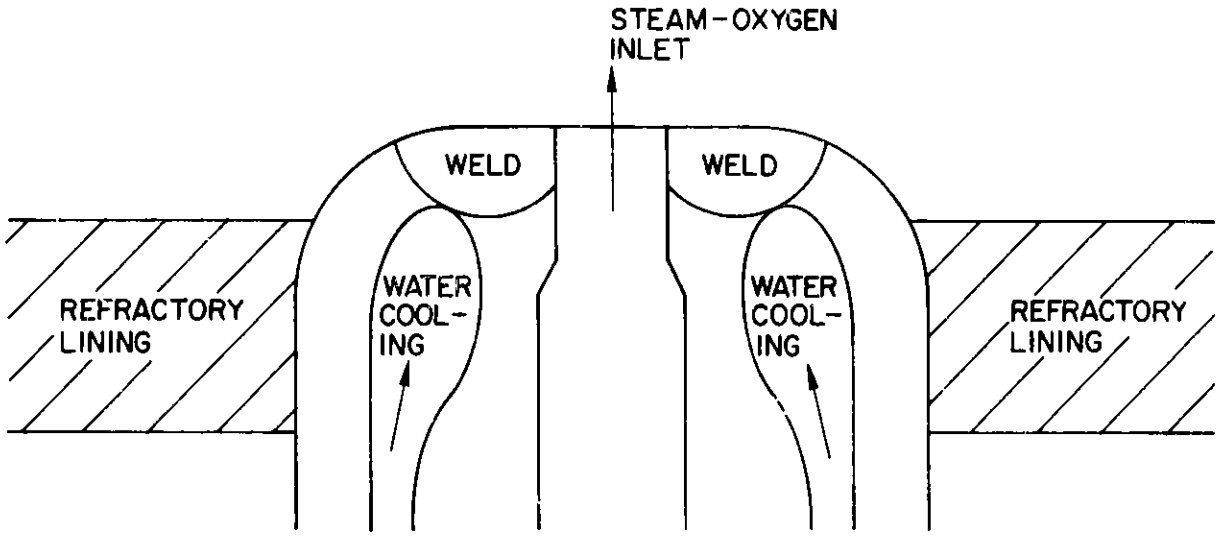


Fig. 48. Schematic Drawing of Tuyere Tip.
ANL Neg. No. 306-79-534.

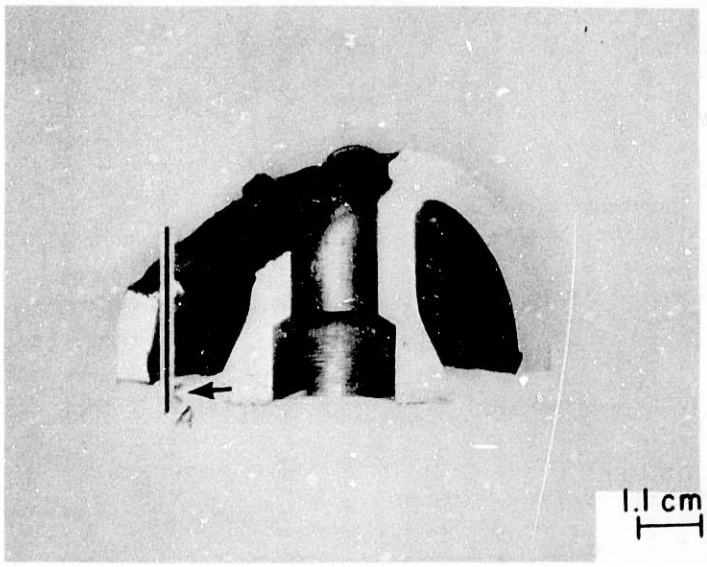


(a)

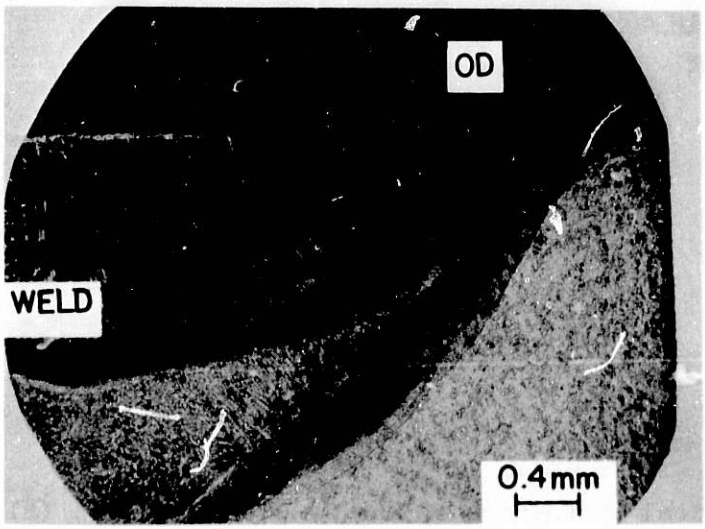


(b)

Fig. 49. (a) Optical Photograph of the West Tuyere Tip; (b) Micrograph of a Polished and Etched Cross Section through the Region Indicated in (a), Showing the Weld Metal and Base Metal. ANL Neg. No. 306-79-543.

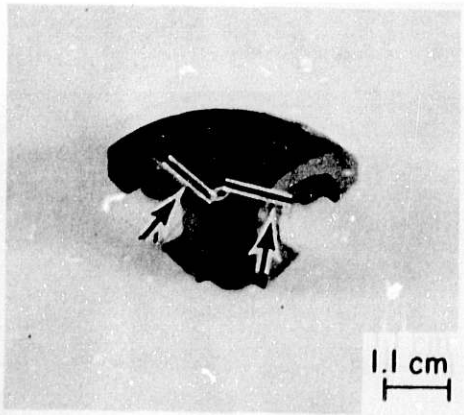


(a)

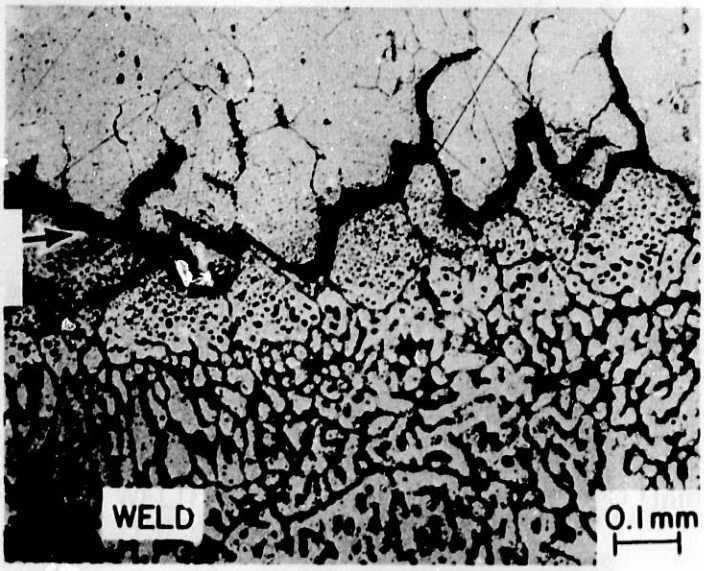


(b)

Fig. 50. (a) Optical Photograph of the South Tuyere Tip; (b) Micrograph of Polished and Etched Cross Section through the Region Indicated in (a). Intergranular cracks can be seen at the weld-base metal interface. ANL Neg. No. 306-79-550.

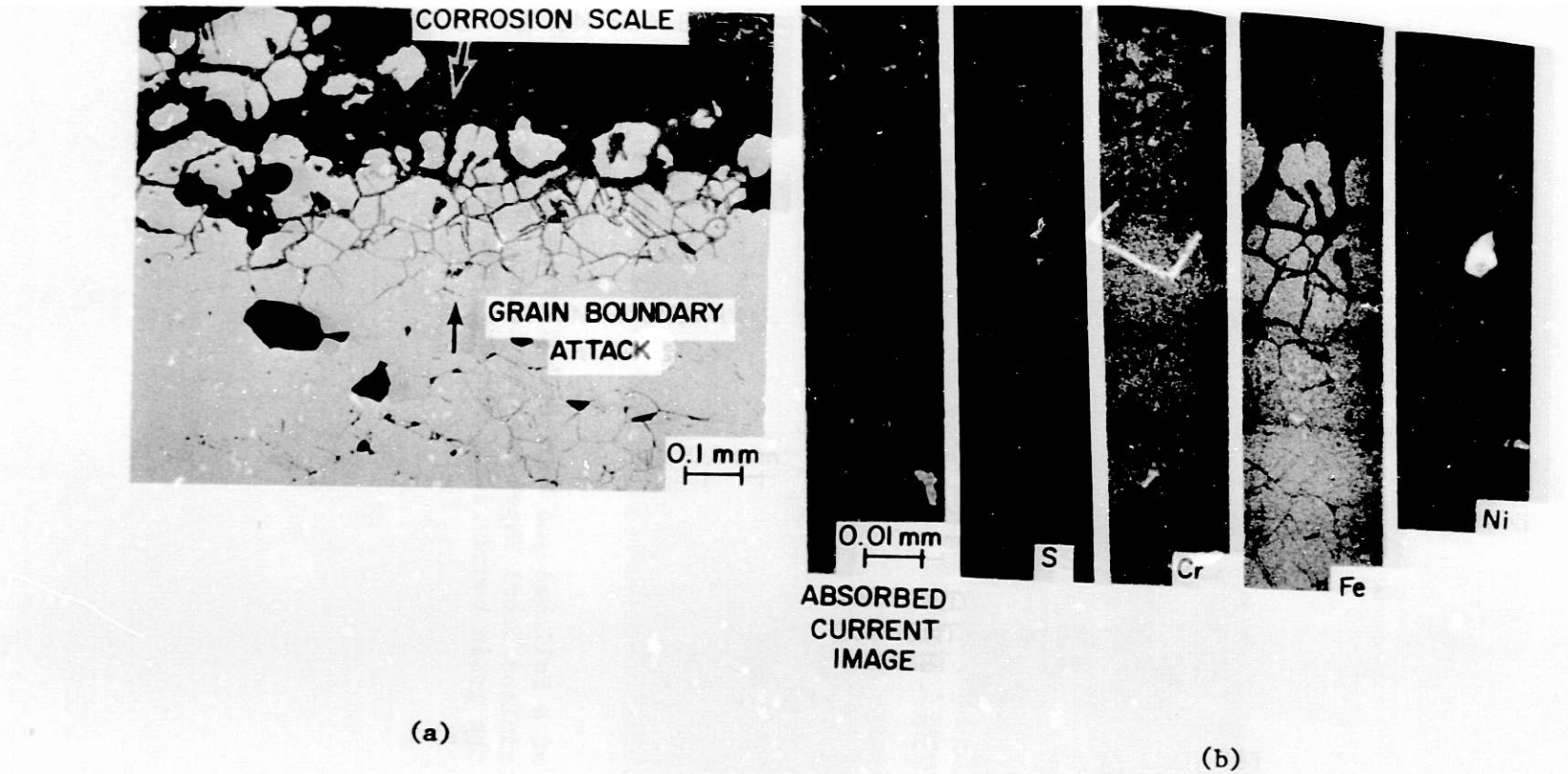


Fig. 51. (a) Micrograph of a Cross Section of the Type 310 Stainless Steel Vapor-barrier Liner; (b) Electron Microprobe Results Showing the Absorbed-current Image and the Sulfur, Chromium, Iron and Nickel Distributions in the Corrosion Scale. ANL Neg. No. 306-79-546.

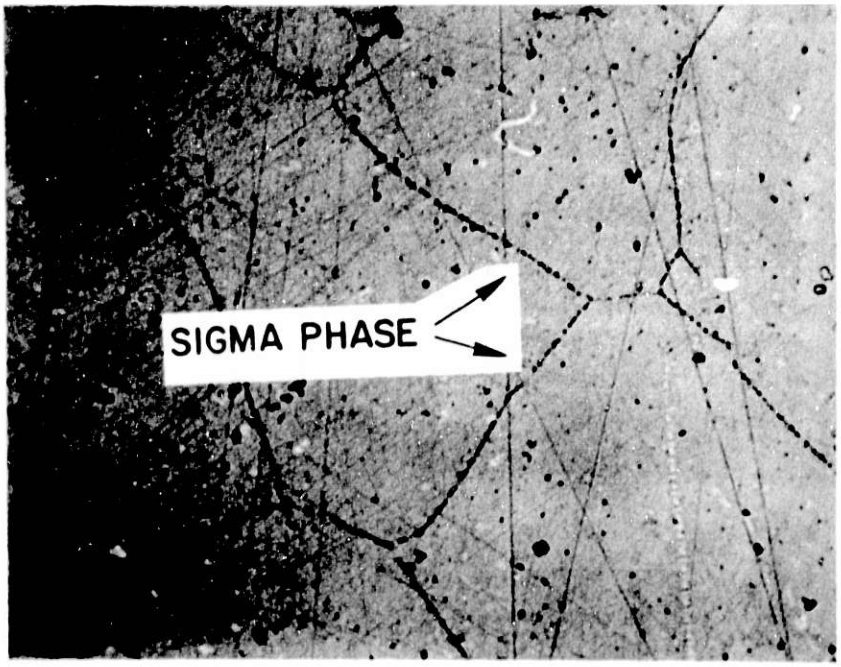


Fig. 52. Micrograph of a Polished and NaOH-etched Cross Section of the Type 310 Stainless Steel Vapor-barrier Liner. Sigma phase is evident at the grain boundaries. ANL Neg. No. 306-79-551.

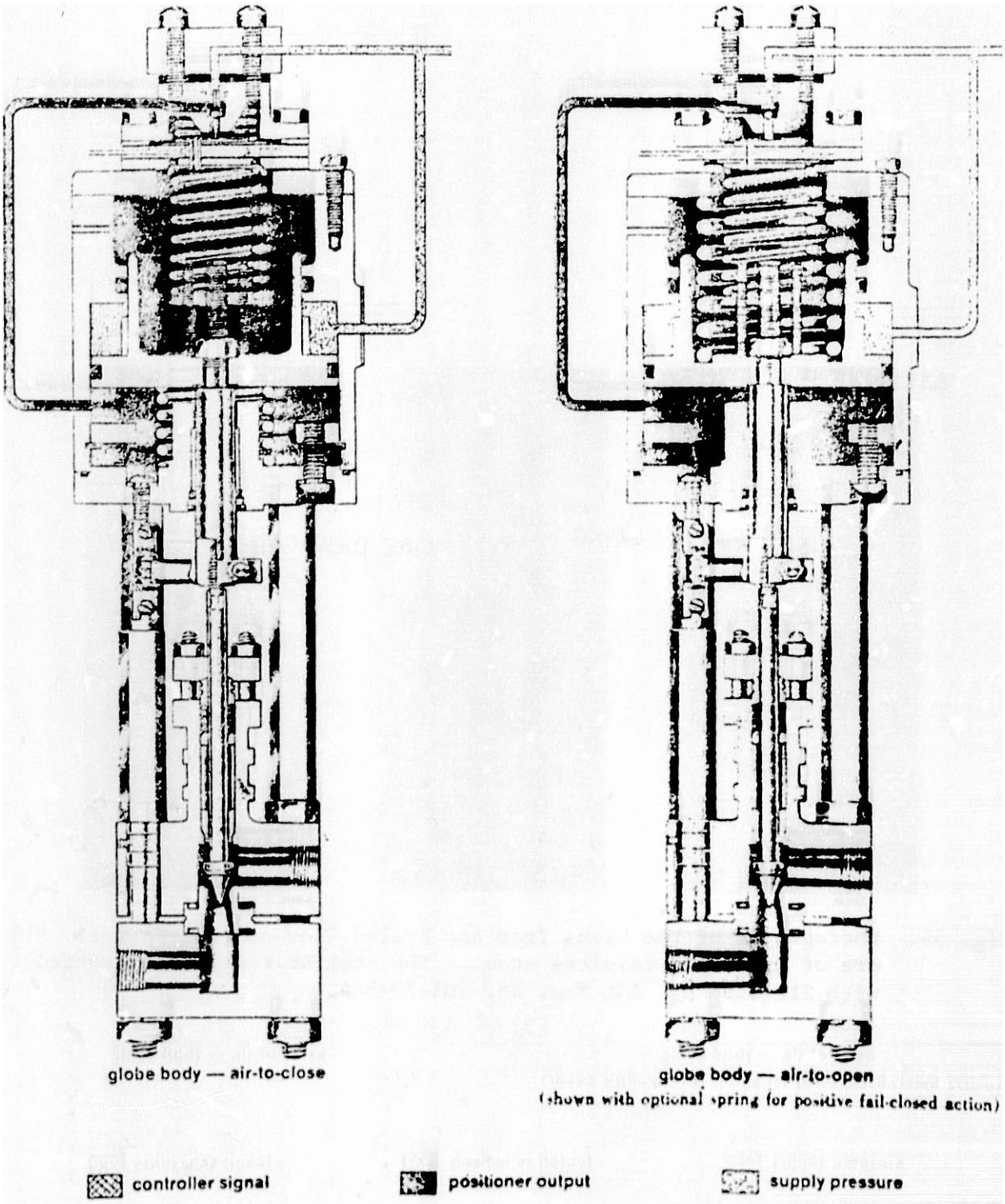


Fig. 53. A Schematic of the Flow-control Valves that Failed by Wire Drawing. ANL Neg. No. 306-79-540.

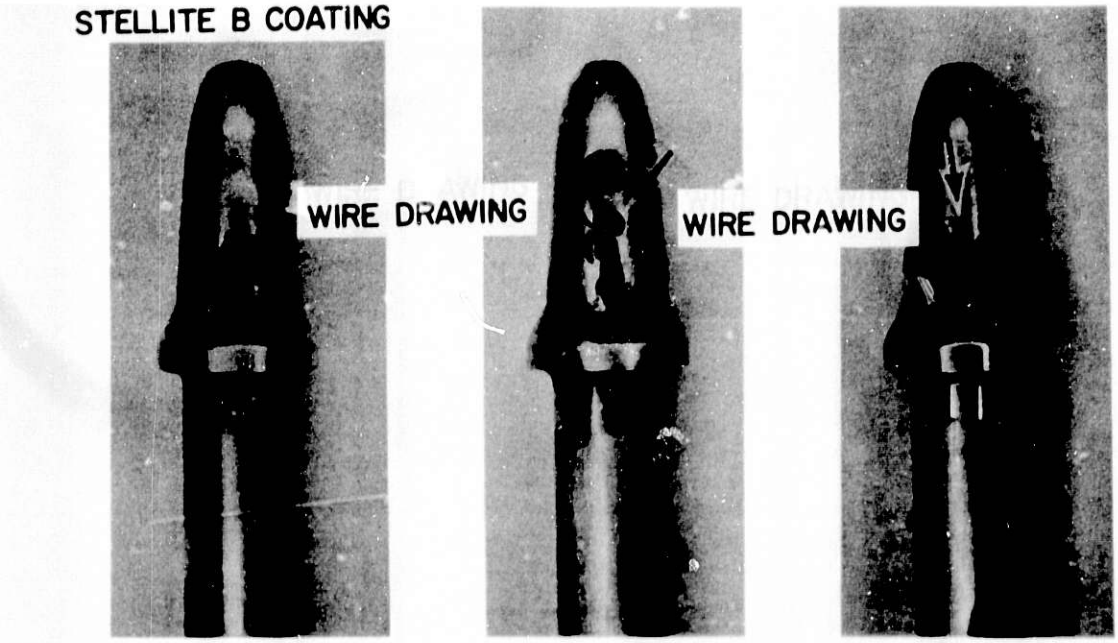


Fig. 54. Photographs of the Stems from the Failed Flow-control Valves. All are of Type 316 stainless steel. The stem at the left is coated with Stellite B. ANL Neg. No. 306-79-544.

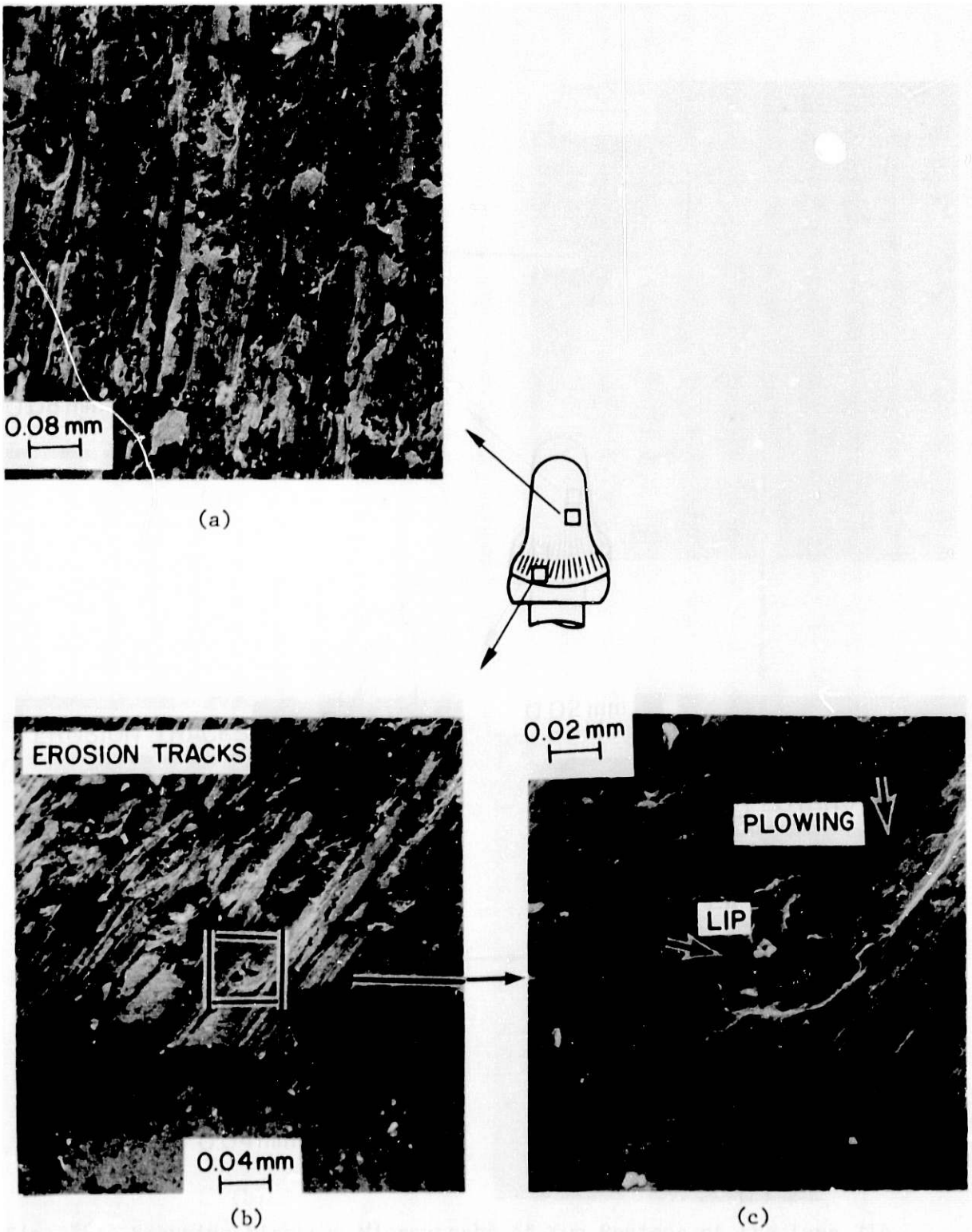


Fig. 55. Scanning Electron Micrographs of Two Regions of the Type 316 Stainless Steel Valve Stem Shown at the Center of Fig. 54. Both regions show metal smearing due to solid-particle impact. Plowing is the dominant erosion mechanism, as evidenced by the material buildup and lip formation visible in (c). ANL Neg. No. 306-79-545.

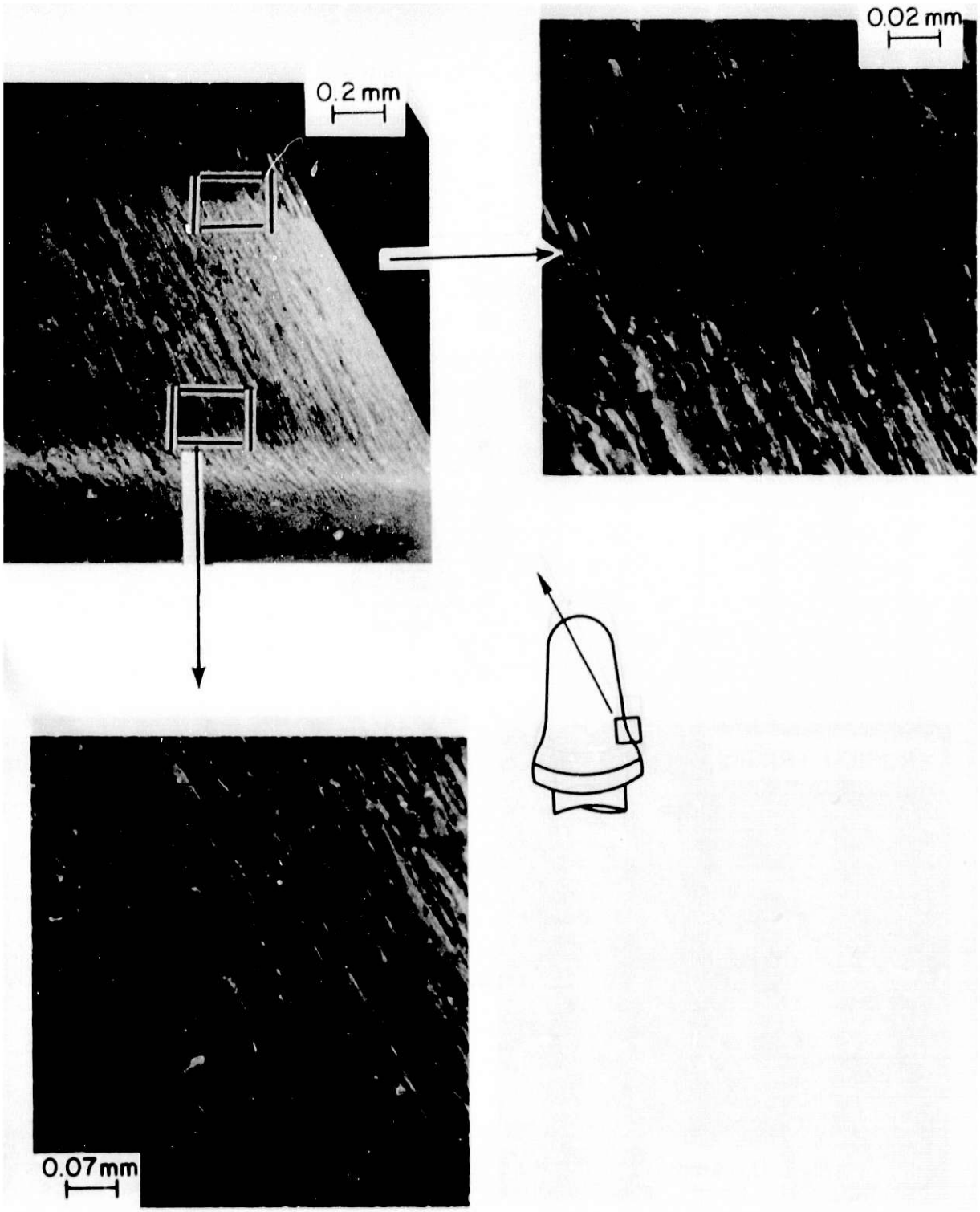


Fig. 56. Scanning Electron Micrographs of Two Regions of the Type 316 Stainless Steel Valve Stem Coated with Stellite B. The micrographs show the solid-particle erosion that occurred in regions subject to low (top) and high impact angles. ANL Neg. No. 306-79-542.

REFERENCES


1. C. R. Kennedy, R. Swaroop, D. J. Jones, R. J. Fousek, R. B. Poeppel, and D. Stahl, "Evaluation of Ceramic Refractories for Slagging Gasifiers: Summary of Progress to Date," Argonne National Laboratory, ANL-78-61 (1978).

2. C. R. Kennedy and R. B. Poeppel, "Corrosion of Refractories Exposed to Molten Acidic Coal-Ash Slags," Interceram 3 (1978).

3. E. A. Snajdr, B. Klaudinyi, J. A. Middleton, and D. S. Yang, "Evaluation of Slag and Refractory Compatibility for Low BTU Gasification of Coal for Electric Power Generation," Combustion Engineering, Inc., FE-1545-48 (December 1977).

4. R. W. Ure, "Refractory Materials for Coal-fired MHD Power Generation," Final Report to the National Science Foundation, University of Utah, UTEC-78-132 (August 1976).

5. "MHD Air Heater Development Technology," Fluidyne Engineering Corporation Report for Period October 1977 to March 1978, FE-3005-1 (April 1978).

6. W. D. Callister, Jr., W. C. Seymour, and V. Griffiths, "Corrosion of Potential MHD Preheater Materials in Liquid Slag and Slag-Seed," Conference on High-Temperature Sciences Related to Open-Cycle, Coal-Fired MHD Systems, April 1977, Argonne National Laboratory, ANL-77-21, pp. 265-269.

7. W. Capps, "Coal Slag Properties Related to MHD," ibid., pp. 190-195.

8. J. J. Rasmussen, The Montana Energy and MHD Research and Development Institute, Inc., private communication (1979).

9. Materials Technology for Coal-conversion Processes, Fourteenth Quarterly Report, April-June 1978, Argonne National Laboratory, ANL-78-79.

10. Materials Technology for Coal-conversion Processes, Thirteenth Quarterly Report, January-March 1978, Argonne National Laboratory, ANL-78-54.

11. Personal letter dated April 6, 1979 from Mr. C.H. Criss to Dr. C.R. Kennedy.

12. T.W. Dickey, J.G. Dimmick, and P.M. Moore, "Feasibility of Acoustic Analysis of Submarine Valve Leakage," Propulsion and Auxiliary Systems Dept. Research and Development Report, David W. Taylor Naval Ship Research and Development Center, Report 78/007 (Jan. 1978).

13. Materials Science Division Coal Technology Ninth Quarterly Report, October-December 1976, Argonne National Laboratory, ANL-77-5.

14. Materials Technology for Coal-conversion Processes, Sixteenth Quarterly Report, October-December 1978, Argonne National Laboratory, ANL-79-23.

15. Metals Handbook, Ninth Edition, Vol. 1: Properties and Selection: Irons and Steels. American Society for Metals, Metals Park, OH (1978), p. 686.

16. R.J. Gray, R.S. Crouse, V.K. Sikker and R.T. King, "A Metallographic Study of Ferrite-Sigma Transformation Using Ferromagnetic Colloid, Microprobe Analysis and Color Etching" in Microstructural Science, Vol. 5, 1977, p. 65.

17. R.T. King, R.J. Gray, J.M. Leitnaker, L.T. Ratcliff and C.W. Houck, "Analysis of Air Distributor Plates from Atmospheric Fluidized Combustors: Rivesville and Alexandria," Oak Ridge National Laboratory, ORNL/TM-6444 (Feb. 1979).